Enabling Photonic Technologies for Dynamic and Adaptive RF Signal Processing

by

Qidi Liu

(Under the Direction of Mable P. Fok)

Abstract

The ultimate objective of this dissertation is to enable photonic technologies for dynamic and adaptive RF signal processing. One of the main driving forces for such an initiative in the near and middle term future come from broadband wireless access networks as well as the growth of fiber links installed in shopping malls, airports, hospitals, stadiums, power plants and other large buildings. However, it is challenging to process different services dynamically and adaptively as emerging RF systems requiring ultra-wide frequency operation range, low communication latency, large data capacity and high information security. In light of increasing functionalities for dynamic and adaptive RF systems, various microwave photonic subsystems are explored to dynamically process from single frequency component to wideband spectrum with enhanced performance in this dissertation. Moreover, recent studies shows that there is intriguing interplay between photonics and microwave signals. The major barrier deterring the exploitation of dynamic and adaptive microwave photonic signal processing is the degree of freedom to manipulate RF-modulated

optical signals (e.g. state-of-polarization, wavelengths, etc). Therefore, there is great potential to apply advanced photonic technologies to dynamic and adaptive RF signal processing.

In this dissertation, real-time RF signal measurement and routing is studied to capture the instantaneous frequency information and rapidly switch among multidimensional RF signal properties, including frequency, amplitude and phase to facilitate the development of high-speed, wideband and secure RF signal processing techniques, which will guarantee emerging/future wireless communication technologies, such as Internet of Things and 5G/6G configuration. Next, dynamic RF spectral processing ability is investigated, which incorporates flexible optical spectrum manipulation and photonic finite impulse response in RF heterogeneous multiband filtering, as well as adaptive point-by-point spectral shaping. Furthermore, in security, dynamic is the key to significantly increase the difficulty for the attacker to decipher the security measure. The introduction of optically-enabled dynamic physical RF steganography in signal transmission could open up a new and effective way to protect sensitive information. This dissertation focus on the design of these system architectures and devise novel signal processing algorithms, which are evaluated through both computational simulation and experimental demonstration to achieve dynamic and adaptive RF signal processing.

Index words: [Microwave photonics, Dynamic radio frequency signal processing, Radio frequency switching, Radio frequency measurement, Optical signal processing, Finite impulse response, Microwave photonic multiband filter, Radio frequency spectral tailoring, Adaptive radio frequency spectral shaper, Radio over fiber transmission and security, Radio frequency steganography]

Enabling Photonic Technologies for Dynamic and Adaptive RF Signal Processing

by

Qidi Liu

B.Eng., Beijing University of Posts and Telecommunications, China, 2014

M.Phil., Beihang University, China, 2016

M.S., University of Georgia, USA, 2020

A Dissertation Submitted to the Graduate Faculty of the

University of Georgia in Partial Fulfillment of the Requirements for the Degree.

Doctor of Philosophy

Athens, Georgia

2021

Enabling Photonic Technologies for Dynamic and Adaptive RF Signal Processing

by

Qidi Liu

Major Professor: Mable P. Fok

Committee: Lawrence A. Hornak

Peter Kner

Luke J. Mortensen

Electronic Version Approved:

Ron Walcott

Dean of the Graduate School

The University of Georgia

December 2021

Dedication

I dedicate this work to my parents, Hongling Jiang and Yong Li, who offered unconditional love and support and have always been there for me. Thank you so much.

To Jiawei Xiong, thanks for encouraging me throughout my education. And thanks for making me see the adventure throughout to the end.

Acknowledgments

I would like to express my deepest gratitude to my research advisor, Dr. Mable P. Fok, not only for her mentoring of my research, but also for her guidance as an amazing teacher, a great leader and a kind friend. The mentoring and guidance from Dr. Mable Fok will be a treasure for a lifetime. My UGA experience with Dr. Mable Fok will not only become a memory that is full of enthusiasm to conduct research and satisfaction on working, but also become a template that will shape my career in the future. To maintain the enthusiasm for research is not easy after years of working on the experiments and especially when the experiments have problems; however, Dr. Mable Fok has a magic way to inspire my enthusiasm.

Next, I would like to extend my sincere thanks to my committee members – Dr. Peter Kner, Dr. Lawrence A. Hornak and Dr. Luke J. Mortensen for their time and effort in improving this work. I am really impressed by their knowledge and experience in optics and photonics from another perspective, which inspires me a lot in my research and thinking.

I also would like to acknowledge my team members, Dr. Frederic Anderson, Dr. Abdelsalam Aboketaf, Dr. Aboozar Mosleh and Dr. Yusheng Bian from my co-op intern at GlobalFoundries for their wonderful collaboration and discussions. I would particularly like to single out my supervisor at GlobalFoundries, Dr. Federick Anderson. I want to thank you for your patient support and for all of the opportunities I was given to further my career.

Furthermore, I would like to recognize the assistance that I received from my lab members. Graduate students: Jia Ge, Li Xu, Mei Yang, Allen Spain, Md Asaduzzaman Jabin. And undergraduate students: Ben Gily, Steven Binder, Victor Qiu, Davis Minor, Daniel Garon, Gabriela C. del Valle Pérez, Hamza Naqawe, Liam Cooper, Mario Garcia, Steven Salazar. Their valuable advice, invaluable contribution and suggestions speed up my research outcome as well as make me feel at home here.

Moreover, I gratefully acknowledge the assistance and effort from all the staff in the College of Engineering, in particular Ms. Margaret J. Sapp and Ms. Victoria E. Martinez, for their constructive advice and guidance along my study.

Finally, I would like to dedicate my thesis to my parents Hongling Jiang and Yong Li. Coming to UGA is the first time I study aboard. And it has been a great challenge for me and an even tougher journey for my mother. I cannot imagine how she is missing me, but to me, she never express any negative emotion. I cannot remember how much support and courage she gave me from the countless international phone calls during my toughest times.

Contents

List of Figures

List of Tables

Chapter 1

Introduction

1.1 Motivation

As commercial and military RF systems continue migrating to higher operating frequencies, the potential for increased bandwidth signal transmission and processing with high dynamic range using RF photonic technology continues to be an attractive option. On the other hand, the scarce spectrum resources cannot keep up with the speed of the exploding spectrum consumption [1], [2] due to the increasing penetration of smart devices (smart phones and tablets), high-performance hardware (e.g., high resolution monitor), high quality user interface design, compelling stream services, as well as the desire for anytime, anywhere high-speed connectivity. It is estimated that the average smartphone user will consume 8.9 GB of data per month in 2021, compared with the number at just 1.4 GB in 2016, according to the latest Ericsson Mobility Report. To utilize the communication resources

Figure 1.1: Dissertation overview.

efficiently and effectively, the combination of two types of communication media become dominant to fit the emerging complex communication environments – fiber-wireless access network [3]. Usually, the main data traffic is fully connected by optical fiber over several hundreds of kilometers, from country to country and city to city as the core network. The use of optical fibers rather than copper cables is considered as ideal front/backhaul media to provide sufficient bandwidth as well as future-proof capacity upgrade. For the "last mile" of the fiber link (i.e., fiber to the home), it is cost-effective and high-performance to connect the center office to the remote wireless base station or dense cells via optical fiber as the access network. On the other hand, at the edge of access network, the wireless communication technologies are dominant in indoor communication, sensor network, and smart cell network. Based on the urgent requirement to massively implement such fiber-wireless access network, our objective here is to investigate dynamic, wideband and adaptive RF signal processing techniques for solving existing RF engineering bottleneck under different application scenarios (i.e. subsystems), such as RF signal identification and routing, dynamic RF spectral management, as well as secure and reliable RF-over-fiber transmission for dynamic access network, as shown in Fig. 1.1, of which specific motivation will be introduced.

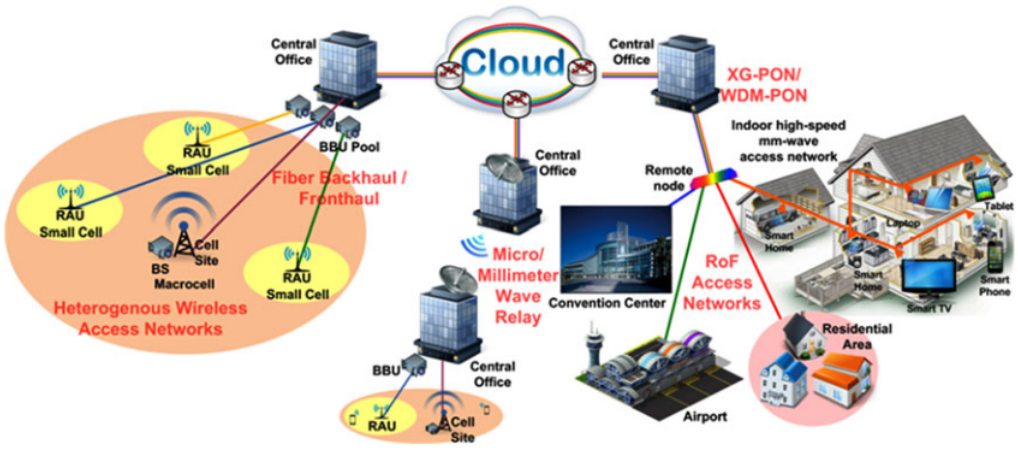

Figure 1.2: Converged fiber-wireless access networks [4]. RAU: Remote antenna unit; BS: Base station; BBU: baseband processing units.

1.1.1 RF Signal Identification and Routing

Microwave frequency measurement is an essential tool in battlefield for identifying threats, providing electronic intelligence, and implementing deceptive countermeasures. In civil applications, RF real-time measurement can be applied to monitor and analyze the perturbation of the sensing network, traffic and automotive control, medicine and health care, and appliances (e.g., microwave oven) [5]. Therefore, the RF signal identification is an indispensable functionality for commercial, defense, and everyday consumer uses. Specifically, dynamic, ultrafast and wideband RF signal measurement with high precision is extremely desired such that spectral information can be extracted in real-time, enabling reliability for the Internet of Things and the target detection.

Moreover, the utilization of the antenna as the wireless transceiver requires the RF operation frequency ranges from a few GHz to tens of GHz, and even hundreds of GHz for THz communication. Thus, to route heterogeneous RF signals over wide and various frequency bands as well as support high-speed data transmission with minimal distortion, ultrafast RF signal switching technology is a critical need [6]. Meanwhile, ultrafast RF switching inherently improves the security of data transmission over the air due to the difficulty to capture the agile frequency carriers (e.g. frequency hopping signals) at the unintended receiver side without any knowledge of the frequency transmitting pattern.

1.1.2 Dynamic RF Spectrum Management

Radio spectrum resources become increasingly crowded and insecure as the number of clients and data capacity exponentially increases these years. To keep a healthy communication environment, improve the quality of service (QoS) as well as provide reliable spectrum usage, dynamic RF spectrum access becomes an

essential part of cognitive wireless communication [7]. For emerging cloud-RAN architecture and future 5G/6G system configuration, as depicted in Fig. 1.2, to simplify the functionality for remote antenna unit (RAU), digital-to-analog conversion (DAC)/ analog-to-digital (ADC) and most RF functions at frontend will shift to the central office (CO). This way, only O/E and E/O conversion, and RF antennas are needed in the modified RAUs [4]. To boost such cloud-RoF deployment, it is beneficial to dynamically manage the spectral resources at CO to support multiple wideband signals as well as enable more advanced and efficient coordination among various services by sharing overall costs (i.e., hardware equipment).

Meanwhile, the dynamic RF spectrum management has potential to support new applications, due to heterogeneous operation on multiple RF spectral bands. For example, the new added services, such as augmented reality (AR), virtual reality (VR), wearable devices, fully immersive experience (3D), possibly occupy new frequency bands, which is not compatible with static RF spectral processing system; however, with dynamic RF spectrum manipulation, the new applications can be directly placed on the device without any hardware upgrading. Therefore, dynamically processing and manipulating a wide RF spectrum that spans across tens of GHz bandwidth provide more versatility and flexibility to maintain the dynamic multi-function RF applications.

1.1.3 Radio-over-Fiber Security

In modern society, optical fiber is the dominant transmission medium of the physical communication network, forming the backbone of the Internet that connects cities and nations across oceans and continents with long haul transmission systems. For fiber-wireless access network, security measures are inevitable to support radio-over-fiber transmission of mobile radio frequency signal (e.g., cellular frequencies, WiFi and WiMax) [8], [9]. Conventionally, to secure the information during transmission, data are encrypted

using software through an encryption key, such that the attackers are not able to interpret the information without the knowledge of the encryption key [10]. Security resulted from encryption is based on the assumption that the attacker is not able to figure out the encryption key; however, it is just a matter of time for the attacker to encrypt the data once he/she get a hold of the data.

For example, the eavesdroppers can still detect the existence of the transmitted data because the data is already exposed in the public traffic and can be attacked easily. Therefore, there is a critical need to provide another layer of security – steganography [11] to secure the data – the secret information is concealed such that the attacker will not even know they should be looking for the information or where to look for the information. This way, for fiber-wireless network, the attacker at any fiber node will never recognize the transmitted RF signal at any frequency channel as well as demodulate the carried data information. Furthermore, in security, dynamic is the key to significantly increase the difficulty for the attacker to decipher the security measure. The introduction of dynamic physical steganography information transmission could open up a new and effective way to protect sensitive information.

1.2 Problem Statement

Although the motivation for dynamic, wideband, adaptive and secure RF systems is explicit, numerous problems needs to be addressed when designing subsystems to enable it, such as real-time RF signal identification, fast routing and effectively allocating the RF spectral resources. Consequently, this section targets to dig into the existing problems in many RF systems.

1.2.1 System Dynamics

While new RF resources from MHz to tens of GHz have been made available to emerging wireless technologies such as the 5G system, the inability to dynamically and precisely manipulate the whole available RF spectrum hinders the performance of the associated multi-/wideband systems. Although it provides compact circuit design, current electronic-based RF system suffers from the lack of tunability and limited reconfigurability over narrow bandwidth. For example, to fulfill various RF system functions, different RLC circuits are required, resulting in electronic restriction in the order of microsecond response speed and MHz tuning range. Taking advantage of photonic techniques, the RF signal is first converted to an optical signal, which can then be processed almost instantaneously over broad frequency bands [12]. However, it is still challenging to achieve dynamic RF signal processing due to the inflexible optical spectrum manipulation through most existing techniques [13], [14]. The lack of system dynamics causes the increase in noise figure, low data transmission rate, unavoidable information interception as well as complex system to support new applications.

Moreover, frequency-dependent non-uniform RF responses occur in individually manufactured RF devices and comprehensive multiband RF communication network is a critical issue that conventional electronics cannot handle easily. Dynamic RF systems offers not only precise processing and handling of broadband microwave signals, but also provide higher system security by flexibly adjusting the physical layer parameters. This dissertation focus on exploring the full potential of manipulating optical spectrum such that the carried RF signals can be dynamically processed according to the complex user-defined functions and the dynamic transmission scenarios.

1.2.2 Security Measures

To ensure the information security of the fiber-wireless network as well as enable high-capacity data being transmitted at a high speed, appropriate security measures which would not deteriorate the system performance have to be investigated. According to the open system interconnection (OSI) model [15], security measures can be taken ranging from the most bottom of the network layer (i.e. physical layer) to the highest layer (i.e. application layer). However, electronic security measures, such as electronic encryption, electronic RF fast switching, gradually meet its bottleneck due to the limited data transmission speed and wiretapping simplicity resulting from the monotonous encryption techniques with limited current and voltage range. Turning to the photon wave function, which enables more degree of freedom manipulation (i.e. frequency, phase, amplitude, polarization, orbital angle momentum, the order of mode, etc), and the use of light to increase the RF signal transmission security is quite promising to solve many security challenges in its electronic counterpart.

Besides the software-based data encryption, two hardware-based approaches are deemed to be effective for preventing the information from attacking: 1) fast-changing information carriers such that the attacker cannot easily jam the channel, catch and analyze the signal of interest promptly; 2) hiding RF signal of interest under the public network such that the untrusted users are never conscious of the existence of the secret signals. Currently, the electromechanical switches and microelectromechanical systems (MEMS) switches have switching time in the range of microsecond; while solid-state switch has a switching time of nanosecond due to the intrinsic physical properties and switching mechanism of electronic devices, which has great potential to be improved with the help of photonics. For physical layer security over fiber,

conventional optical encryption mainly protects pure data-driven optical transmission within main road. However, there is no scheme to dynamically protect the access network in physical layer.

1.3 Overview of Microwave Photonic Signal Processing

This section describes some background knowledge about microwave photonics and how it inspires the design of dynamic and adaptive RF signal processing techniques developed in this dissertation.

1.3.1 Microwave Photonic System

Conventional RF signal processing approaches are usually implemented by electronic RLC circuit – resister, inductor and capacitor – to fulfill the designed RF transfer function. However, the inherent electronic bottleneck is limited by the rate at which the electrons can move (2200 km/s), inductive and capacitive effects as well as resistive losses associated with electron propagation in materials. In this way, the electronic-based system performance significantly degrades as the demand of operation frequency, reconfigurability, tunability and response time increases. To meet the urgent requirement in these aspects, microwave photonics is an emerging hot interdisciplinary area which investigates the interaction between light wave and microwave signals, and becomes a good candidate to tackle the challenges in its electronic counterpart [16], [17]. For decades, the field of microwave photonics involves the photonic microwave generation, transmission, distribution, receiving as well as analyzing, which greatly improves the conventional RF engineering and electronics as photonics offers unprecedented opportunities to the systems that are either too complex or not possible to be achieved directly in the RF domain [18]. Initially, the applications of microwave photonics focus on national defense such as electronic warfare, (anti-)detecting enemies,

unmanned aerial vehicles (UAV) manipulation, radar jamming and deception, to name a few. In recent years, consumer applications pushes the need of MWP as the demands of high-speed, high-capacity and wideband RF systems increase, such as cellular, cable television, wireless and satellite communications, distributed antenna systems, sensing, optical coherence tomography techniques and medical imaging.

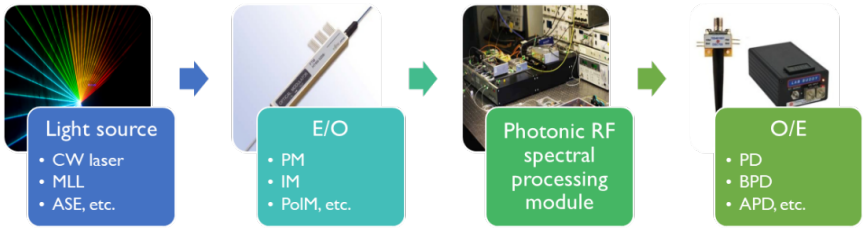

Figure 1.3: Microwave photonic system configuration.

As shown in Fig. 1.3, to achieve user-defined RF functionality, the RF signals being processed are modulated onto the light source through the E/O converter at the beginning of the system. The light source can be chosen among continuous wave (CW) laser, mode-locked laser (MLL), as well as amplified spontaneous emission (ASE) noise thanks to the mature laser technology developed since 1960. Depending on the target tasks, the E/O converter is capable of diverse signal modulation formats, such as phase modulation (PM), intensity modulation (IM), and polarization modulation (PolM). Afterwards, the modulated light, which carries the information of RF signals, is sent to the particularly designed photonic RF signal processing module to realize the complex and wideband RF signals functionality. At this stage, various optical devices, such as optical delay lines, optical attenuators, optical fibers, as well as optical amplifiers, are utilized to construct optically enabled RF signal processing sub-systems. Then, an O/E converter is needed to convert the processed optical signal back to electrical domain. Comparing with its electronic counterpart, microwave photonic signal processing system enables ultra-wideband RF signal

manipulation, resisting electromagnetic interference as well as ultrafast response speed by using the high-frequency light wave (in the order of THz) as signal carrier. For example, a hundred GHz RF signal only occupied 2.2% frequency resource of the C band (1530 - 1565 nm) in optical domain, which is a big consumption in RF domain. Furthermore, transmitting RF modulated (digital or analog) light signal over fiber enables ultra-low loss, which is 0.2 dB/km for standard single mode fiber, while the signal arriving at the receiver over just 100 m of an electrical cable (30 dB/100 m) without amplification are only a dim possibility.

1.3.2 Finite Impulse Response

Finite impulse response (FIR) is characterized by the fact that the delayed and weighted versions of the input signal will lead to either destructive or constructive interference in time domain at output [19]. However, only the constructive interference will have relatively large amplitude response in frequency domain, as illustrated in Fig. 1.4.

By setting pre-designed time delay and weight of each tap, desired finite impulse response at particular frequency location (i.e. constructive interference) can be resulted. The mathematical relationship between the response and design parameters is expressed as,

$$H(\omega_{RF}) = \sum_{i=0}^{N-1} a_i exp(-j\omega_{RF} iT) \tag{1.1}$$

Where ω_{RF} is the microwave frequency, a_i is the amplitude of the i-th tap, N is the tap number and T is the time delay between adjacent tap. It is important to note that the tap number N governs the characteristics of the designed filter in both Q-factor as well as main-side lobe suppression ratio (MSSR)

in frequency response. Compared with electronic-based FIR filter, which utilizes multi-tap electrical delay line combined with electrical amplifier at each tap, the weighted and delayed copy of the input RF signal is scaled onto optical domain when applying microwave photonic filter. To achieve such a MWP filter, chromatic dispersion in optical fiber plays an important role, as shown in Fig. 3, which makes different colors in an optical pulse propagate at different speed. Hence, the RF signals carried by different color (tap) will naturally experience different time delay between adjacent copy. On the other hand, the weight difference can be adjusted by controlling the intensity of each color (tap). In this way, the required time delay and proper weights designed for specific microwave photonic FIR filter can be successfully achieved.

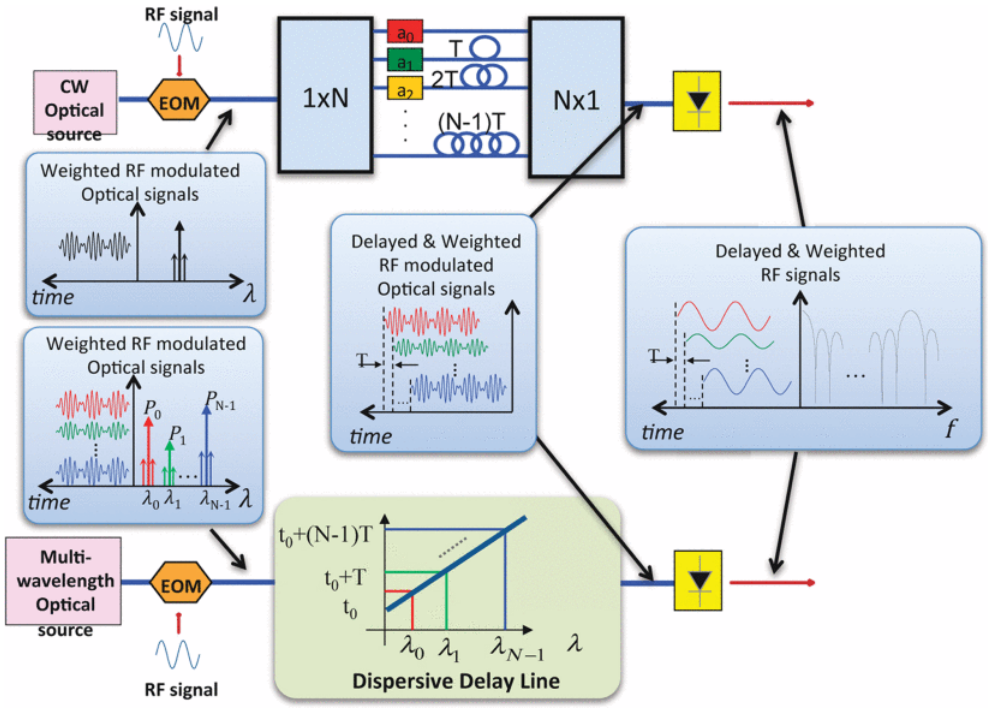

Figure 1.4: Microwave Photonic discrete-time finite impulse response [20]: (a) CW optical source connected with an array of multiple optical delay paths and attenuators; (b) multi-wavelength optical source combined with a linear dispersive delay line.

Currently, two common approaches for implementing microwave photonics filters are depicted in Fig. 1.4. In the upper illustration, one CW optical source is used to modulate the input RF signal. Then,

the modulated light is split by a 1-N demultiplexer. For each path, an optical attenuator associated with an optical delay line of particular relationship is deployed. According to Eq. 1.1, the weight of each copy is controlled by each attenuator and the fixed delay T between each copy is governed by the length difference of adjacent path. However, it is inconvenient and impractical to adjust every attenuator and delay line each time for turning to another filter setup. Besides, when large numbers of taps are needed, the massive branches would greatly increase the cost and system complexity. it takes advantages of multi-wavelength optical source and dispersive delay line in the lower illustration, and has shown great improvement over the previous scenario, the time delay between each copy can be easily tuned by the separation of each optical carrier, $T = \Delta\omega\beta_2 L$, where $\Delta\omega$,β_2,L are comb spacing, group velocity dispersion and length of dispersive medium, respectively. So far, two popular techniques are being used to achieve such a functionality. First, coherent spacing-adjustable optical frequency combs with large comb lines can be realized by either cascaded IM/PMs or pumping an ultra-high-Q optical resonator with Kerr nonlinearity using a continuous-wave laser. Alternatively, in incoherent regime, a comb-like spectral slicing method can be used to trim the input incoherent broadband light source (e.g. ASE noise) into multi-wavelength light source. In either way, the obtained multiple optical carriers with different amplitudes and certain spacing, which is then modulated by RF signals and sent to a dispersive medium to introduce chromatic dispersion induced time delay. Then, by detecting all the taps at a high-speed photo-detector, the designed RF FIR filter can be achieved.

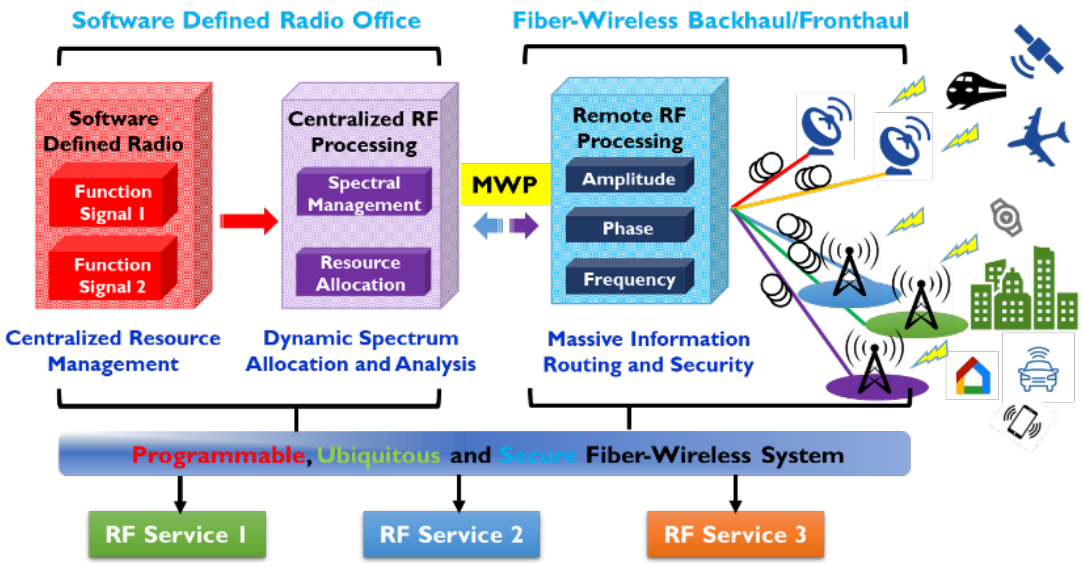

Figure 1.5: Dynamic and wideband microwave photonic fiber-wireless system.

1.4 Overview of Dissertation Chapters

Due to the conflict between the growth of mobile data traffic and limited spectrum resources at conventional RF bands, more efficient spectral usage and dynamic spectral management techniques are the two main directions for the next-generation and high-speed wireless access networks. As shown in Fig. 1.5, dynamic and wideband microwave photonic signal processing system includes software defined radio, centralized RF processing as well as remote RF signal processing unit. In this dissertation, various subsystems to support programmable, ubiquitous and secure fiber-wireless RF system is proposed, including two interconnected research themes: **Theme I: Dynamic RF Signal Measurement and Switching** and **Theme II: Adaptive RF Spectral Processing and Physical Security over Optical Fiber**. Briefly, the challenges and corresponding solutions for each subsystem are summarized in Table 1.1.

This dissertation mainly contains of 6 chapters, as described in Table 1.1. The objective for each microwave photonic subsystems are evaluated through both computational simulation and experimental demonstration.

Chapter 1 introduces the motivation, problem statement and the overview of microwave photonic systems. Besides, this chapter reviews the current status of high-speed, dynamic microwave photonic signal processing, and defines the objectives of this dissertation.

Chapter 2 discusses the dynamic instantaneous radio frequency measurement enabled by photonics. This chapter first investigates the dual-function frequency estimation system including instantaneous RF frequency as well as Doppler shift measurement. Next, data-driven approach assisted by machine learning is explored such that the frequency estimation error is reduced to 50 MHz in tens of GHz frequency measurement range.

Chapter 3 provides a comprehensive review on fast frequency hopping signals and expand the research to the design of multidimentional RF switch with picosecond on/off speed for dynamic and high-speed RF applications enabled by photonic four wave mixing nonlinear effect. The developed real-time multidimensional radio frequency signal switching is able to switch various RF properties including amplitude, phase and frequency with less than 50 ps to ensure transmission security.

Chapter 4 comprehensively studies dynamic and heterogeneous radio frequency spectral properties tuning, including independently amplitude, frequency, bandwidth, and group delay slope tuning. In addition, independent spectral shape reconfiguring between Gaussian, flat-top, and triangular shapes has also been achieved. By embedding adaptive decomposition and reconstruction algorithms, point-by-point spectral shaper for arbitrary wideband frequency response is also achieved.

Chapter 5 explores the dynamic RF secure signal transmission for emerging communication networks. The idea is inspired by Marine Hatchetfish, which uses silvering and counter-illumination strategies to hide from predators and preys in the ocean.

Chapter 6 concludes the dissertation by discussing the limitations of this dissertation objective. The potential miniature and integration of the demonstrated systems in the future is also explored.

Table 1.1: Brief Summary of Each Chapter Work

	Functionalities	**Applications**	**Challenges**	**Solutions**
Theme I	Instantaneous frequency measurement & Doppler shift detection (**Ch.2**)	Radar, satellite, smart vehicles monitoring	Low measurement resolution, frequency range, separate function setup.	Dynamic PM-Lyot filter adjustment & machine learning
	Real-time RF signal switching (**Ch.3**)	Signal routing, multidimensional RF modulation	Low switching speed, non-transparent modulation formats	Polarization-dependent FWM
Theme II	RF multiband filtering (**Ch.4**)	Multiband radar communication, out-of-band noise rejection	Limited passband tunability and reconfigurability	Independent optical spectral shaping & FIR
	RF spectrum tailoring (**Ch.4**)	multi-function mobile service; equalizing spectral unevenness	Simple spectral processing functions	Adaptive Two-section algorithm: Decomposition & reconstruction
	RoF physical security (**Ch.5**)	Secure data transmission in physical layer	Software based encryption	Dynamic RF signal steganography

Chapter 2

Dynamic Instantaneous Radio Frequency Measurement Based on Photonics

2.1 Instantaneous Microwave Photonic Frequency Measurement

Instantaneous frequency measurement (IFM) and Doppler frequency shift (DFS) measurement systems are two essential tools in battlefield for identifying threats, providing electronic intelligence, and implementing deceptive countermeasures. Due to the advancement of emerging RF wireless systems, the frequencies that are encountered by IFM and DFS systems could range from MHz to tens of GHz, proposing a challenge to the electronic based measurement system. Photonics has been a promising solution to tackle challenges in modern RF electronic systems. Various microwave photonic based IFM systems and DFS measurement systems have been individually demonstrated. For example, IFM can be achieved using

frequency-to-time mapping [21], power fading comparison [22], [23], SBS-assisted phase-to-intensity modulation [24], and frequency-to-intensity mapping [25]. While DFS measurement systems can be achieved based on signal beating of sidebands generated from either cascaded intensity modulators [26] or the dual parallel MZMs [27]. Although existing photonic-based IFM and DFS systems solved some of the challenges in their electronic counterparts, they could easily suffer from limitation including low resolution, narrow operation frequency range, as well as Doppler frequency shift measurement errors and significant resolution degradation in frequency measurement due to dynamic spectral misalignment.

2.2 Dual-Function Instantaneous RF Measurement and Doppler Shift Measurement

[1] In this section, we propose and demonstrate a dual-function microwave photonic system that can perform both IFM and DFS measurements with adaptive and enhanced resolution as well as dynamic frequency measurement range. The proposed system can perform both IFM and DFS measurement without the need to replace any hardware, which provides operation flexibility when implementing it in a battlefield. The key component in our system is a phase modulator incorporated Lyot loop filter (PM-Lyot filter) [28] which is capable of fast adaptation to any spectral drifting as well as providing dynamic resolution setting based on the signal frequency. The PM-Lyot filter can be adjusted to achieve a sharp spectral profile with high peak-to-notch extinction ratio for the enhancement of frequency resolution and for a complete carrier suppression to ensure accurate DFS measurement. Based on the principle, a microwave photonic dual-function system capable of measuring both instantaneous frequency and Doppler frequency shift

[1] **Q. Liu** and M. P. Fok. "Dual-function Frequency and Doppler Shift Measurement System Using a Phase Modulator Incorporated Lyot Filter." Optical Fiber Communication Conference (OFC), Th2A. 36, 2019.

is experimentally demonstrated. The system consists of a tunable Lyot loop filter that enhances spectral resolution and reduces measurement error.

2.2.1 Experimental details

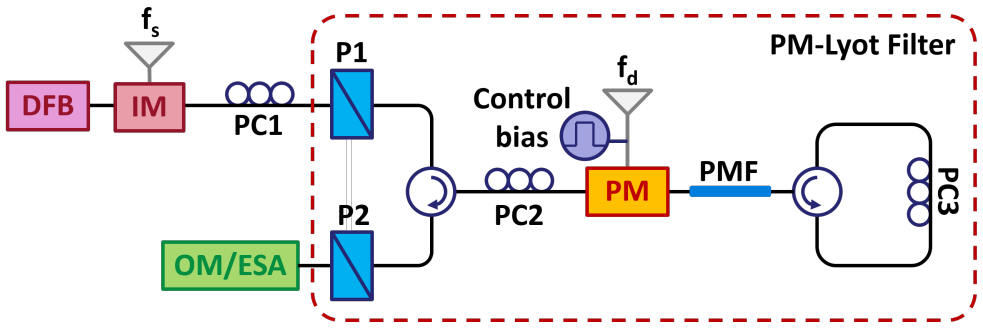

Figure 2.1: Experimental setup of the dual-function IFM and DFS system. DFB: distributed feedback laser; IM: Mach-Zehnder intensity modulator; PM: phase modulator; PMF: polarization maintaining fiber; PC1-3: polarization controller; P1-2: polarizer; PD: photodetector; OM: optical power meter; ESA: electrical spectrum analyzer.

Figure 2.1 shows the experimental setup of the proposed dual-function frequency measurement system. A distributed feedback laser (DFB) centered at 1549.03 nm is used as the optical carrier and the received RF signal at fs is modulated onto the optical carrier through a 10-Gb/s electro-optic intensity modulator (IM). The IM is biased at its minimum transmission point to achieve carrier-suppressed double-sideband modulation (CS-DSB). The CS-DSB signal is then launched into the PM-Lyot filter. The PM-Lyot filter is an interferometric comb filter that consists of a pair of polarizers, a 10-Gb/s phase modulator (PM), a 9-m polarization maintaining fiber (PMF) and three polarization controllers (PC1-3). Free spectral range (FSR) Δf of the PM-LMF is governed by,

$$\Delta f = \frac{c}{B_{PMF} L_{eff} - B_{PM} L_{PM}} \tag{2.1}$$

where B_{PMF}, B_{PM}, L_{eff} and L_{PM} are the birefringence and effective length of the PMF and the waveguide in the phase modulator, respectively. The optical circulator and the polarization controller PC3 construct a loop that allows light to travel back to the PMF to experience additional birefringence. If the polarization rotation of PC3 is set to 0°, the light that is propagating back to the input will experience birefringence from the PM and PMF again, resulting in an effective length of 2L. On the other hand, if PC3 is set to 45°, the light will not experience any birefringence on its way back ($L_{eff} = L$). In our experiment, the phase modulator consists of a 71-mm $LiNbO_3$ crystal with birefringence of 7.4×10^{-3} and a 1-m PMF pigtail at the output with birefringence of 3.0×10^{-4}, while the 9-m PMF has a birefringence of 6.33×10^{-4}. It is worth to notice that birefringence of the phase modulator waveguide can be slightly tuned by applying a DC bias voltage to it. The resultant change in FSR of the PM-Lyot filter is so small that only a spectral shift in the optical comb can be observed if we focus on a small wavelength section.

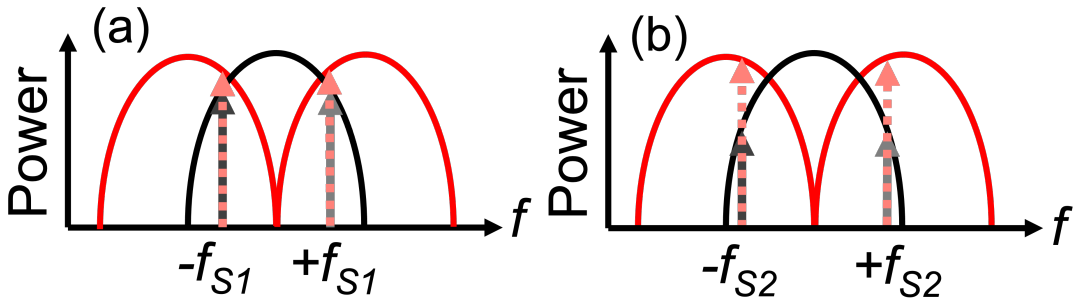

Figure 2.2: Principle of IFM measurement.

To perform IFM, the PM-Lyot filter transmission peak is first aligned with the optical carrier frequency (f_0) of the CS-DSB signal, such that the two sidebands ($f_0 - f_s$ and $f_0 + f_s$) are aligned to the rising and falling slopes of the transmission function, as shown in Figure 2.2(a). Since the sidebands of signal with different frequency will align at a different part of the transmission function, different amount of optical power ($P_{peak} = sin^2(\pi f_s / \Delta f)$) is resulted for different input frequency. However, the resultant

optical power also depends on the input RF signal strength, meaning that any power fluctuation will negatively affect the accuracy of frequency measurement. To solve this problem, we propose to measure the power ratio of the sidebands between (i) P_{peak}: when the transmission peak is aligned with the carrier – dashed black curve and (ii) $P_{notch} = cos^2(\pi f_s/\Delta f)$): when the transmission notch is aligned with the carrier –solid black curve. Tuning between the two cases is achieved by applying a DC voltage to the phase modulator, and fast tuning at tens of GHz speed is supported through electro-optics Pockel effect [29]. Power ratio between P_{peak} and P_{notch} always has a fixed relationship for certain frequency despite the power of the RF signal and the optical carrier. Thus, the frequency-to-power ratio (L_p in dB) can be expressed as,

$$L_p = \gamma log\left[tan(\frac{\pi f_s}{\Delta f})\right] \tag{2.2}$$

where γ is proportional to the extinction ratio of optical comb filter. When a higher frequency resolution is desired, the PM-Lyot filter can be tuned to have its FSR cut by half by setting polarization controller PC3 at $0°$. On the other hand, if a larger frequency range is desired, the polarization controller PC3 is set at $45°$, such that a full FSR is obtained to support doubling the frequency range.

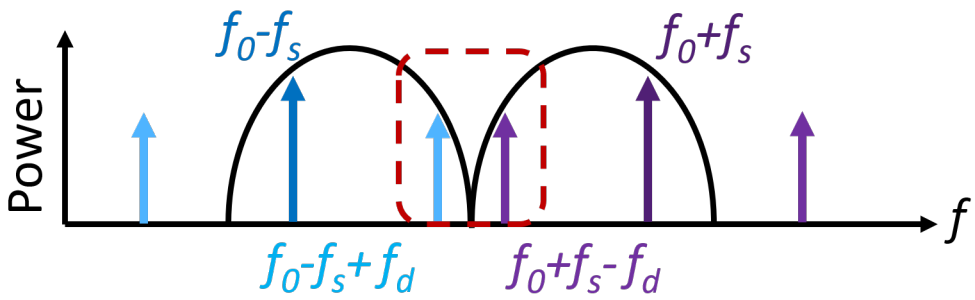

Figure 2.3: Principle of DFS measurement.

Furthermore, the proposed system can be used for DFS measurement for advanced RF systems including satellite communication and missile radar where the carrier frequency is at GHz to tens of GHz. First, the transmitted signal f_s is modulated onto the intensity modulator to achieve CS-DSB modulation, while the received signal f_d (usually is tens of MHz from f_s) is modulated onto the sidebands $f_0 - f_s$ and $f_0 + f_s$ through a phase modulator and two sets of secondary sidebands $f_0 - f_s - f_d$ and $f_0 - f_s + f_d$ as well as $f_0 + f_s - f_d$ and $f_0 + f_s + f_d$ are generated, as illustrated in Figure 2.3. The PM-Lyot filter is having its transmission notch aligned with the optical carrier frequency such that the residue optical carrier of the CS-DSB signal can be completely suppressed to prevent errors in the measured Doppler frequency. Since the Doppler shift is typically below GHz range, a photodetector with bandwidth of 190 MHz is used to generate the beat signal between the two secondary sidebands, resulting in a beat signal frequency $f_b = 2|f_d - f_s|$. The factor 2 in the equation essentially enhanced the spectral resolution by two times.

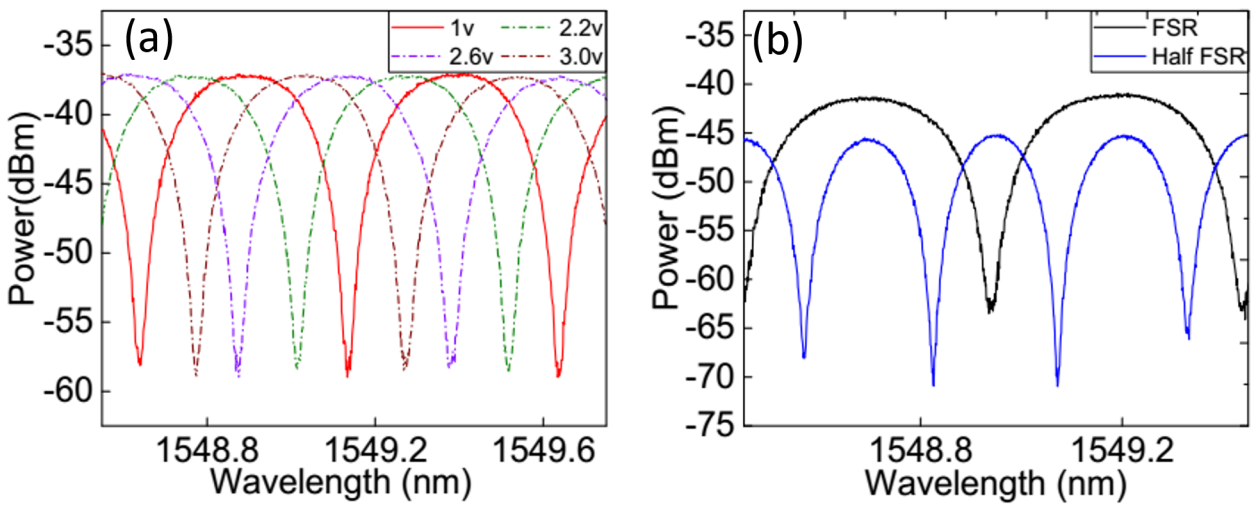

Figure 2.4: (a) Transmission spectrum of PM-Lyot filter with different control bias at the PM; (b) Full FSR (black) and half FSR (blue) transmission spectrum resulted from the control feedback polarization.

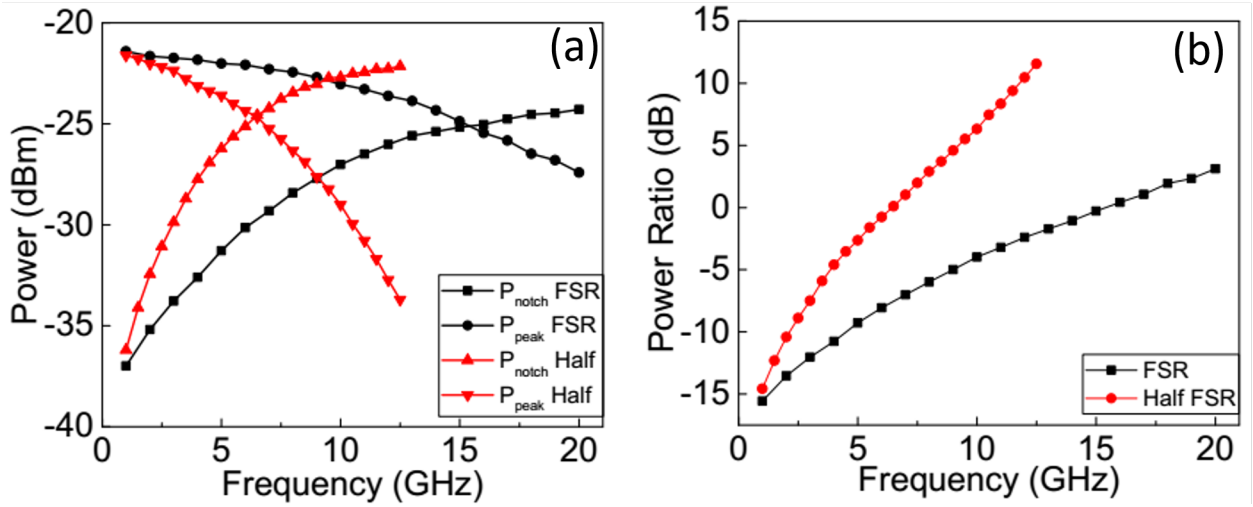

Figure 2.5: (a) P_{peak} and P_{notch} measurement when working at full FSR (black) and half FSR (red) settings; (b) Power ratio measurement when operating at full FSR (black) and half FSR (red) settings.

2.2.2 Results and Discussion

First, we study the relationship between the spectral positions of the PM-Lyot filter with the bias voltage, as shown in Figure 2.4(a). The optical spectrum is measured by an optical spectrum analyzer (OSA) with 0.8-pm resolution. The PM-Lyot filter has a 21-dB extinction ratio and FSR of 0.493 nm, corresponding to 61.6 GHz in frequency. The comb shifts to a shorter wavelength while maintaining its overall profile when a positive DC bias is applied to it. A 1.6 V of voltage change is needed to shift the comb from peak to notch at a particular wavelength. Furthermore, FSR of the PM-Lyot filter can be changed by controlling PC3 in the return loop. Figure 2.4(b) shows a half in FSR when PC3 is set at 0° (blue), and a FSR with PC3 set at 45° (black). The red triangle and the black squares in Figure 2.5(a) show the direct power measurement of P_{peak} and P_{notch} when half and full FSR combs are used, respectively. The resultant

power ratio L_p measurement is shown in Figure 2.5(b) that clearly show a 2.7-dB/GHz enhancement in frequency measurement resolution when half FSR setting is used instead of a full FSR setting.

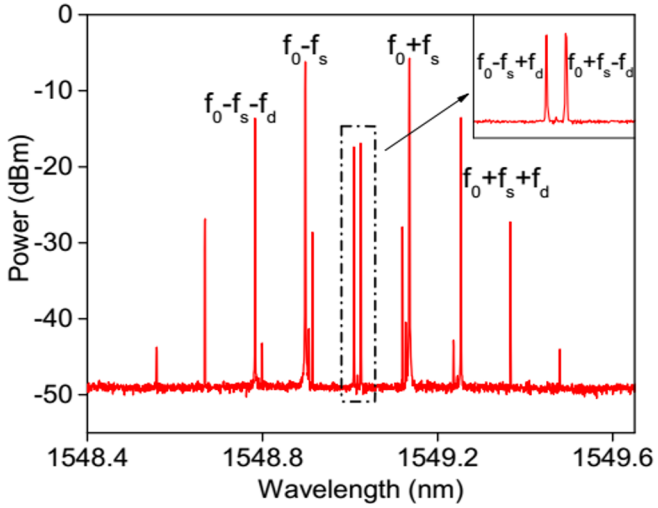

Figure 2.6: Optical spectrum of PM-Lyot filter output during Doppler frequency shift measurment (inset: zoom-in view showing complete carrier suppression)

Next, we use the proposed system for DFS measurement. The transmitted signal at 15 GHz is modulated onto an optical carrier using an intensity modulator to generate a CS-DSB signal, while the received signal is modulated onto the generated sidebands at the phase modulator in the PM-Lyot filter. Figure 2.6 shows the optical spectrum at the output of the PM-Lyot filter. For a clear display in Figure 2.6, a 14 GHz signal is used as the received signal instead to provide a significant spectral separation (2 GHz) between the two generated secondary sidebands. In Doppler frequency shift, the frequency difference should be in the order of kHz to MHz. Complete suppression of the optical carrier is observed as shown in the inset. Figure 2.7(a) show the resultant RF spectrum of Doppler shift measurement when the optical carrier is not completely removed, where incorrect frequency components are observed and causes error in the measurement. With a complete suppression of optical carrier, a pure frequency component is observed in Figure 2.7(b) that corresponds to two times of the Doppler frequency shift at 1 MHz.

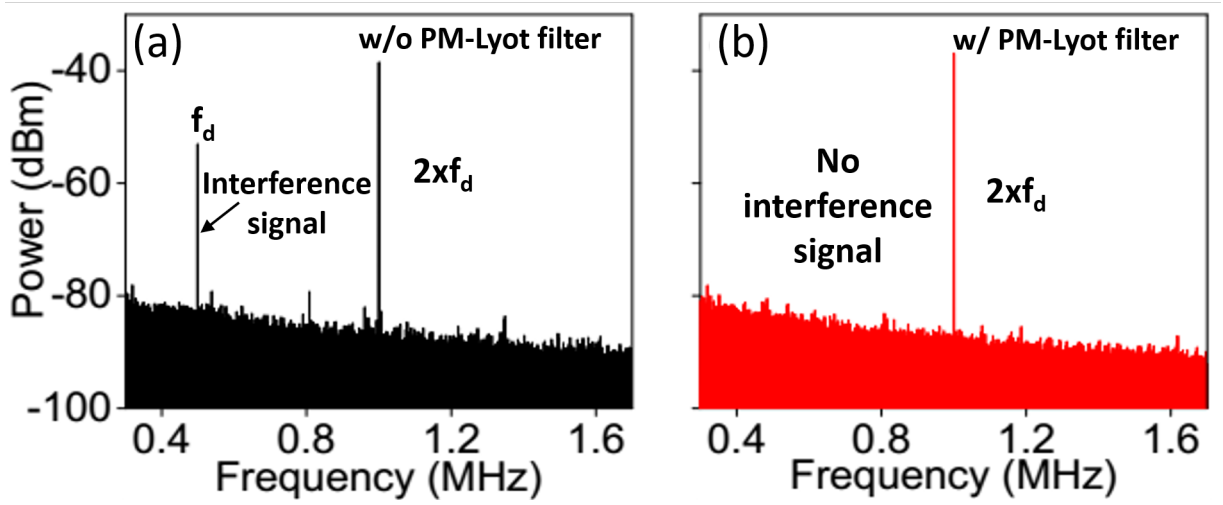

Figure 2.7: Optical spectrum of PM-Lyot filter output during Doppler frequency shift measurment (inset: zoom-in view showing complete carrier suppression)

2.3 Data-Driven Microwave Photonic Frequency Estimation

[2] Instantaneous microwave frequency estimation enables numerous essential applications in the commercial, defense, and civilian marketplace. The advancement of applications is hindered by the bottleneck in electronic-based frequency measurement systems including narrow bandwidth, high errors rate, and low dynamic range. Photonics-based frequency estimation approaches not only increase the operation frequency range and provide rapid measurement response, but also benefit from immunity to electromagnetic interference and enhancement in system adaptability. Despite the unique advantages offered by photonics-based frequency estimation approaches, it is challenging to obtain linear mapping between the unknown frequency and the measured optical characteristics due to the nonlinear response in electro-optical devices, which consequently results in degradation in measurement precision and a

[2] **Q. Liu**, Benjamin Gily, and M. P. Fok. "Adaptive Photonic Microwave Instantaneous Frequency Estimation Using Machine Learning." IEEE Photonics Technology Letters (under revision)

complex calibration relationship. Therefore, it is critical to mitigate the challenge to achieve dynamic, adaptive, and high-precision estimation of microwave frequency. To this end, this section presents the design and demonstration of a high-precision photonic based instantaneous frequency estimation system driven by machine learning. A three-layer deep neural network is used to tackle device nonlinearity and system noise, resulting in absolute error of < 50 MHz and root mean square error of 1.1 MHz.

2.3.1 Introduction

Wideband instantaneous microwave frequency estimation system is an essential tool for radar detection, electronic warfare, military threats identification, decisive intelligence acquisition, and deceptive countermeasures implementation [30]. However, emerging wideband and complex wireless environment brings critical challenges to realize frequency estimation using conventional electronic technologies, resulting in narrow bandwidth, high errors rate, and low dynamic range measurements. The unique characteristic of photonic, including wideband operation, high reconfigurability, and instantaneous response make photonics be a promising candidate to overcome hurdles faced by electronics approaches. Microwave photonic based frequency estimation have been demonstrated using frequency-to-time mapping [21], power fading comparison [31], SBS-assisted phase-to-intensity modulation [24], and frequency-to-intensity mapping [25]. Although existing photonic approaches solved some of the challenges that their electronic counterparts are facing, current photonic schemes suffer from relatively limited reconfigurability for optimizing measurement performance, large frequency estimation error in the order of hundreds of MHz, and inability to adapt to dynamic RF scenario.

At the same time, machine learning (ML) has been used to enhance a wide range of photonic signal processing tasks, including optical performance monitoring, nonlinearity compensation in transmission

system, proactive fault detection, and software-defined networking [32]. Recently, a convolutional neural network-assisted optimization method is proposed to achieve instantaneous frequency estimation over the Brillouin frequency range (10 GHz) and achieve significant accuracy improvement with error within several tens of MHz [33]. However, there is a trade-off between measurement range and tolerance error. Most existing frequency estimation methods could either enable wideband measurement range with relatively low frequency resolution (i.e. a few hundred MHz) or achieve a small error (i.e. tens of MHz) with narrow measurement range.

In this section, we principally and experimentally demonstrated an adaptive instantaneous frequency estimation system based on complementary optical power measurement assisted by deep neural network (DNN). Based on prior experience the intelligent frequency estimation system has, high measurement accuracy as well as high tolerance to device nonlinearity and system noise are achieved. The DNN-assisted frequency estimation system can adapt to dynamic RF transmission condition and significantly decrease the resultant frequency estimation error to 50 MHz with a 1.1-MHz root mean square error over a 14-GHz frequency range.

2.3.2 Operation principle

To perform microwave frequency estimation, the unknown microwave signal-of-interest is modulated onto an optical carrier via an electro-optic intensity modulator (EOM), as shown in Figure 2.8(a). The EOM is biased at the null transmission point to achieve carrier suppressed double sideband modulation (CS-DSB). The CS-DSB modulated optical output is then sent to an optical comb filter pair with complementary spectral responses (i.e. with positive and inverse responses). Therefore, the microwave frequency can be determined by monitoring the filtered optical powers using two optical power meters. Assuming

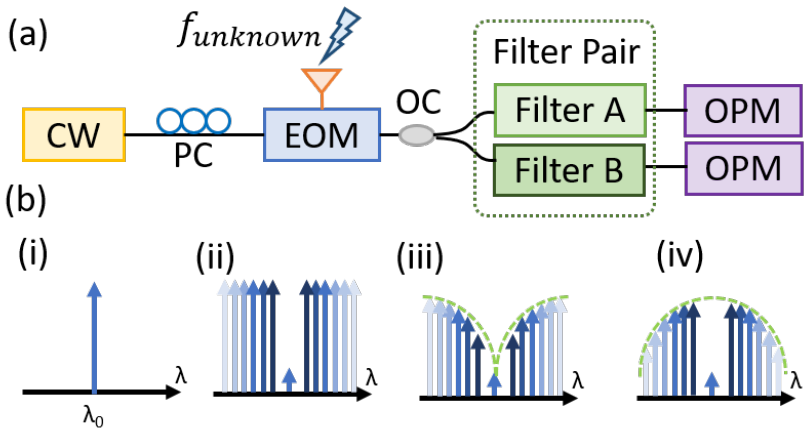

Figure 2.8: Schematic of the basic photonic microwave frequency estimation system. CW: continuous wave; EOM: electro-optic modulator; PC: polarization controller. OC: optical coupler. (b) optical spectra of (i) optical carrier, (ii) CS-DSB signal, (iii) (iv) filter pair (cosine shape).

the input electrical field amplitude is $E_0 exp(j2\pi f_c t)$, the CS-DSB optical signal resulted from an applied microwave signal at frequency f_{RF} can be written as,

$$E_{out}(t) = E_0 \Sigma_n J_{2n}(\beta) cos(2\pi f_c t + 2n \cdot 2\pi f_{RF} t - n\pi) + J_{2n-1}(\beta) cos(2\pi f_c t - (2n-1) \cdot 2\pi f_{RF} t + n\pi) \quad (2.3)$$

where $J_n(.)$ is the n-th Bessel function of the first order. It can be seen that amplitudes of the generated optical sidebands are proportional to the corresponding Bessel functions associated with the modulation depth $\beta = \pi \frac{V_m cos(2\pi f_{RF})}{V_\pi}$.

In conventional optical digital signal processing, the modulating microwave signal power and the nonlinear transfer function of modulator are ignored such that the assumption of the small signal modu-

lation is satisfied, resulting in only the first-order sidebands are being considered in the model. However, high-order sidebands in non-ideal modulation, varying microwave signal power, as well as frequency (in-)dependent optical/RF noise will significantly affect the frequency estimation model in practical. Since the power ratio between the complementary-filtered output is proportional to the summation of the Bessel functions and the two complementary spectral responses, they can be written as:

$$P_{pos} - P_{inv} \propto 10log_{10}\Sigma_n J_n^2(\beta) + 10log_{10}\frac{T_{pos}}{T_{Inv}} + N(\mu, \sigma_{noise}^2) \tag{2.4}$$

where P_{pos} and P_{inv} are the optical power in log scale experiencing positive and inverse transmission responses, respectively. T_{pos} and T_{inv} are the transmission functions of the complementary output of the comb filter. $N(\mu, \sigma_{noise}^2)$ is the unknown instantaneous noise following a Gaussian distribution with mean μ and variance σ_{noise}^2 in the case of central limit theorem [34], which include shot noise, relative intensity noise, and thermal noise.

Conventionally, complementary comb-like spectral response can be obtained easily by putting birefringence medium in an interferometric structure, such that a sinusoidal transfer function can be obtained, as depicted in Fig. 2.9(a) [35],

$$T(dB) = 10log_{10}\left[1 - \gamma cos(\frac{f_{RF}}{FSR})\right] \tag{2.5}$$

where γ, f_{RF},and FSR define the peak-notch contrast ratio, microwave frequency, and free spectral range of the comb filter pair, respectively. However, the resultant spectral response drifts easily with small environmental variations, and the spectral response is sensitive to the polarization of the incident light. Furthermore, the inherent sinusoidal transfer function results in nonlinear mapping between the

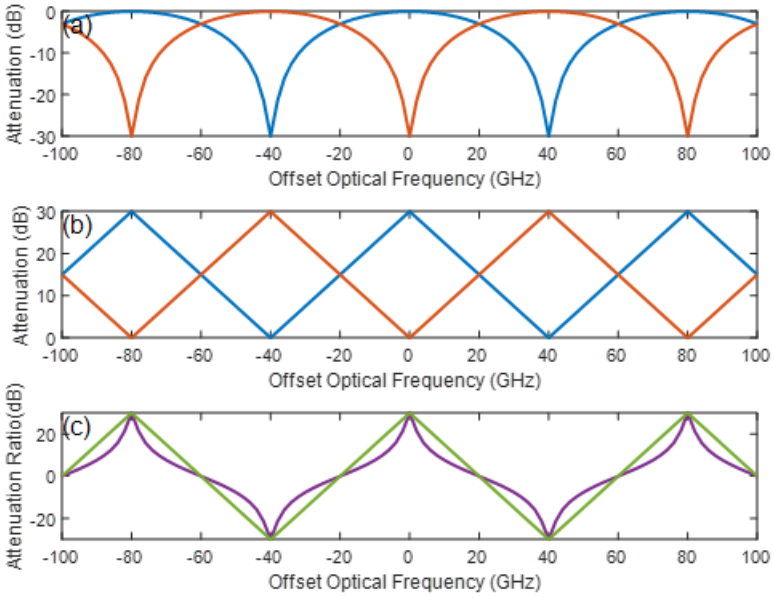

Figure 2.9: Simulated transmission curve comparison. (a) sinusoidal transmission curve (log scale); (b) triangular transmission curve (log scale); (c) attenuation slope comparison between sinusoidal (purple) and triangular (green) transmission function.

optical attenuation ratio and the signal frequency, causing a large error variation especially in the peak and notch regions. To control the complementary spectral responses with large degree of freedom and high stability, a programmable wave shaper [36] is utilized in this work instead. Furthermore, a linear triangular transmission function T (depicted in Fig. 2.9(b)) is used instead of a sinusoidal function to increase the linear range,

$$T(dB) = max(ER - \frac{ER}{FSR/2}|f_{RF}|, 0) \tag{2.6}$$

where ER is the peak-notch extinction ratio of the complementary triangular spectral responses. Figure 2.9(c) shows the simulated attenuation ratio comparison between a sinusoidal spectral response and

a triangular spectral response. It is observed that the attenuation ratio resulted from the triangular spectral function (green) is highly linear over the whole frequency range of interest, while the attenuation ratio resulted conventional sinusoidal spectral function (purple) is merely linear within a narrow spectral range in the middle of the slope. The nonlinear region introduces inconsistent variations in the relationship between the attenuation ratio and frequency relationship over different frequency, resulting in large measurement error variance. To compare the performance between a triangular and sinusoidal spectral function for frequency estimation, we define a new parameter, attenuation ratio slope, which describe both the linearity of the spectral function and measurement resolution. In principle, a constant slope across the frequency range of interest is desired to mitigate the errors resulted from nonlinearity in the spectral function. Figure 2.10 shows the attenuation ratio slope at different FSR and frequency offset from the carrier frequency. The attenuation ratio slope of the triangular spectral function has a constant value over frequency (Fig. 2.10(c)) while the sinusoidal spectral function has inconsistent attenuation ratio slope. (Fig.2.10 (a)). Furthermore, for a given FSR, the attenuation ratio slope is consistent for a large range of extinction ratio (ER) in the triangular spectral response (Fig. 2.10(d)) but varies a lot in the sinusoidal spectral response (Fig.2.10 (b)). Thus, it is inevitable that frequency estimation error is high at low and high frequency ranges than the center frequency ranges in the sinusoidal case, resulting in a frequency estimation model with large mean squared error.

2.3.3 Implementation of deep learning assisted frequency estimation system

Fig. 2.11 (b) shows the block diagram that describes the workflow of the proposed data-driven frequency estimation scheme: First, the collected data are loaded from the database. Then, data preprocessing is applied, which consists of labeling data, cleaning the data by removing the redundant data points, and

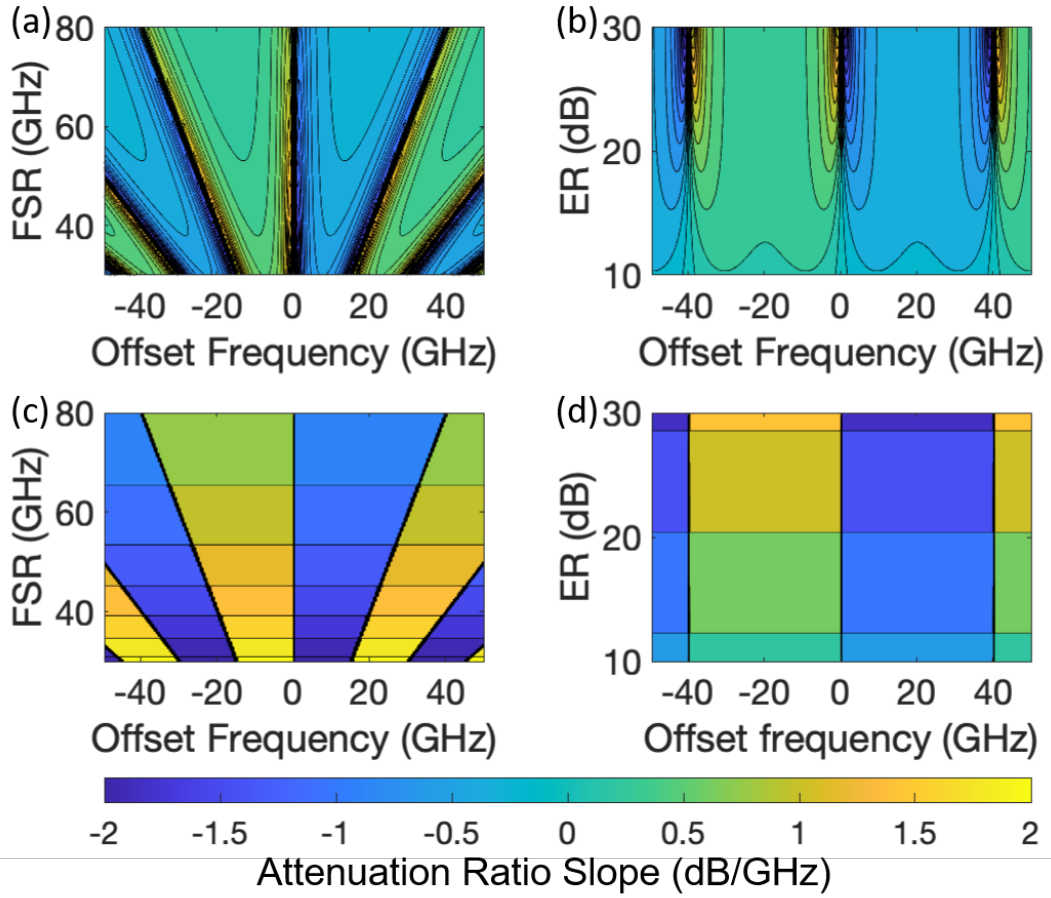

Figure 2.10: Performance comparison between the attenuation ratio slope in sinusoidal and triangular spectral response. (a) sinusoidal with fixed ER; (b) sinusoidal with fixed FSR; (c) triangular with fixed ER; (d) triangular with fixed FSR.

normalize the data. Next, data partitioning is used to split the data into training data and test data. It is worth to notice that 10-fold cross validation is used, such that 10 different randomly divided data partitions are resulted. Lastly, model inference is performed with testing data, and the metrics are calculated once the model is trained using training data.

DNN is uniquely designed to assist the frequency estimation process in our experiment, that utilize information including RF frequency, FSR and ER of the complementary spectral functions, input RF power, and measured optical powers at the complementary spectral responses. To train the DNN, the collected data are partitioned into three parts, 90% for training, 5% for validation, and $5\%$for testing. The designed deep neural network is optimized by adjusting the weights and bias with Levenberg Marquardt regularization. Specifically, the updated weight and bias parameters during each iteration is equal to $-[J^T J + \mu I]^(- 1)J^T e$, where I is the identity matrix, J is the Jacobian matrix that contains the first derivatives of network errors with respect to the weights and biases, and e is the vector of network errors. Before training, the raw data is normalized into a more understandable format that has a standard deviation of 1 with a mean of 0. The proposed data-driven DNN is then trained in a processer with an Intel Xeon CPU E5 3.5 GHz and two NVIDIA Geforce-Quadro-P4000 GPUs. The trained dataset consists of 14896 observations, which is applied to the designed three hidden layer DNN, where each layer consists of 10, 20, and 5 neurons, respectively.

Figure 2.11(a) shows the experimental setup of the proposed data-driven frequency estimation system that consists of two parts: a complementary optical power measurement unit and a deep neural network for frequency estimation. To achieve complementary optical power measurement, a distributed feedback laser (DFB) centered at 1549.275 nm is used as the optical carrier. To collect training data, the RF signal of interest that is sweeping from 1 to 16 GHz with a step of 200 MHz is used. The RF signal is then

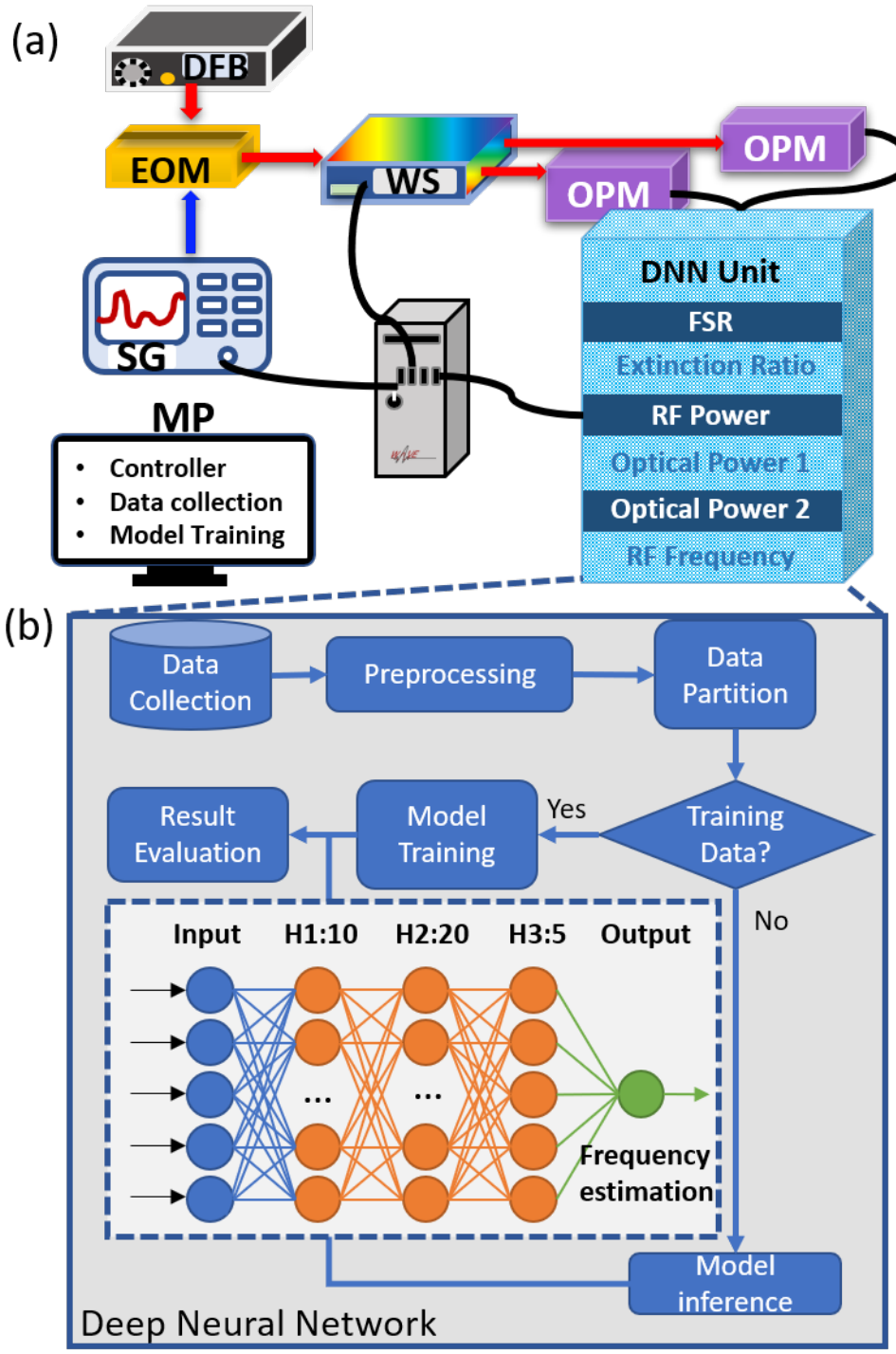

Figure 2.11: The proposed data-driven photonic microwave frequency estimation system with improved resolution and immunity to system nonlinearity. (a) Experimental setup. DFB: distributed feedback laser; EOM: electro-optic modulator; SG: signal generator; WS: optical wave shaper; OPM: optical power meter; MP: microprocessor; DNN: deep neural network; (b) structure of the designed DNN, and the overall block diagram showing the workflow of the proposed data-driven evaluation methods.

modulated onto the optical carrier using a 10-Gb/s electro-optic intensity modulator (EOM). The EOM is biased at the null transmission point to achieve CS-DSB modulation, as shown by the blue curve in Fig. 2.12(a). The CS-DSB optical signal is then passed through the pair of triangular complementary spectral responses (orange curve in log scale) at the optical wave shaper. Triangular response is used to ensure the power difference between the two measured complementary power is proportional to the signal frequency. Transmission outside of the triangular cycle is set to zero for removing optical noise and undesired high frequency harmonics generated during electro-optic modulation. Fig. 2.12(a) shows the triangular spectral response with variable FSR and ER. In our experiment, FSR ranges from 40 GHz to 70 GHz with step resolution of 5 GHz is used. A larger FSR supports a wider frequency estimation range but would results in a lower frequency resolution. Frequency resolution can be improved by increasing the ER of the triangular spectral response. ER ranges can be set from 15 dB to 30 dB with 5 dB step size. To enable signal power transparent frequency estimation, training data with RF power from -10 dBm to 2 dBm and increment of 2 dB is used to train the DNN model. A quasi-linear relationship is observed in the measured complementary optical powers obtained through the two triangular complementary spectral responses, as shown in Fig. 2.12(b).

2.3.4 Results and Discussion

To evaluate the performance of the trained model, histogram of the absolute error between the predicted and actual RF frequency is shown by the yellow bars in Fig. 2.13(a), which is less than 50 MHz. The histogram of the training and validation processes are also shown in blue and orange in Fig. 2.13(b) for comparison. In addition, the calculated RMSE is 1.1 MHz, which correspond to only 0.5% of the RF frequency sweeping step resolution. The regression performance plot between predicted and the actual

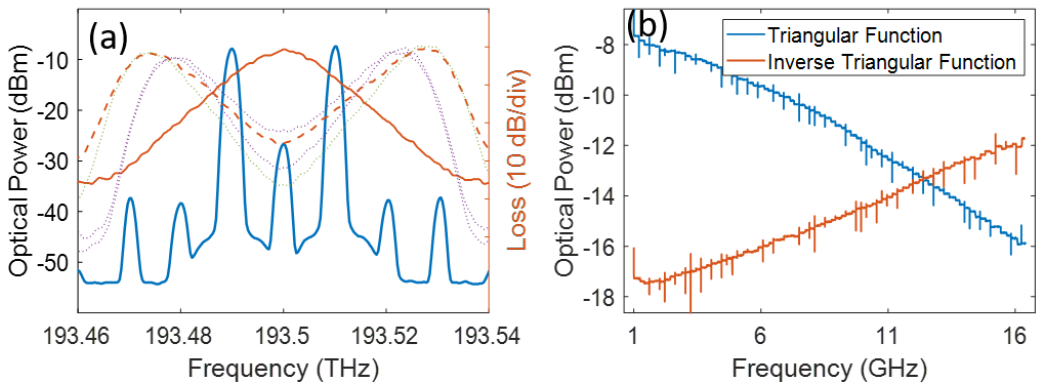

Figure 2.12: Examples of various measurement using one setting: (a) Measured optical spectra of CS-DSB signal (blue); complementary triangular transmission curves (orange solid and dash), transmission curves with tunable FSR and ER (purple dotted curves); (b) measured optical power at different RF frequency (RF power = 0 dBm, ER = 15dB and FSR = 0.05THz).

RF frequency with respect to the training, testing and validation dataset is shown in Fig. 2.13(b). The calculated R2 value is 99.94% among all groups of data, indicating a goodness of fit of the proposed DNN model. The DNN-assisted frequency estimation system works well even under dynamic user-defined settings with unknown frequency.

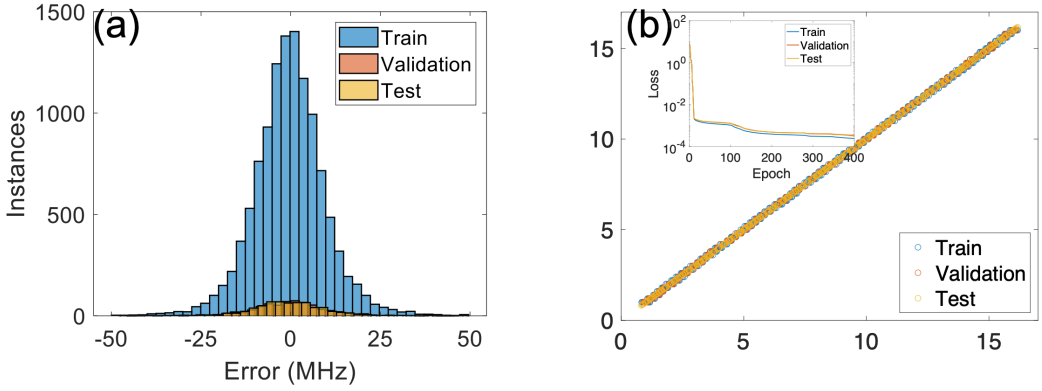

Figure 2.13: (a) Model error distribution among train, validation, and test data; (b) model evaluation with R2 equal to 0.9994 (inset: train, validation and test loss curves).

To evaluate the performance of the trained DNN, we apply the new input data to obtain the estimated frequency and compare the result with the actual frequency. In Fig. 2.14(a), the thick blue line represents the estimated frequency, which matches well with the actual frequency (thin red line). The corresponding preset RF powers, FSRs, ERs, and measured optical powers are also shown in Fig. 2.14(b)-(c). The estimated results has a measurement error of less than 50 MHz, proving the successful implementation of DNN-assisted microwave estimation.

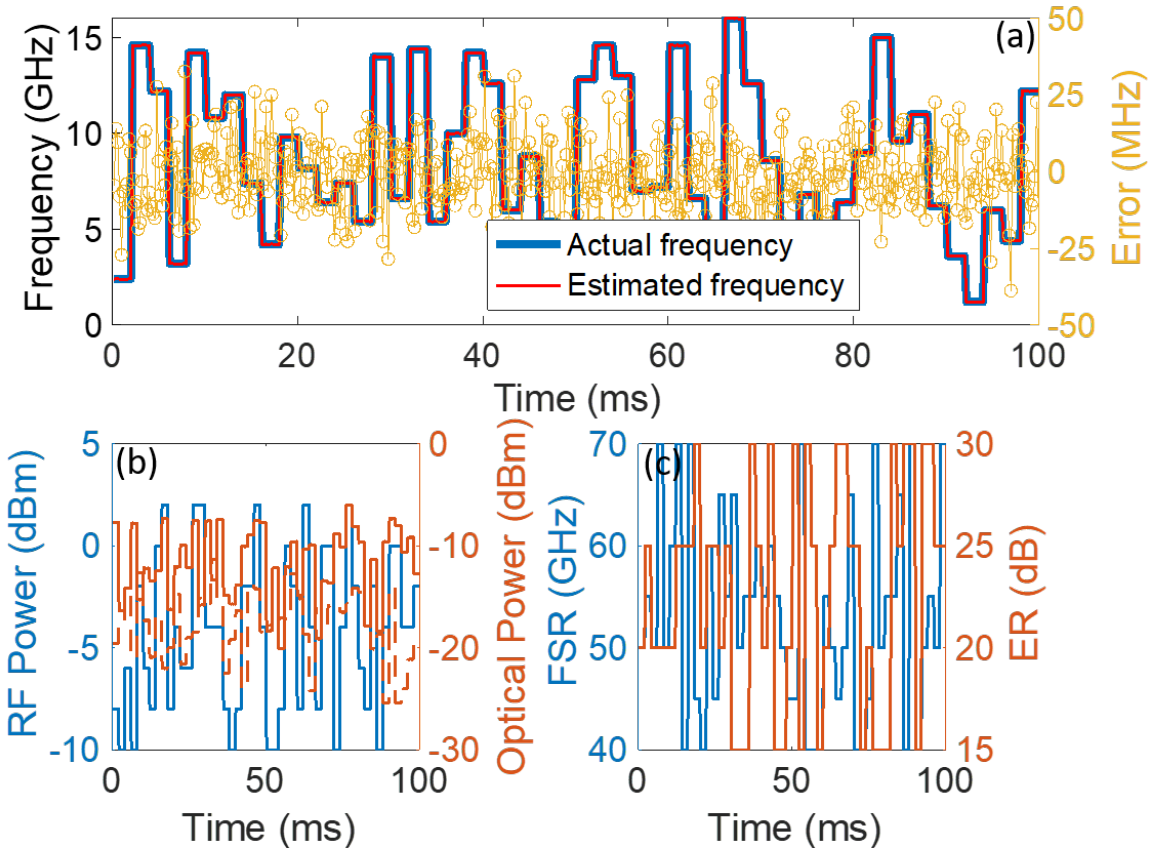

Figure 2.14: Performance evaluation: Estimated frequency and true frequency at different system settings. (a) the estimated frequency and true frequency; (b) preset RF power and measured optical power at complementary triangular spectral functions; (c) preset FSRs and ERs.

2.4 Summary

In summary, in this chapter, we developed two dynamic photonics-enabled instantaneous RF measurement systems. In the first scheme, a dual-function microwave photonic system that can measure both RF instantaneous frequency and Doppler frequency shift is experimentally demonstrated using a phase modulator incorporated Lyot loop filter. With the incorporation of phase modulator, dynamic adaptation to measurement range and resolution can be obtained. A 2.7 dB/GHz of resolution enhancement is achieved for frequency measurement. Complete carrier suppression is achieved to mitigate measurement error in Doppler frequency shift and to double the spectral resolution.

With the help of machine learning methods, a data-driven instantaneous frequency estimation system based on complementary optical power measurement is also demonstrated. The absolute measurement error is significantly reduced to 50 MHz with a RMSE of only 1.1 MHz. Compared with the methods without transmission curve improvement and machine learning, the designed DNN-assisted frequency estimation system could solve the precision issues resulted from system noise and device nonlinearity, as well as overfitting problem in most conventional frequency estimation methods. Unlike conventional frequency estimation scheme, the proposed frequency estimation model works well for both pre-known and un-known data. With DNN training, the measurement error is significantly improved through the training and validation process, which also results in high adaptability to unknown RF signal properties.

Chapter 3

High-Speed Multidimensional Radio Frequency Signal Switching

Due to the increasing demands of information security and high data fidelity in counter-measurement for military applications, as well as high data capacity requirement in emerging RF communications, there is a critical need for real-time switching of high-speed RF signal [37], [38]. Applications of high-speed switching of RF signal includes signal routing, amplitude and phase modulations, frequency hopping signal generation, and multi-dimensional modulation, as illustrated in Fig. 3.1. Among them, ultrafast frequency switching for frequency hopping (FH) signal generation is of particular interest due to its unique advantages such as immunity to inter-symbol interference and anti-jamming capability that are essential in modern RF systems [39], [40]. To date, high-speed switching of RF signal amplitude is easy to achieve using electro-optics modulators and optical mixing techniques [41], [42]. However, it is always

challenging to switch the phase or frequency of an RF signal with fast switching time, i.e. the 10 % - 90 % rise/fall time for the output to switch from one frequency/phase to another. Electromechanical switches and microelectromechanical systems (MEMS) switches have switching time in the range of microsecond; while solid-state switch has a switching time of nanosecond due to the intrinsic physical properties and switching mechanism of electronic devices [6], [43], [44].

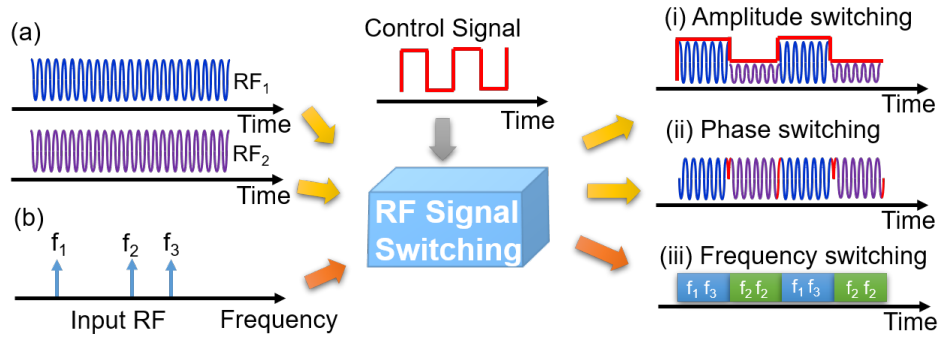

Figure 3.1: Applications of high-speed RF signal switching. (a) Two continuous wave input for (i) amplitude switching and (ii) phase switching; (b) Multiple frequency input for (iii) frequency switching.

3.1 Ultrafast and Wideband Microwave Photonic Frequency Hopping System

[1] The increasing demands for enhancing information security in data transmission, providing countermeasure against jamming in military applications, as well as boosting data capacity in mobile and satellite communication lead to a critical need for high-speed frequency hopping systems. Conventional electronics-based frequency hopping systems suffer from low data rate, low hopping speed, and narrow hopping frequency bandwidth, unfortunately, those are important aspects to facilitate frequency hopping in emerg-

[1] **Q. Liu**, M. P. Fok. "Ultrafast and Wideband Microwave Photonic Frequency-Hopping Systems: A Review." Applied Sciences, 10.2 (2020): 521.

ing microwave systems. The recent advancement of microwave photonics – the use of light to process microwave signals, provides promising solutions to tackle the challenges faced by electronic frequency hopping systems. In this section, the challenges of achieving real-time frequency hopping systems are examined. The operation principles and results of various microwave photonics enabled frequency hopping systems are briefly discussed, that have wide hopping frequency range and frequency hopping speed of as fast as tens of picoseconds.

Frequency hopping systems, which change the information carrier frequency between a series of frequencies determined by a unique hopping code sequence (Figure 3.2), has always attracted great interest in radar and satellite systems, wireless radio frequency (RF) communications, as well as emerging dynamic communication systems (i.e. 5G/6G) [39]. The history of frequency hopping was dated back to 1941, which was patented by a Hollywood actress Hedy Lamarr and pianist George Antheil. The technology was not taken seriously in electronic countermeasure worldwide until 1980s. With the merit of frequency hopping systems, such as mitigating the effects of inter-symbol interference and jamming, it significantly increases the communication capacity of emerging RF wireless systems - making it an essential tool to fulfil the high RF spectral resources demand in the commercial, defense, and civilian federal marketplace [40], [45], [46]. Furthermore, the fast frequency hopping capability greatly increases the security of wireless services – the lack of fast changing in carrier frequency make it challenging for Eve to interpret the information. Moreover, signal interference resulted from multi-path effect could be largely reduced by the fast-changing frequency carriers. Frequency hopping systems have been widely implemented, for examples, in Bluetooth [47], Advanced Extremely High Frequency (AEHF) communication satellites [48], and the Military Strategic and Tactical Relay (MILSTAR) communication satellites [49]. Although frequency hopping systems have been proved successfully in various RF systems, the hopping speed

is limited to milliseconds, and the hopping frequency range is less than several GHz, which hinder its implementation in emerging RF wireless communications and sophisticated electronic warfare systems. Due to the inherent electronic bottleneck and available frequency bandwidth of the electronic devices, it is very challenging for electronics-based frequency hopping system to achieve hopping frequency bandwidth over several GHz in close to real-time hopping speed.

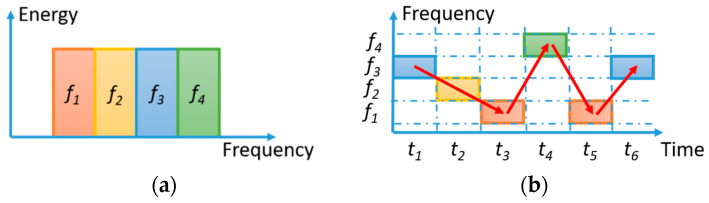

Figure 3.2: Principle of frequency hopping communication systems. (a) Frequency channel assignment for a single user; (b) Time-varying spectral usage of the allocated frequency for a particular user.

Microwave photonics (MWP), which bridges radio frequency signal and photonic signal processing, is capable of overcoming bottlenecks in electronics due to its large bandwidth, instantaneous response, as well as flexibility and reconfigurability [17]. Various challenging RF signal processing tasks have been successfully demonstrated using photonic technologies [24], [35], [50]–[52], such as microwave photonic analog to digital converters, microwave photonic filters, microwave photonic arbitrary waveform generators, to name a few. Although microwave photonic approaches are capable of generating various types of RF signals [53], it is not trivial to utilize them for generating frequency hopping signals due to the limited frequency tunability and hopping speed in the existing signal generating approaches, as well as the time required to stabilize at the desired frequency.

In recent years, there are several attempts of designing microwave photonic frequency hopping systems with wider hopping bandwidth and roughly 103-106 times faster hopping speed when compared with conventional electronic approaches. Figure 3.3 shows an illustration of a microwave photonic frequency

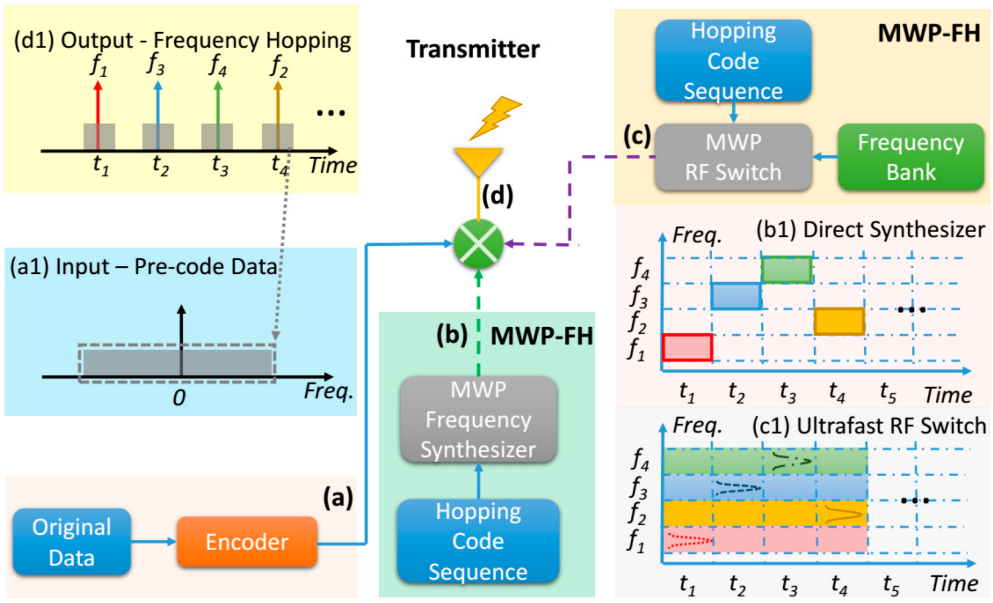

Figure 3.3: Schematic of microwave photonic frequency hopping transmission systems. (a) Input-encoded data at baseband; (b) Ultrafast MWP based frequency synthesizer controlled by an applied hopping pattern. (c) Frequency hopping carrier generation using MWP RF switch (d) Output – frequency hopping signal.

hopping system that consists of (a) a pre-encoded input data module, and (b)/(c) a frequency hopping carrier generation module for generating the uplink carrier. The pre-encoded input data is used to modulate the RF carrier and then transmitted through a high-frequency antenna as a frequency hopping signal. There are mainly two types of MWP frequency hopping carrier generation schemes, including (i) MWP frequency synthesizer with ultrafast frequency switching ability, such as the use of nonlinear period one dynamics of injected semiconductor laser to directly generate different frequency at different time [15,16]; (ii) MWP switch for fast switching of pre-generated frequencies, such as the use of ultrafast microwave photonic RF filter to switch out different frequency carriers.

There are two major challenges in MWP frequency synthesizer approach: First, a stable desired frequency is needed to be established in a short period of time to enable fast frequency switching; second, the

precise control of the hopping code sequence properties due to the required tight relationship between the synthesized frequency and the applied hopping code sequence. In MWP RF switch approaches, the two major challenges are: (i) to achieve fast-switching time within a cycle of the carrier, and (ii) completely switch off the unwanted frequencies. Needless to say, for both approaches, it is even more challenging to achieve a multi-level frequency hopping system with picoseconds hopping speed and instantaneous reconfiguring capabilities. Table 3.1 shows a list of examples of the state-of-the-art frequency hopping signal generation schemes based on various RF electronics and microwave photonic approaches.

Recent advancement in microwave photonic frequency-hopping schemes enable hopping speed ranging from picoseconds to nanoseconds and the hopping-frequency bandwidth over tens of GHz with hopping stability. Moreover, some of the microwave photonic approaches could be used for multi-level frequency-hopping, including flexible OEOs, tunable MWP filters, and nonlinear period-one dynamics in lasers. To achieve both multi-level frequency-hopping and fast switching speed, multiple frequency-hopping approaches with fast switching time could be incorporated together to increase the level of frequency-hopping while maintaining the high hopping speed.

The rapid development of real-time frequency-hopping speed as well as the transparency of data formats, frequency, phase and amplitude in the frequency-hopping system could be potentially used in the future THz wireless communication and be used in any wireless communication transmission scenario. Looking forward, the practical application of microwave photonic frequency-hopping system can be further improved and optimized through miniaturization, integration, and incorporating intelligence to adapt to more sophisticated wireless communications.

Table 3.1: Comparison of the State-of-the-Art Frequency-Hopping Signal-Generation Schemes

Reference	Techniques	Speed	Potential for Multi-level	Methods	Tuning Mechanism
[54]	Four wave mixing (our approach)	50 ps	No	switch	Polarization tuning
[55]	SBS filter	100 ps	Yes	switch	SBS tuning
[56]	EO-based comb filter	100 ps	Yes	switch	EO Pockels effect
[29]	Notch filter	190 ps	No	switch	EO Pockels effect
[57]	Lyot filter	200 ps	Yes	switch	Nonlinear polarization rotation
[58]	DD-MZM bias control	1 ns	No	switch	EO Pockels effect
[59]	Optical injection	10 ns	Yes	synthesizer	Nonlinear dynamics
[60]	Delay line-based comb filter	40 ns	Yes	switch	Optical delay line
[61]	PM-PSFBG OEO	100 ns	Yes	synthesizer	Polarization tuning
[62]	Microring resonator	500 us	Yes	synthesizer	Thermal tuning
[44]	RF-MEMS	300 us	Yes	switch	MEMS capacitor
[63]	Integrated spectrum shaper	7 ms	Yes	switch	Thermal tuning

3.2 Real-time Multidimensional Radio Frequency Signal Switching

[2] Real-time switching of RF signal properties, including phase, frequency, and amplitude, is essential for emerging high-speed RF systems to improve security, signal fidelity, and enhance data capacity. While it is easy to switch the amplitude of an RF signal at GHz speed, unfortunately, it is extremely challenging to perform phase or frequency switching of an RF signal with a fast switching time in the picosecond range. In this section, a real-time RF signal switching technique is proposed and demonstrated based on polarization dependent four-wave mixing in a highly-nonlinear optical fiber. Due to the amplitude, phase, and frequency transparent property of four-wave mixing, the proposed scheme is capable of manipulating multidimensional RF signal of over tens of GHz frequency, and achieve frequency hopping and phase switching of a GHz RF signal. The switching time is not limited by the proposed temporal switching technique; instead, it is solely depending on the rise/fall time of the control signal itself. The generation of frequency hopping signal with a switching time of 50 ps, as well as simultaneously frequency and phase switching of a GHz RF signal have been experimentally demonstrated based on the proposed RF signal switching scheme.

[2] **Q. Liu**, M. P. Fok. "Real-Time RF Multi-Dimensional Signal Switching Using Polarization-Dependent Optical Mixing ", IEEE Photonics Journal, 12.2 (2020):1-8.

3.3 The Implementation of Four Wave Mixing to Signal Switching

3.3.1 introduction

Microwave photonic approach is a promising candidate to achieve high-speed RF signal switching of various signal properties. A number of frequency hopping signal generation schemes have demonstrated switching speed of up to hundreds of picoseconds. For example, the use of a polarization maintenance-phase shift fiber Bragg grating based optoelectronic oscillator (OEO) [61] can achieve FH signal with hopping speed of 0.1 ms, limited by the time for the establishment of a stable oscillation. Hopping speed of 10 ns can be achieved through the control of an optically injected semiconductor laser [59], while the control of bias voltage of a dual drive Mach–Zehnder modulator (DDMZM) enables 1 ns switching speed [58]. The use of microwave photonic filters [29], [55], [56], [60], [62], [64], including stimulated Brillouin scattering based [55] and comb filter based [56] techniques for generating fast-switching frequency hopping signal can achieve hopping speed of hundreds of picoseconds. On the other hand, photonic-assisted microwave signal mixing for amplitude and phase-switching signal generation can be implemented via stimulated Brillouin scattering (SBS)-based carrier suppression [65], the use of phase coherent orthogonal carrier [66], polarization rotation in semiconductor optical amplifier [67], and the use of Sagnac loop based modulator [68]. However, most existing microwave photonic approaches require the use of optical filters, electrical phase shifters, which essentially limits both the lower and upper operation signal frequencies.

In this section, we propose and demonstrate a novel microwave photonic technique to achieve real-time switching of various RF signal properties, including frequency and phase switching, as well as am-

plitude modulation over a wide operation frequency range. Polarization-dependent four-wave mixing (FWM) is utilized in the proposed scheme, which has instantaneous response time and is frequency, phase, and amplitude transparent [69], enabling RF signals switching with potentially zero transition time. Fiber optics based FWM has been widely investigated for wavelength conversion, signal multicasting, supercontinuum generation, signal regeneration, logic operation, frequency comb generation, optical phase conjugation as well as fiber-optic parametric amplification [70]–[72]. In most of these applications, the polarization sensitive property in FWM is a disadvantage that would degrade the performance of the systems. Most of the time, polarization diversity or other polarization managing techniques have to be implemented to guarantee efficient FWM to occur. In this work, instead of mitigating the polarization sensitive property of FWM, we take advantage of the property and combine it with the FWM transparency characteristic to achieve real-time RF signal switching of multi-dimensional signal properties. We have experimentally demonstrated the generation of FH signal with hopping speed of 50 ps – which is the fastest so far to our knowledge, that solely limited by the rise/fall time of the electrical control signal. A comparison of switching speed and the potential of multilevel frequency switching for various approaches are shown in Table 3.1. Unlike other approaches that has a tight requirement on the relationship between the frequencies for switching [55], [58], our proposed scheme enables flexible choices of frequency usage for the generation of FH signal. Furthermore, the proposed technique works well for microwave signal mixing of both amplitude and phase modulations without the need of hybrid electrical devices for single sideband modulation [67], [68] or complicated off-line phase compensation [73].

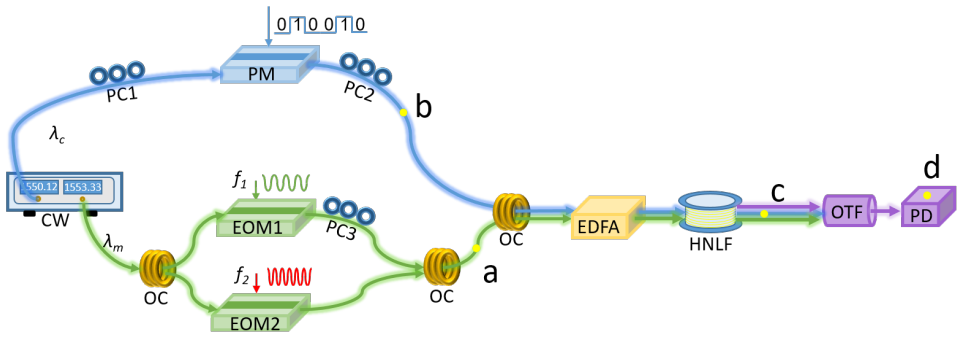

Figure 3.4: Experimental setup of the proposed RF signal switching system. OC: optical coupler; PC1-3: polarization controllers; PM: phase modulator; EOM1-2: electro-optic intensity modulator; EDFA: Erbium-doped fiber amplifier; HNLF: high nonlinear optical fiber; OTF: optical tunable filter; PD: photodetector.

3.3.2 Experimental details

Fig. 3.4 illustrates the experimental setup of the proposed real-time RF signal switching scheme based on polarization dependent four-wave mixing. Two laser sources (ILX 7900B) at 1550.12 nm (λ_c) and 1553.32 nm (λ_m) are used as the optical carriers for the control signal and microwave signals, respectively. The control signal generated from a high-speed pattern generator (Agilent N4906B) is modulated onto the polarization of the optical carrier at λ_c via a 10-Gbps phase modulator (EOSpace-LN-52S). A phase modulator can be used for polarization modulation by aligning the optical carrier at 45° with respect to the principal axes (x and y) of the phase modulator waveguide [74]. Thus, the modulated optical control signal E_{PM} after polarization modulation can be expressed as,

$$E_{PM} = \begin{bmatrix} E_x \\ E_y \end{bmatrix} = \frac{\sqrt{2}}{2} E_0 e^{j\omega_0 t} \begin{bmatrix} cos(\beta c(t)) \\ sin(\beta c(t)) \end{bmatrix} \tag{3.1}$$

where E_x and E_y are the amplitude of the modulated optical control signal at x and y polarization, respectively, while E_0 and ω_0 are the amplitude and angular frequency of the optical carrier at the output of the PM. In equation 3.1, the modulation efficiency is $\beta = \pi V_c/2V_p$, where V_c is the amplitude of the binary control signal $c(t)$, and V_p is the half-wave voltage of the PM. Therefore, by properly adjusting the control signal voltage applied to the PM such that $\beta = \pi/2$, polarization of the input light wave will be set to x or y directions during bit 1 and bit 0 of the control signal, respectively, resulting in a complementary pattern on separate polarization states as illustrated in Fig. 3.5(b).

The optical carrier at λ_m is split into two branches and is intensity modulated by two microwave signals at f_1 and f_2, which are then set to have orthogonal polarization before combining at the optical coupler. It is important to note that the intensity modulator (JDSU OC-192) has 3-dB bandwidth of 14 GHz, which limits the upper frequency of the input RF signals. The two intensity modulated optical signals and the polarization modulated optical control signal are then combined by optical coupler (OC) and amplified by an Erbium-doped fiber amplifier (EDFA) to 18.5 dBm to ensure FWM is induced in the dispersion shifted highly nonlinear optical fiber (HNLF). The 200-m HNLF has dispersion slope of 0.022 $ps/(nm^2 \cdot km)$ and nonlinear coefficient of $20/(W \cdot km)$ in the vicinity of 1550 nm. Since FWM is a polarization sensitive process, polarization controllers (PC) are used to ensure the polarization is optimized to obtain the best switching RF outputs. Specifically, polarizations of the optical signal at f_1 and f_2 are set to x and y, respectively, which are orthogonal to each other. In degenerate FWM, FWM efficiency is the strongest if the polarization of the two signals are the same, while no FWM occurs if the polarization of the input signals are orthogonal. Therefore, x-component of the optical control signal, i.e. all the bit 1 in the control signal, will undergo FWM only with the x-polarization branch of λ_m (modulated at f_1), as shown in Fig. 3.5(c)i, resulting in f_1 only appears during bit 1 of the control signal (Fig. 3.5(c)iii).

On the other hand, y-component of the optical signal, i.e. all the bit 0 in the control signal, will undergo FWM only with the y-polarization branch of λ_m (modulated at f_2), as shown in Fig. 3.5(c)ii, resulting in f_2 only appears during bit 0 of the control signal (Fig. 3.5(c)iv). Then, an optical tunable filter with 0.5 nm bandwidth is set at 1556.52 nm to extract the FWM output, while a 10-Gbps photodetector (PD) is used to convert the FWM output into an electrical RF signal. A 30-GHz dual channel electrical oscilloscope (Keysight 86100D) is used to observe the temporally stitched RF signal. Thus, f_1 and f_2 are temporally stitched together into "$f_2, f_1, f_2, f_2, f_1, f_2$" when a control signal $c(t) = 010010$ is used, as shown in Fig. 3.5(d).

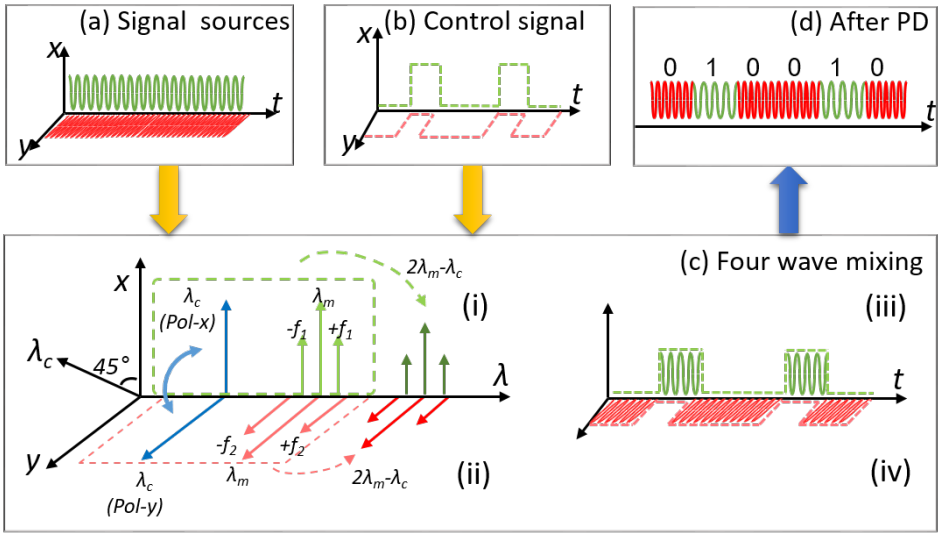

Figure 3.5: Operation principle of the proposed real-time RF signal switching system for FH signal generation using four-wave mixing; (a) RF signals at f_1 and f_2 modulated on λ_m at x- and y- polarizations; (b) Control signal after phase modulator; (c) FWM process at x- and y-polarization; (d) Frequency hopping signal generated through RF signal switching.

3.3.3 Results and discussions

In our experiment, we first experimentally demonstrate the use of the proposed RF signal switching technique for generating a real-time frequency hopping signal. Two sinusoidal RF signals with f_1 = 5

GHz and f_2 = 8 GHz are applied to intensity modulators EOM1 and EOM2 , respectively. A frequency hopping control signal of "1011010010" at 1 Gbps is used to control the PM. The FWM output at 1556.52 nm carries the resultant frequency hopping signal, with a FWM conversion efficiency of -20 dB. After photo-detection, the frequency hopping signal follows the correct hopping sequence of "1011010010", as shown in Fig. 3.6(a). A clean frequency hopping between 5 GHz and 8 GHz is observed with uniform amplitude profile. From the zoom-in view of the frequency hopping signal (inset of Fig. 3.6(a)), no significant switching time is observed at the intersection between the 5-GHz and 8-GHz sections. The spectral pureness of the frequency hopping signal is determined by the ability to completely switch off the undesired frequency component. To observe how good each of the frequency component is being switched out, a polarization beam splitter with 500:1 extinction ratio is used to separate the x- and y-polarization components of the FWM output. To optimize the system performance, precise polarization adjustment is performed at the very beginning of the experiment. As shown in Fig. 3.6(b) and (c), a pure 5-GHz signal with pattern "1011010010" is detected through x polarization and an 8-GHz signal with complementary pattern "0100101101" is observed on y polarization. No residual signal is observed during their corresponding switching-off time. Since FWM has instantaneous response, the only limitation of the switching speed is the rise/fall time of the control signal and the modulator bandwidth.

To investigate the switching time of the RF signal switching process, the two microwave signals f_1 and f_2 are removed, leaving just the two orthogonally polarized CW light at λ_m and the optical control signal at λ_c for FWM. A polarization beam splitter is used to separate the FWM output into x- and y-polarizations, as shown in Fig. 3.6(d) and (e), respectively. The rise/fall time of each polarization component in the FWM output indicate how fast the proposed signal switching system can be realized between the input microwave signals. Fig. 3.6(f)i-ii are the zoom-in view of the 10% to 90% rise and fall time, showing a 50

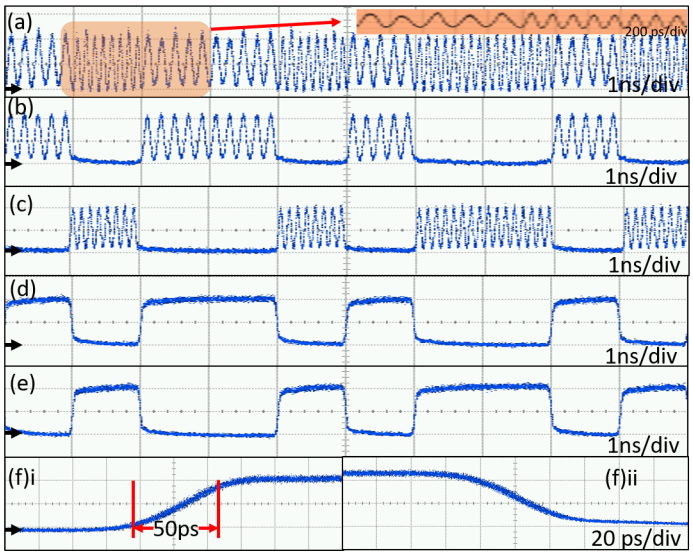

Figure 3.6: (a) Generated FH signal with hopping frequency of 5GHz and 8GHz when a "101101001o" control signal is used, inset: zoom-in waveform of the orange shaded area; (b)(c) Temporal waveforms of the 5 GHz and 8 GHz RF signals when a control signal of "101101001o" is used; (d)-(e) FWM outputs at x- and y-polarization when no RF signals are used; (f) Response time measurement for i) Rising and ii) Falling edge. (black arrow: zero voltage)

ps switching speed for both rising and falling edges, governed by the rise/fall time of the control signal and the modulator bandwidth. Switching time of 50 ps is the fastest to date, thanks to the instantaneous response time of FWM. Since FWM process is frequency independent, the proposed RF signal switching scheme also works well for a wide range of frequency. Fig. 3.7(a) shows the waveform of a frequency hopping signal consists of 3-GHz and 10-GHz frequencies with a 20 bits frequency hopping pattern "11101000110101100100" as the control signal. The spectrogram representation is measured and is shown in Fig. 3.7(b), while the retrieved instantaneous frequency is shown by the red curve.

While FWM is a polarization-dependent processing, it is amplitude, phase, and frequency transparent. Therefore, the proposed RF signal switching technique can be used for microwave signal mixing. Instead of using f_1 and f_2 to modulate the orthogonal light beams at λ_m, one of the EOM is disabled and a

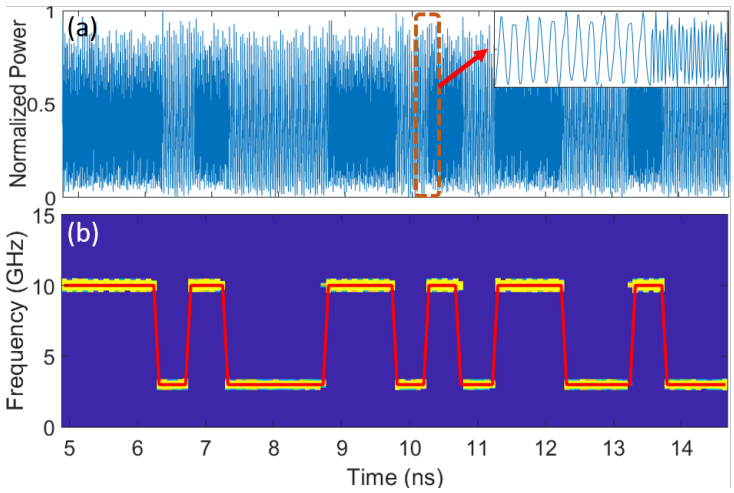

Figure 3.7: (a) Measured FH signal between 3 GHz and 10 GHz with a 20 bits hopping pattern "11010001101011001001"; (b) Spectrogram representation of the FH signal and the corresponding retrieved frequency pattern in red curve.

local oscillator (LO) signal at 10 GHz is used for modulating the second intensity modulator to achieve signal mixing. In our experiment, a 1 Gbps $2^{15} - 1$ pseudo-random bit sequence (PRBS) is used as the intermediate frequency (IF) signal, and is used to modulate the polarization of λ_c using the PM. When the polarization of the LO-modulated light is aligned with that of the IF-modulated light, on-off-keying (OOK) modulation is achieved and a widely open eye diagram with extinction ratio of 12.9 dB is observed as shown in Fig. 3.8(a). By setting the polarization between $0°$ and $90°$, amplitude shift keying (ASK) modulation of the LO at 10 GHz with various extinction ratio can be obtained. The clarity of the eye diagram is consistent throughout the tuning of extinction ratio. Fig. 3.8(b) shows an example of a widely open eye diagram of a ASK signal with 3.9 dB extinction ratio.

Next, we investigate the ability for phase modulation – binary phase shift keying (BPSK) of microwave signal. BPSK can be achieved by either biasing the two intensity EOMs at opposite transmission slope or applying a relative delay between the two driving RF signals applied to the EOMs, such that the two

modulated orthogonal optical signals at λ_m is phase-offset by π. An IF at 1 Gbps and bit pattern of "1010" is used. The RF signal switching system successfully generated a phase modulated signal according to the IF, as shown in Fig. 3.8(c). The waveform of the phase modulated signal clearly verifies the 0 and π shift during bit 0 and bit 1, corresponding to the two phase transitions indicated by the red circles. Due to the phase and frequency transparency of FWM, the proposed RF signal switching technique can offer multiple dimensions for signal modulation, i.e. simultaneously phase and frequency modulation. Fig. 3.8(d) shows a phase shifted RF signal that also has its carrier frequency hopping between 5 GHz and 10 GHz.

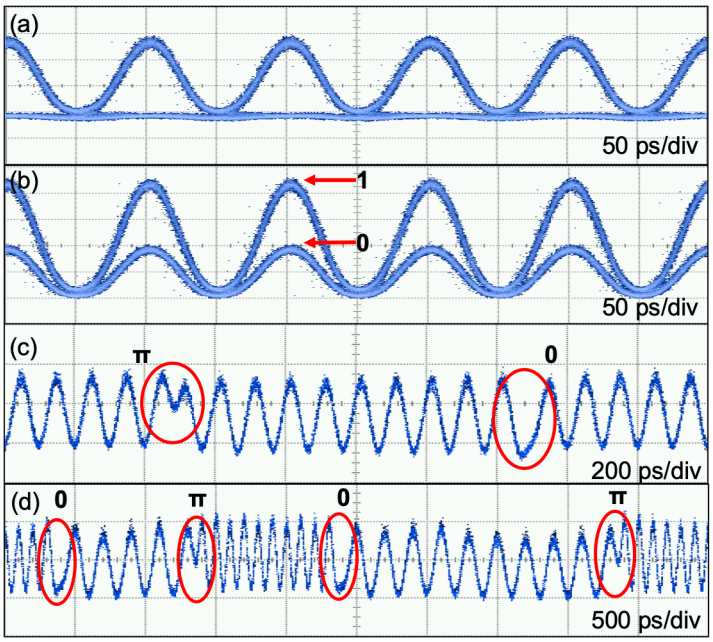

Figure 3.8: (a) Eye diagram of a PRBS OOK modulation at 1 Gbps; (b) Eye diagram of PRBS ASK modulation at 1 Gbps; (c) Waveform of 1 Gbps phase switching of a 10 GHz LO. (d) Waveform of 1 Gbps phase modulation of a dual-frequency LO at 5 GHz and 10 GHz.

3.4 Summary

In summary, we proposed and experimentally demonstrated a real-time RF signal switching technique that has instantaneous response time and a wide operation frequency range of tens of GHz. The approach utilized the polarization-dependent nature as well as phase and frequency transparent properties of four wave mixing to achieve fast switching time for frequency hopping signal generation and signal mixing with various modulation formats. RF signal switching technique can be used to generate frequency hopping signal with instantaneous switching speed to improve security and signal fidelity of high capacity RF systems. Switching speed of 50 ps is experimentally observed, which is governed by the rise/fall time of the electrical control signal and bandwidth of the electro-optic modulator. It is worth to notice that approaches that could potentially be translated to multilevel frequency switching are desired to provide a more complex hopping pattern and further improve information security during transmission. The proposed FWM based signal switching scheme could be cascaded with another FWM stage or combined with other frequency switching scheme to perform multilevel frequency switching due to its frequency transparent property. Although not all existing approaches could potentially achieve multi-level frequency switching, a few of the existing approaches including flexible OEOs, tunable MWP filters, and nonlinear period one dynamics are able to do that, which is summarized in Table 1. Looking forward, the practical implementation of microwave photonic frequency hopping system can be further enhanced by integration, reconfiguration, and intelligentization to adapt to dynamic, and complex wireless communication scenarios.

Chapter 4

Dynamic and Heterougenous Radio Frequency Spectral Properties Tuning

Emerging RF communication systems and satellite systems utilize the transmission of multiband frequency signals to support multi-function service and to enable the system to adapt to changes dynamically [14], [75]–[77]. Due to the heterogeneous and dynamic nature of modern RF systems, multiband RF filters with independently controllable passbands and heterogeneous spectral properties are critical to support flexible and dynamic multiband RF systems. With existing RF electronics based RF filters, it is very challenging to achieve multiband filtering, as well as the ability to tune the properties of each passband. These tasks are difficult to achieve because of the relatively narrow bandwidth supported by RF electronics, the inherent low-tunability characteristic of RF electronics, and the challenges to satisfy the design parameters for all passbands [78], [79]. For state-of-the-art electronics based RF multiband

filters, only a few have been realized with limited frequency tunability [80]–[82]. Although electronic approaches offer on-chip solutions [83], it is impossible to independently tune the properties of each passband.

Microwave photonic (MWP) approaches have been a promising candidate to tackle a number of challenges in RF electronics due to its unique properties – wide operation frequency, high-tunability, and immunity to electromagnetic interference. In recent years, there is a growing interest in using MWP technologies for developing RF filters with tunable and reconfigurable passbands [16], [84]–[89]. Single passband MWP filters can be implemented using various techniques, including chip-based stimulated Brillouin scattering [90], [91], optical comb based filters [92]–[94]. However, only a few of the approaches [57], [84], [95], [96] can be transformed into a multiband filter design – but only the center frequency or the number of passbands can be tuned [97]. Among all the existing tunable multiband RF filter approaches, optical comb based filters with interleaved optical combs can provide the largest number of passbands as well as the highest tunability and reconfigurability. Although a large number of reconfigurable RF passbands can be generated, each passband in the multiband filter has a close relationship with one another – frequency tuning of one passband will lead to a frequency change in another passband, and the appearance of one passband often requires the presence of another passband. This limitation is caused by the fact that each interleaved optical comb is related to each other through the use of the same interferometric device. Furthermore, the spectral shape and bandwidth of all the passbands are determined by one optical filter to shape the optical comb, resulting in the same spectral shape and bandwidth across all the passbands [98], [99]. Therefore, none of the existing approaches can achieve fully independent control of frequency, bandwidth, amplitude, group delay slope, or spectral shape of each of the passbands.

In this chapter, we present a programmable design algorithm and experimental demonstration of a microwave photonic multiband RF filter with independent tunable passband spectral properties. Then, based on a novel decomposition and reconstrunction algorithms, we successfully achieved an adaptive RF spectral shaper with 11 controlling points to flexibly process arbitrary wideband RF spectrum, enabling S,C,X bands adaptive shaping.

4.1 Programmable Multiband RF filters Based on Photonics

Multiband RF filters with independently controllable passbands are an essential component in dynamic multiband RF communications. Unfortunately, even a fixed multiband RF filter without the capability to adjust the passband properties individually is very difficult to achieve using either RF electronics or microwave photonic technologies. In microwave photonic approaches, the critical limitation is the close relationship between passbands – the tuning of one passband will lead to a change in another, hindering the ability to independently control each passband. In this section, a programmable microwave photonic multiband filter with full control of amplitude, frequency, bandwidth, group delay slope, and spectral shape of each passband has been experimentally demonstrated. A multiband filter design algorithm has also been developed, which considers each RF passband as an individual, then uses inverse Fourier transform and filter design rule to determine the corresponding optical parameters, and combines a series of shaped cosine functions to achieve the desired RF properties.

The progammable waveshaper is based on Finisar's Liquid Crystal on Silicon (LCoS) technology. As shown schematically in the Fig. 4.1, the input signal is dispersed by a conventional grating before its spectral components hit the LCoS optical processor. This LCoS processor consists of a matrix of reflective

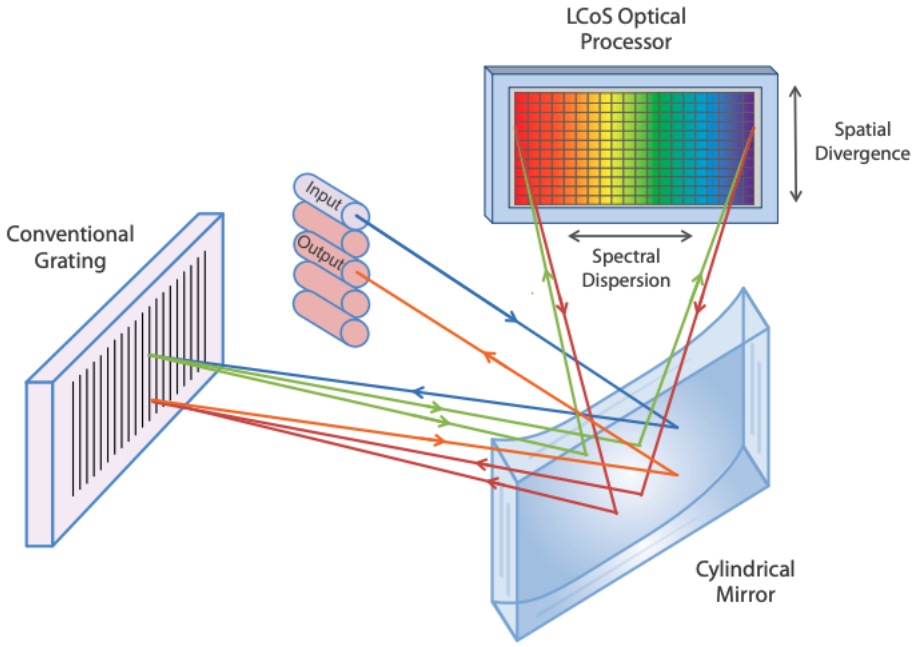

Figure 4.1: Working principle of the Finisar 1000S wave shaper [100].

liquid crystal elements. By applying voltages to these matrix elements, they can add individual phase shifts to the reflected signals which allows beam steering of the signal components hitting the LCoS processor. As the wavelengths are separated on the LCoS chip the control of each wavelength is independent of all others and can be switched or filtered without interfering with other wavelengths. As a result, the structure offers spectral attenuation, dispersion and optical switching capabilities which are available in the wave shaper [101].

Although the waveshaper provides the capability to flexibly manipulate optical spectrum, the dynamic processing of wideband RF signals is not investigated yet. To fully control the wideband RF signal, a close relationship between optical spectrum and RF response with particular physical settings needs to be investigated. Therefore, an automated GUI for user-friendly useage targeting the dynamic RF signal processing is highly desired. The designed GUI for fully automated multiband RF filters design based on MATLAB

is shown in Fig. 4.2, which can automatically generate the corresponding `example-filter.wsp` formatting file for optical wave shaper, including both hardware description and the embedding algorithm to fulfill the desired multiband RF response. It is important to mention that this GUI design is the key to achieve the research goals for this section. And the detailed codes are also attached in Appendix. B.

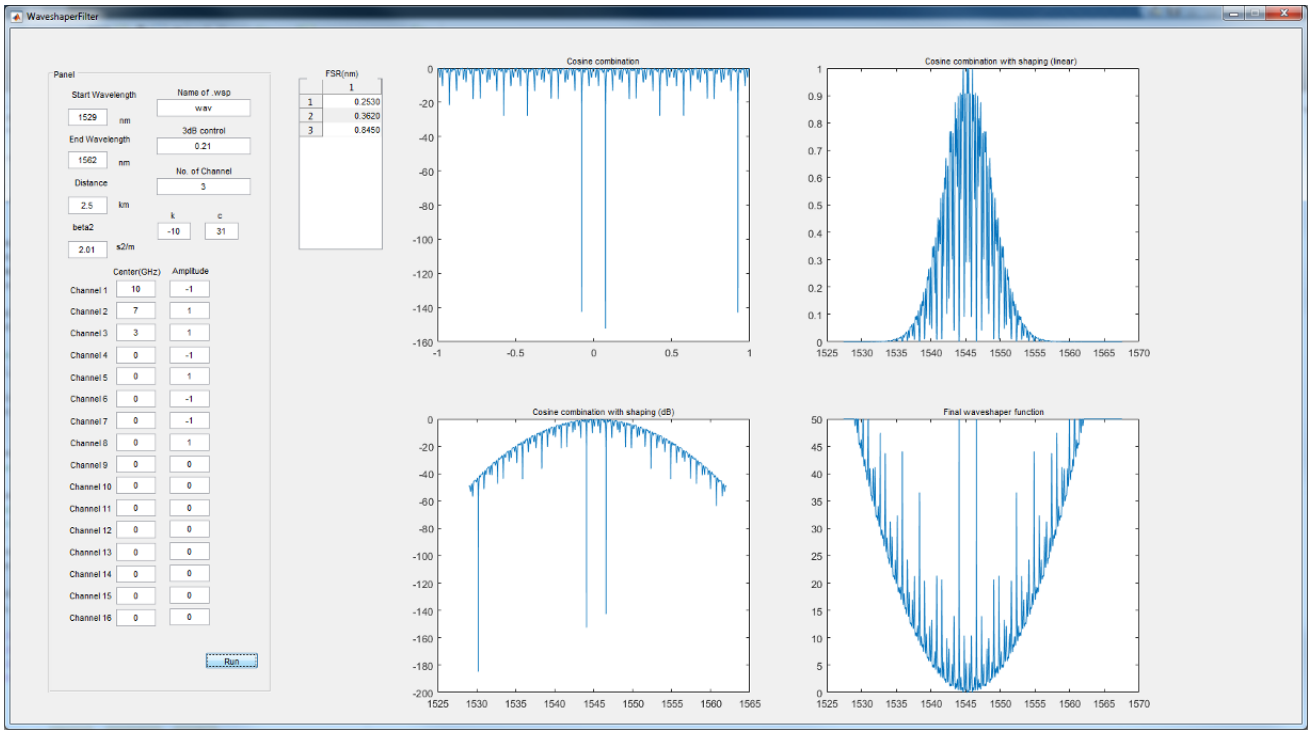

Figure 4.2: Illustration of the designed multiband filter GUI.

4.2 Microwave Photonic Multiband Filter with Independently Tunable Passband Spectral Properties

[1] In this section, we present the design algorithm and experimental demonstration of a microwave photonic multiband RF filter with independent tunable passband spectral properties. As illustrated in Fig. 4.3, the proposed algorithm considers each RF passband as an individual, then it uses the inverse Fourier transform relationship between the RF passband and the corresponding optical profile, as well as the finite impulse response (FIR) filter design rule to determine the corresponding optical parameters, including free spectral range (FSR), bandwidth, envelop profile, and weight (i.e. amplitude of the comb) of each shaped cosine optical comb for each passband. As a final step, a series of properly shaped cosine functions are combined into one final equation and is programmed into an optical spectral shaper to achieve the desired RF properties in the microwave photonic based multiband RF filter. We have experimentally demonstrated amplitude, frequency, bandwidth, and group delay slope tuning. Independent spectral shape reconfiguring between Gaussian, flat-top, and triangular shapes has also been achieved.

4.2.1 Operation principle

The proposed independently tunable multiband filter has a similar structure as a conventional optical comb based microwave photonic filter [102], which consists of a broadband light source, an optical spectral slicing device for generating the filter taps (i.e. optical carriers), an electro-optic modulator for modulating the RF input signal onto the optical carriers, a dispersive medium to provide temporal delay between

[1] **Q. Liu**, J. Ge, M. P. Fok. "Microwave photonic multiband filter with independently tunable passband spectral properties." Optics Letters, 43 (2018): 5685 - 5688.

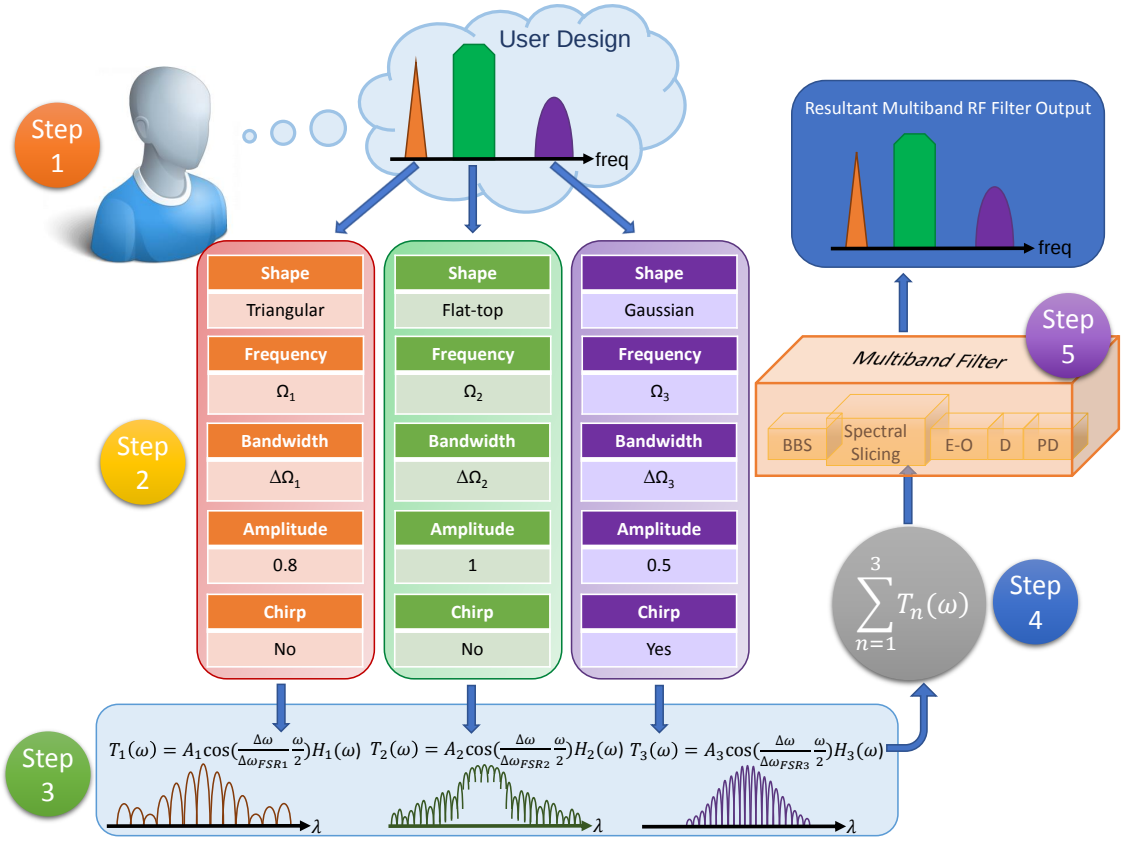

Figure 4.3: Illustration of the proposed multiband filter design algorithm. Step 1: Determine the desired frequency response of the multiband filter by user. Step 2: Design the properties of each passband individually. Step 3: Generate the corresponding shaped cosine function for each passband. Step 4: Combine all the shaped cosine function into one single final shaping function. Step 5: Control the spectral slicing device in the multiband filter using the final shaping function. BBS: broadband source; E-O: electro-optical modulator; D: dispersive medium; PD: photodetector.

taps, and a high speed photodetector to convert the weighted and delayed optical signal into the desired RF response. The user will first determine the desired frequency response of the multiband filter (Step 1) and then design the parameters for each passband, including the spectral shape, bandwidth, center frequency, filter amplitude, and group delay slope if needed (Step 2). According to the desired RF filter center frequency $\Delta\Omega_n$, the corresponding FSR $\Delta\Omega_n$ and the resultant 3-dB bandwidth $\Delta\Omega_n$ of the nth passband can be respectively expressed as

$$\Delta\omega_{FSRn} = \frac{2\pi}{\beta_2 L_{DCF}\Omega_n}, \Delta\Omega_n = \frac{\sqrt{8ln2}}{\beta_2 L_{DCF}\omega_n} \tag{4.1}$$

where β_2, L_{DCF}, $\Delta\omega_n$, $\Delta\omega$ denote group velocity dispersion (GVD), length of the dispersive medium, 3-dB bandwidth, and full bandwidth of the shaped optical spectrum, respectively. Once the above parameters for each passband are defined by the user, a cosine function shaped by $H_n(\omega)$ is used to represent the properties of each optical comb corresponding to the desired properties of the RF passband. The cosine function for each of the passband is designed based on the inverse Fourier transfer relationship and microwave photonic filter design rules (Step 3). Amplitude of each passband can be tuned using the parameter An, which controls the power of the shaped optical comb. The final optical comb is generated by combining all the shaped cosine functions that corresponds to the 1st to nth passband (Step 4). The final step is to program the spectral slicing device using the final combined cosine function (Step 5). The final shaped cosine function for controlling the optical spectral slicing device is

$$T(\omega) = \sum_{n=1}^{N} A_n cos(\frac{\Delta\omega}{\Delta\omega_{FRSn}} \cdot \frac{\omega}{2}) H_n(\omega) \tag{4.2}$$

4.2.2 Experimental details

In our experiment, a superluminescent diode (Thorlabs SLD S5FC1005S) is used as the broadband light source that covers the wavelength range from 1528-1568 nm, while a dispersive fiber with total dispersion of 397.35 ps/nm is used as the dispersive medium. A 12 GHz electro-optic modulator (Fujitsu FTM7921ER) is used to modulate the RF signal onto the optical comb, while a 20 GHz photodetector is used to convert the optical signal back to RF domain and a RF network analyzer (Agilent E5071C) is used to observe the desired RF response. Bandwidths of the modulator and the photodetector set the upper frequency limit for our multiband RF filter. An optical waveshaper (Finisar 1000S) is used for spectral slicing and profile shaping of the optical comb for programmable control of the optical spectra according to the final shaped cosine function (Eq. 4.2). To enable system integration, an integrated line-by-line optical pulse shaper [103] or on-chip 2D meshes of connected waveguides [104] can be used instead.

Figure 4.4 is a preliminary experiment to study the design of the proposed tunable multiband RF filter. A series of single bandpass filters spaced at 1 GHz are obtained over a 10 GHz frequency range. Fig. 4.4(a)(i)-(iii) shows shaped optical spectra of three Gaussian RF single passband filters with center frequency at 2 GHz, 6 GHz, and 8 GHz, indicated as #1, #2, and #3 in Fig. 4.4(b). The RF spectra corresponding to all the ten single passband filters are shown in Fig. 4.4(b). Clear spectral profiles, uniform amplitude, and sidelobe suppression ratio of over 40 dB are achieved for all single passband filters. Next, three shaped cosine functions are picked to generate a multiband filter with three passbands at 2 GHz, 6 GHz, and 8 GHz. Thus, the three corresponding shaped cosine functions with FSR of 1.2 nm, 0.4 nm, and 0.3 nm are selected and combined, resulting in the final shaped cosine function for controlling the spectral slicing device. As a result, a shaped optical spectrum with the desired interleaving optical combs

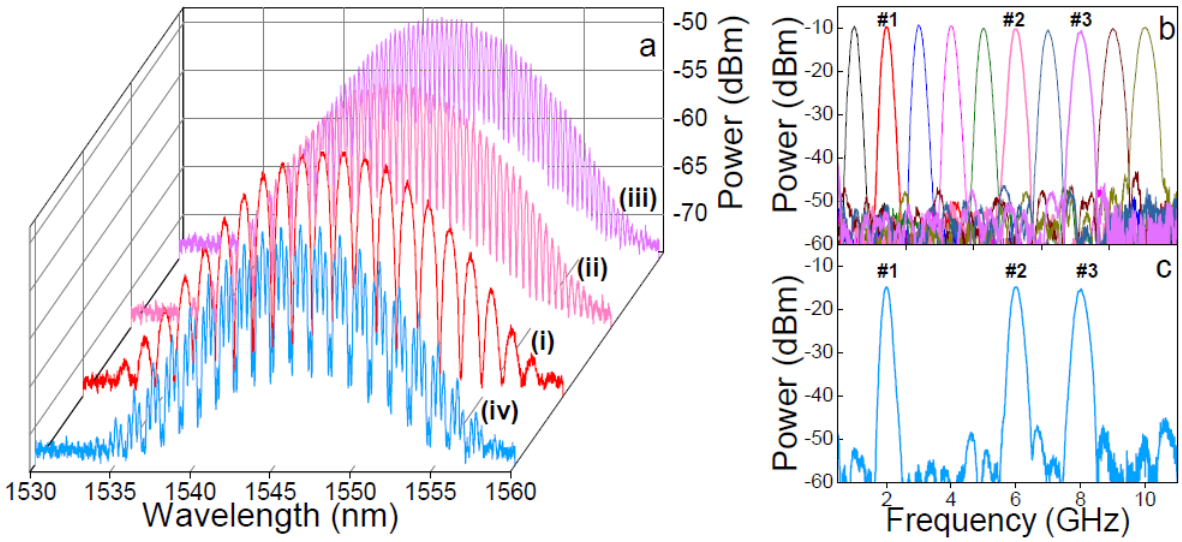

Figure 4.4: Experimental demonstration of the proposed multiband filter design algorithm. (a) Shaped cosine-sliced optical spectra: (i)-(iii) corresponding to passband # 1 (2 GHz), #2 (6 GHz) and #3 (8 GHz); (iv) Optical spectrum of the final shaped cosine function for a three-passband filter. (b) Measured RF spectra of ten single-bandpass filters. (c) RF spectrum of the three-passband filter resulted from the filter design algorithm with passbands centered at 2 GHz, 6 GHz and 8 GHz.

is generated as shown in Fig. 4.4(a)(iv), and is used as the optical carrier for modulation by the input RF signal. The modulated optical carrier is then propagated through the dispersive medium and detected by a photodetector, the resultant RF response is measured by a RF network analyzer that shows the designed three-passband multiband filter with passbands at 2 GHz, 6 GHz, and 8 GHz, as shown in Fig. 4.4(c). The preliminary results prove the feasibility of using the proposed design algorithm for designing multiband RF filters with high flexibility and customizability.

4.2.3 Results and discussions

Various combinations of three different filter shapes, including Gaussian, triangular, and flat-top profiles, in a three-passband multiband filter are also demonstrated, as shown in Fig. 4.5. To achieve mixed spectral

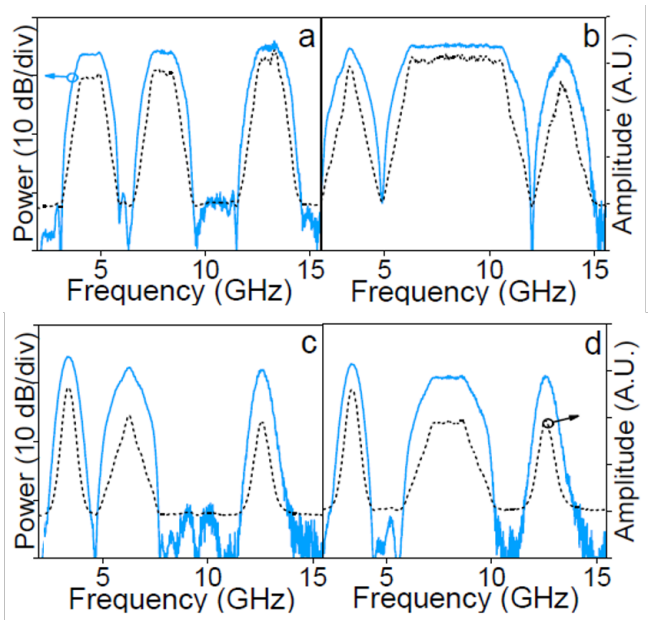

Figure 4.5: Experimental results of multiband filter with mixed and individually tunable spectral shapes. (a) Three flat-top passbands filter. (b) Triangular-flattop-triangular filter. (c) Gaussian-triangular-Gaussian filter. (d) Gaussian-flattop-Gaussian filter.

shape in a multiband filter, the desired profile – mainly filter shape and bandwidth – for each passband is first designed; subsequently, the algorithm takes the inverse Fourier transform of each desired filter shape and uses it to shape the corresponding cosine function. For example, a 10-nm optical spectral range of optical comb is shaped into a sinc-squared function in order to achieve a triangular-shaped passband; Flat-top passband shape is achieved using two sinc-squared functions for shaping. Blue solid lines in Fig. 4.5 are the resultant RF responses of the proposed multiband RF filter in logarithmic scale, while the black dashed lines correspond to the RF response in linear scale. The results clearly demonstrate the ability to individually control the spectral shape and bandwidth of each passband.

We also experimentally demonstrate the capability of individual amplitude control in an 11-passband Gaussian filter and a 5-passband triangular filter, as shown in Fig. 4.6(a)-(d) and Fig. 4.6(e)-(h), respectively.

Amplitude of each passband is set to the desired value that is independent of each other. It is worth noticing that this individual passband amplitude control is effective in compensating the dispersion induced power fading phenomenon occurred in any comb based RF filters that use phase modulator for modulating the RF signal onto the optical carrier.

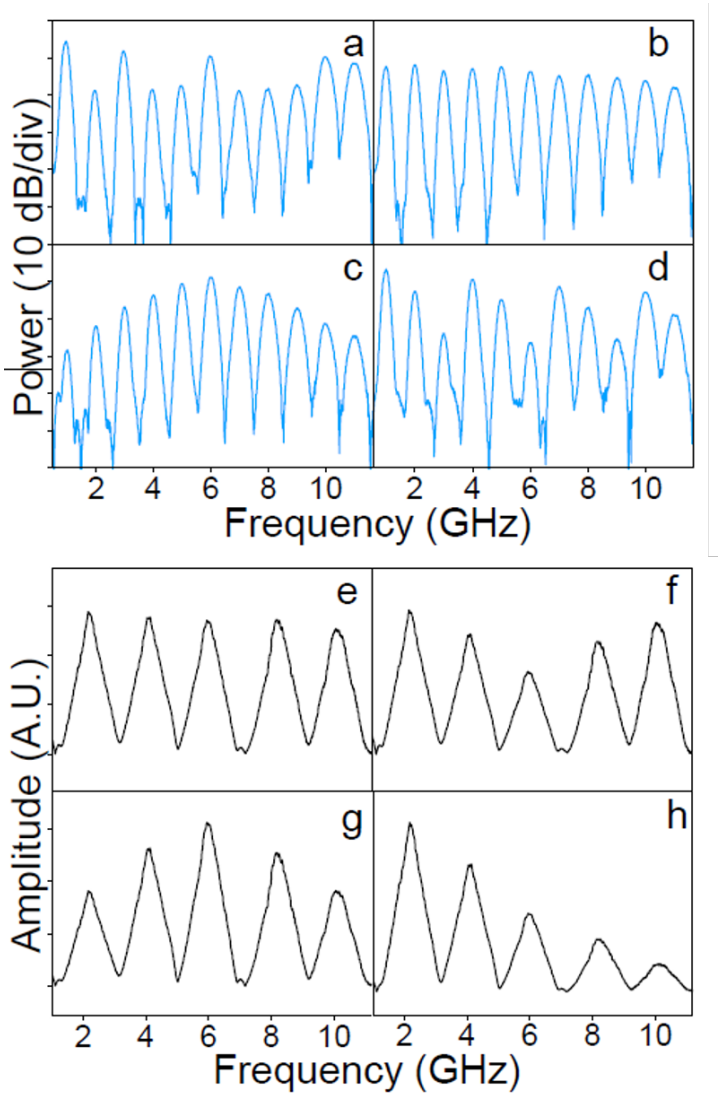

Figure 4.6: Experimental results of individual passband amplitude tuning in multiband filters. (a)-(d) Eleven-passband Gaussian filter with different amplitude assignment: (a) random; (b) flat; (c) triangular distribution; (d) saw-tooth distribution. (e)-(h) Five-passband triangular filters with different amplitude assignment: (e) flat; (f) inverted triangular distribution; (g) triangular distribution; (h) negative slope distribution.

To individually change the 3-dB bandwidth of each passband, we can tailor the 3-dB bandwidth of each of the cosine function $\Delta\omega_n$, according to Eq. 4.1. Since the dispersive medium has a slightly different dispersion values at different wavelengths, the filter passband bandwidth also depending on the particular spectral range that the optical comb is located. For example, the black and purple curves in Fig. 4.7(a) indicate two optical combs with the same 3-dB bandwidth but are at two different spectral ranges. The difference in spectral range will result in a different 3-dB bandwidth in the RF passband. Fig. 4.7(b)-(c) show the experimental results of a 4-passband multiband filter with individually tunable passband bandwidth by controlling the 3-dB bandwidth of each cosine function $\Delta\omega_n$. The number of passband is determined by the passband bandwidth, the frequency range of interest, and resolution of the waveshaper; while the passband bandwidth is determined by the width of the optical spectrum. In our current setup, the minimum and maximum 3-dB bandwidth are 180 MHz and 680 MHz, respectively; resulting in a 278% of bandwidth tuning. With the ability to individually tune the passband bandwidth, we can compensate the bandwidth broadening effect due to the 3rd order nonlinear dispersion slope of the dispersive medium, and result in a multiband filter with the same bandwidth over all the passbands.

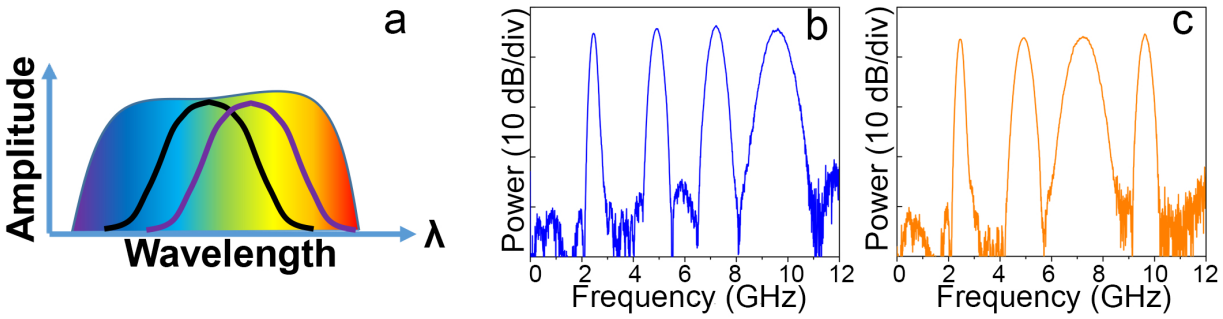

Figure 4.7: Experimental results of individual passband bandwidth tuning. (a) Optical spectra at different wavelength range give different RF passband bandwidth. (b)(c) Four-passband Gaussian multiband filter with individually tunable passband bandwidth.

The chirp function of a photonic-based single passband RF filter can be written as [50],

$$F_{chirp}(\omega) = cos(\frac{k}{4\pi}\omega^2 + \frac{b}{2}\omega) \tag{4.3}$$

where k is used to determine the sign of the group delay slope and the rate of FSR change, while b determines the number of comb lines within the selected optical bandwidth. Through different choices of k and b, the chirp rate of the resultant optical comb as well as the group delay slope of each of the passband in the multiband filter can be individually controlled. In a chirped filter, since the density of the optical comb linearly changes across the optical spectrum, center frequency of the passband is determined by the FSR at the center part of the sliced optical spectrum. The resultant chirped optical comb with a small positive k is shown in Fig. 4.8(a), while a comb with larger positive k is shown in Fig. 4.8(b). A positive k results in a denser comb at the longer wavelength and a sparser comb at the shorter wavelength; while a linear chirped optical combs with negative k is shown in Fig. 4.8(c), resulting in a denser comb at the shorter wavelength. Since the tuning of k will also change the bandwidth of the resultant RF passband, both the optical spectrum range $\Delta\omega$ and the 3-dB bandwidth of the shaped optical spectrum $\Delta\omega$ will have to be adjusted accordingly to maintain the same RF bandwidth. Fig. 4.8(d) shows the RF spectra of a single passband filter with tunable group delay slope (inset). The spectral profiles are well maintained during group delay slope tuning. Both positive (blue curve) and negative (red, orange, and black) group delay slopes are achieved by setting different k. Also, chirped multiband filter with different bandwidths and group delay slopes among the five passbands are shown in Fig. 4.8(e) and 4.8(f), which prove the capability to individually control the group delay slope of each passband in a multiband RF filter.

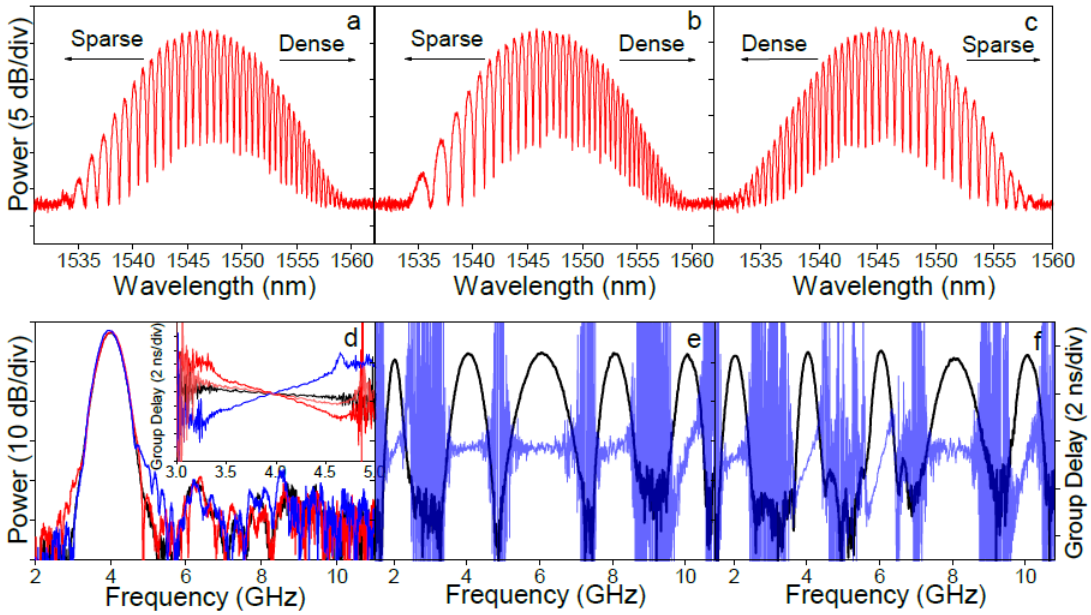

Figure 4.8: Experimental results of group delay slope tuning. (a)(b) Chirped optical spectra with different positive k values. (c) with negative k value. (d) Single passband chirped filter with different group delay slopes; inset: group delay measurement. (e)(f) Five-passband Gaussian chirped filter with individual group delay slope and bandwidth control.

4.3 Microwave Photonic Spectral Shaper

Emerging radio frequency (RF) wireless communication utilizes dynamic usage of spectrum to fulfill the needs in heterogeneous and multiband communication applications [76], [105]. Due to the ever-increasing operation bandwidth of modern RF systems, the ubiquitousness of high capacity and always-on mobile devices as well as the data-intensive day-to-day applications, there is a critical need of adaptive RF spectral shaping systems, such that new applications can be supported and quality of services can be guaranteed in dynamic multi-function RF applications [106]–[108]. For decades, tunable and reconfigurable band-pass and notch filters are the major devices for spectral processing and noise removal. Nevertheless, it is challenging to dynamically process and manipulate a wide RF spectrum that spans across tens of GHz

bandwidth using either RF electronics or digital signal processing. The challenge is due to the limited wideband functionality of RF electronics as well as the large amount of sampling and computation power needed in digital signal processing. Although electronic-based RF spectral shaping provides on-chip solutions [81], the tight design criteria and inherent inflexibility in electronics limit the operation bandwidth, the variety of the spectral shaping function, as well as tunability and reconfigurability of the spectral functions that could be achieved [109], [110].

Microwave photonics has been a good candidate to tackle various challenges of its electronic counterpart due to its merits of large operation bandwidth, high tunability, and high reconfigurability [16], [17]. Extensive efforts have been made to spectrally processing RF signal using photonics in various ways, including spectral shaping [90], [95] , single and multiband spectral filtering [97], spectral channelizing [111], [112], and spectrum analyzing [113]. A lot of successes have been achieved in the field of microwave photonic filtering [84], [114] over the last decade, that provides single passband or multiband filtering with mainly Gaussian profile. Passband filtering can be regarded as one type of spectral shaping and is deemed to be the nature way for implementing RF spectral shaping. However, it is challenging to achieve RF spectral shaping with good spectral resolution, multiple independent spectral control points, complex shaping functions, and high reconfigurability over tens of GHz frequency range. For example, single passband/notch filter cannot be used to control complex RF function spanning across tens of GHz RF spectrum. Recent research focus on shrinking the bandwidth of passband/notch to increase the resolution of a RF control point [115], [116]; however, the fine RF control point cannot be scaled up for processing RF spectrum that span across tens of GHz range. Cascaded configuration could potentially provide multiple control points [117] but the resultant system could be expensive and have high power consumption.

Several potential candidates for wideband RF spectral shaping have been proposed including multi-pump Brillouin based microwave photonic filter [95], FIR based multiband microwave photonic spectral filter [118], and Kerr comb based RF bandwidth scaling [119]. However, each technique faces critical challenges on implementing RF spectral shaper with complex and adaptive functions. For example, Brillouin technique provides a resolution as high as 32 MHz but lacking spectral profile reconfigurability due to the difficulties in independent gain profile control with multiple Brillouin pumps [95]. Direct FIR based spectral shaping approaches have one major limitation is that complex and precise phase manipulation of the optical spectrum is necessary to satisfy the Fourier transform relationship between the optical and RF domains. Unfortunately, it is very challenging to achieve rapid phase control beyond $-\pi$ to π of each comb lines in the optical comb carrier with existing technologies that resulting in distorted RF spectral response. Therefore, only simple RF spectral shaping function including Gaussian, triangular, and flattop have been obtained. On the other hand, FIR microwave photonic multiband filter offers wideband RF spectral shaping capability, but most existing approaches shows a tight spectral relation between each passband, limiting its independent control capability. To fulfill the requirements in dynamic and wideband RF communication systems, there is a critical need for multi-point dynamic spectral control over a wide bandwidth with varying resolution.

4.4 Adaptive Point-by-point RF Spectral Shaper

[2] Radio frequency spectral shaper is an essential component in emerging multi-service mobile communications, multiband satellite and radar systems as well as future 5G/6G radio frequency systems, for equalizing spectral unevenness, removing out-of-band noise and interference, as well as manipulating

[2] **Q. Liu**, M. P. Fok. "Adaptive photonic RF spectral shaper." Optics Express 28.17 (2020): 24789-24798.

multi-band signal simultaneously. While it is easy to achieve simple spectral functions using either conventional microwave photonic filters or optical spectrum to microwave spectra mapping techniques, it is extremely challenging to enable complex spectral shaping functions over tens of GHz bandwidth as well as achieving point-by-point shaping capability to fulfill the needs in dynamic wireless communications. In this section, we proposed and demonstrated a novel spectral shaping system, which utilizes a two-section algorithm to automatically decompose the target RF response into a series of Gaussian functions and reconstruct the desired RF response by microwave photonic techniques. The devised spectral shaping system is capable of manipulating the spectral function in various bands (S, C, and X) simultaneously with step resolution of as fine as tens of MHz. The resolution limitation in optical spectral processing is mitigated using discrete convolution technique. Over ten dynamic and independently adjustable spectral control points is experimentally achieved based on the proposed spectral shaper.

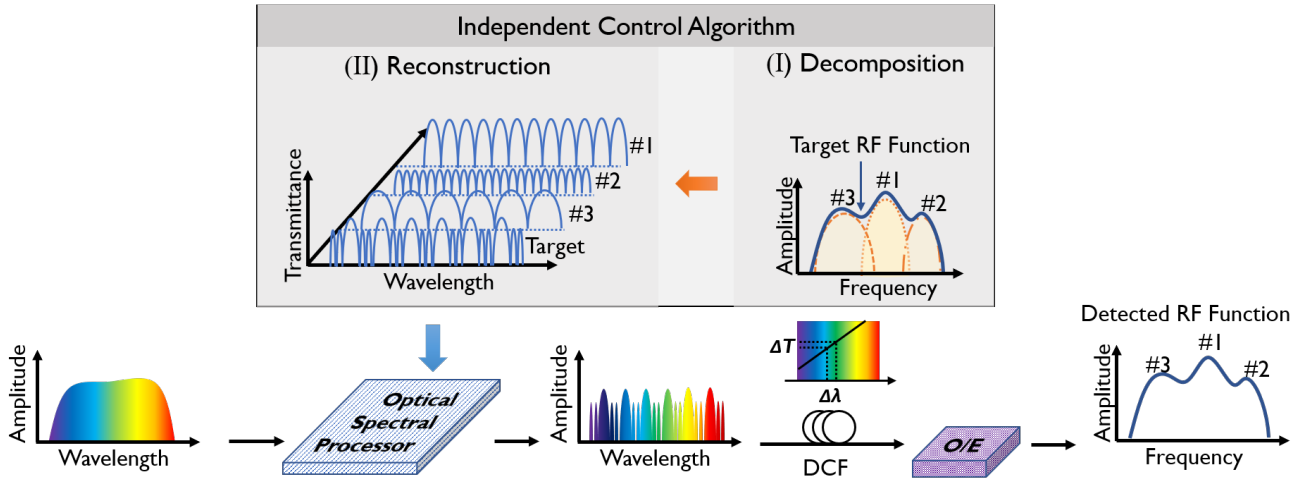

Figure 4.9: Adaptive photonic RF spectral shaper with automatic control algorithm.

In this section, a novel adaptive microwave photonic RF spectral shaper with multiple adaptive spectral control points over wideband operation frequency range of 10 GHz is proposed and experimentally demon-

strated. The proposed scheme can process the whole frequency band simultaneously with arbitrary/user-defined RF response instead of using single/multiband filter with fixed spectral shape (e.g. triangular, Gaussian, flat-top, etc.). To overcome the phase limitation in direct FIR scheme, this proposed approach automatically breaks down the target spectral response into a unique series of Gaussian functions according to its spectral characteristic, such that manipulation of optical phase is not required. Then the corresponding sets of finite impulse responses (FIR) parameters are simultaneously generated. The FIR parameters are combined and is then used to control the generation of interleaving optical comb carrier with the correct weight and delay, as illustrated in Fig. 4.9. In this way, the target spectral response can be reconstructed from the shaped optical comb carrier after photodetection. Unlike optical to RF spectral mapping approach where the RF resolution is fixed and directly limited by the optical spectral resolution, our scheme is based on the use of multiple FIR to generate the interleaved optical comb carriers with all the needed free spectral range (FSR) for the reconstruction of the target RF spectral function, which significantly improved the step resolution to less than 10 MHz. Therefore, the proposed scheme enables adaptive RF spectral shaping with flexible spectral profile through the automatic spectral decomposition and reconstruction processes.

4.4.1 Experimental details

Figure 4.10 shows the experimental setup of the proposed RF spectral shaper. A superluminescent diode (Thorlabs SLD S5FC1005S) is used as a broadband optical source, which covers the wavelength range from 1528 nm to 1568 nm. An optical wave shaper (Finisar 1000S) is used for controlling the optical spectral properties of the broadband optical source through spectral slicing, such that interleaved combs with the designed amplitude, bandwidth, spacing, and envelope profile can be generated all at once based on

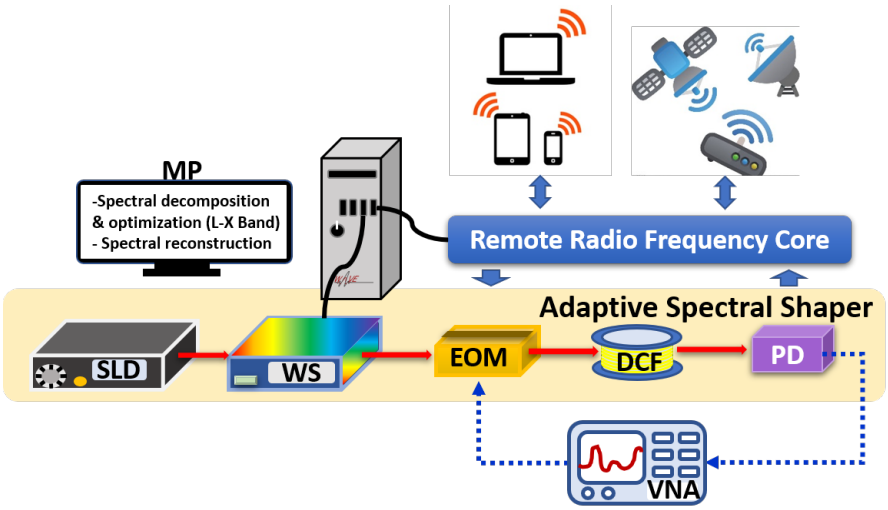

Figure 4.10: Experimental setup of the multi-point adaptive RF spectral shaper. SLD: superluminescent diode; WS: optical wave shaper; EOM: electro-optic modulator; DCF: dispersion compensating fiber; PD: photodetector; VNA: vector network analyzer. MP: microprocessor (Red line: optical paths; dashed blue line: electrical paths; black line: computer control paths).

the results from the RF spectral decomposition algorithm. Since optical comb generation and comb profile shaping are performed at the same time at the optical waves shaper, no complex spectral alignment or calibration is needed [98], [99]. A 12-GHz electro-optic modulator (Fujitsu FTM7921ER) is used to modulate the RF signal from the remote RF core onto the shaped comb carrier. In our experiment, a sweeping RF signal from a 20-GHz vector network analyzer (Agilent E5071C) is used as the RF input for characterizing the proposed RF spectral shaper. The FIR tap delay is provided by the dispersion compensating fiber (DCF) with length of 2.5 km and group velocity dispersion of 170 ps/nm/km. An 18-GHz photodetector is used to convert the modulated optical comb carrier back to RF domain and the resultant RF response is measured by the VNA. The enabler of the adaptive and independent multi-point control of the RF spectral response is the two-section algorithm for optimized decomposition and reconstruction of the target RF response.

4.4.2 RF Spectral Decomposition and Optimization

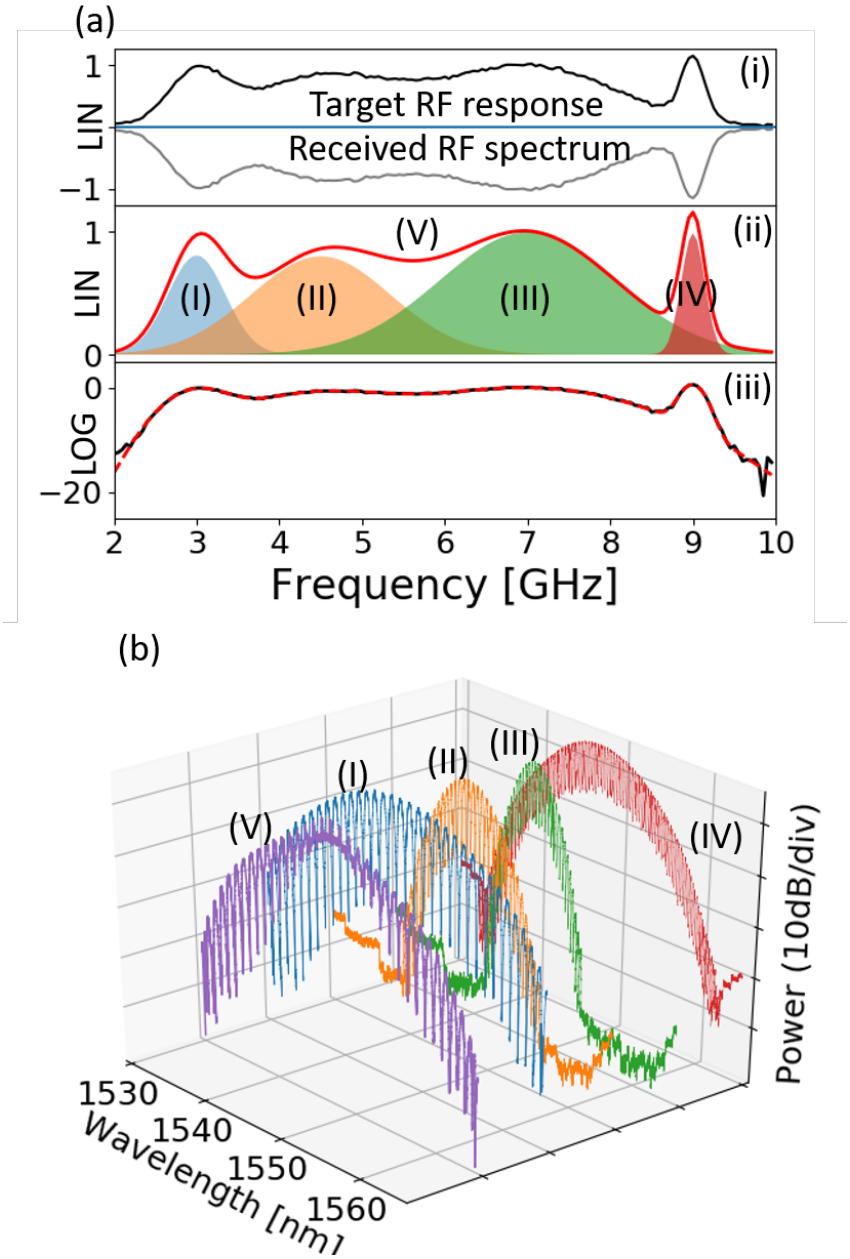

Figure 4.11: Illustration of the automatic RF spectral decomposition and reconstruction process. (a)(i) received RF spectrum/response (grey); target RF response (black); equalized response (blue); (ii) optimized and decomposed spectra of Gaussian functions; (iii) reconstructed RF spectra (red) and target RF response (black) in log scale. (b) Corresponding optical spectral control with independent comb properties (I-IV: blue, orange, green and red) and corresponding aggregated optical spectrum (V: purple).

Based on radial basis decomposition [120], [121], wideband RF spectrum can be represented by orthogonal basis in the form of a series of Gaussian functions with different bandwidth and amplitude; similar to how a repetitive time domain waveform can be decomposed into a series of sinusoid basis at different frequency. Therefore, given a target RF spectral response (e.g. complementary RF response for equalization in Fig. 4.11(a)i), the target response can be decomposed into a series of Gaussian functions, as shown in Fig. 4.11(a)ii. The decomposition process is achieved by having Gaussian peaks aligning at the maxima of the RF response, while the overlapping of the tails of Gaussian functions forms the minima or plateaus. Therefore, a widely spaced subset of Gaussian functions with wide bandwidth will lead to a gentle change in the resultant RF spectral response with coarse spectral control. While fine control of sharp amplitude changes in the RF response can be achieved by offset-overlapping a narrow bandwidth Gaussian function with a main wideband Gaussian function. Furthermore, overlapping regions between each Gaussian function could constitute a valley or plateau in the RF response. Therefore, the Gaussian functions could be spaced unevenly, and the number of Gaussian functions corresponds to the number of control points needed in the RF spectrum reconstruction. The goal of the algorithm (Algorithm 1) is to identify and optimize the Gaussian functions with different amplitude and bandwidth properties needed in the target RF spectral response, including the total number of Gaussian functions n for RF spectral reconstruction and the detail parameters of the ith Gaussian function, such as amplitude C_i, center frequency f_{c-i}, and 3-dB bandwidth f_{3dB-i}.

Mathematical expression of the decomposed RF response can be expressed as series of Gaussian functions as described below,

$$F_R(f) = \sum_{i=1}^{n} C_i \exp -\frac{(f - f_{c-i})^2}{2 f_{3dB-i}} \tag{4.4}$$

Table 4.1: RF Spectral Decomposition and Optimization

1: input: data of RF response curve (fk, pk): k = 1, …, N
2: Determine and label m maxima and minima of the data
3: Estimate the parameters of the m Gaussian basis
4: Initialize n = 1
5: **if** n > m then stop
else use the parameters of n most dominant Gaussians determined in step 3 as the initial values for the Marquardt algorithm and refine the parameters.
6: **If** the resultant error $e_n < \epsilon$ then stop
else increasing n by one and go to step 5.
7: output: the number of n and the corresponding parameters
$(C_i, f_{c-i}, f_{3dB-i} : i = 1, \ldots, n)$ of each Gaussian functions

Although the discrepancy between the target RF response and the reconstructed RF response could be reduced using a large number of Gaussian functions, an overly large number of Gaussian functions will consequently degrade the optical comb carrier quality, i.e. the comb features could be masked by another comb, and negatively affect the RF response reconstruction performance. Therefore, the proposed algorithm (Algorithm 1) aims to identify the optimized number (n) of Gaussian functions needed for RF response reconstruction while keeping the discrepancy within the tolerable error limit, ϵ, governed by

$$\sqrt{\frac{1}{N}\sum_{k=1}^{N}(F_R(f_k) - p_k)^2 < \epsilon} \tag{4.5}$$

where N is the total number of frequency points for describing the target RF spectral response, pk is the power magnitude of the kth frequency point, and $F_R(f_k)$ is the fitted power function of the kth power that contributes to maintaining the RF response discrepancy within ϵ. It is worth to notice that the Marquardt algorithm is used to find the local minimum of the cost function, and the initial parameter is estimated by the maximums and minimums of the target RF response to ensure Algorithm 1 is converged.

4.4.3 RF Spectral Reconstruction

Once the RF spectral decomposition algorithm has determined all the feature parameters for the set of Gaussian functions, second part of the algorithm determines the corresponding parameters for generating the optical comb carrier that forms the Gaussian functions for the reconstruction of the target RF response, including comb amplitude A_n, 3-dB optical envelope bandwidth $\Delta\omega_{3dB-n}$, and comb FSR $\Delta\omega_{FSR-n}$ of the n-th group of optical comb. The n-th comb FSR and the 3-dB bandwidth are determined by Eq.4.1.

Since all the optical parameters are combined before using it to control the optical comb generation process, the whole set of optical combs are interleaved and sliced all at once using a single optical spectral shaper. Furthermore, the Gaussian functions in the RF domain $F_R(f)$ and the corresponding envelope of the optical comb carrier $H_n(\omega)$ has a Fourier transform relationship, therefore, the final aggregated optical comb carrier $T(\omega)$ can be expressed as a summation of cosine functions with Gaussian envelope $H_n(\omega)$ as shown in Eq. 4.2.Fig. 4.11(b) shows the measured optical spectra of the four sets of Gaussian-shaped optical comb that corresponds to the four Gaussian RF functions (red, green, blue, and orange curves in Fig. 4.11(a)ii and (b)), as well as the final aggregated optical comb carrier (purple curve in Fig. 4.11(a)ii and (b)) that corresponds to the resultant RF response. The final optical comb carrier keeps all the features of each subset group of optical combs.

According to Eq. 4.1, the minimum bandwidth of each RF control point (i.e. RF feature) is determined by the 3-dB bandwidth of the overall optical comb and the total dispersion provided. While the maximum bandwidth of each RF control point is limited by how narrow the overall optical comb bandwidth could be as well as the photodetector bandwidth. Suppose the dispersion constant β_2 is unchanged,

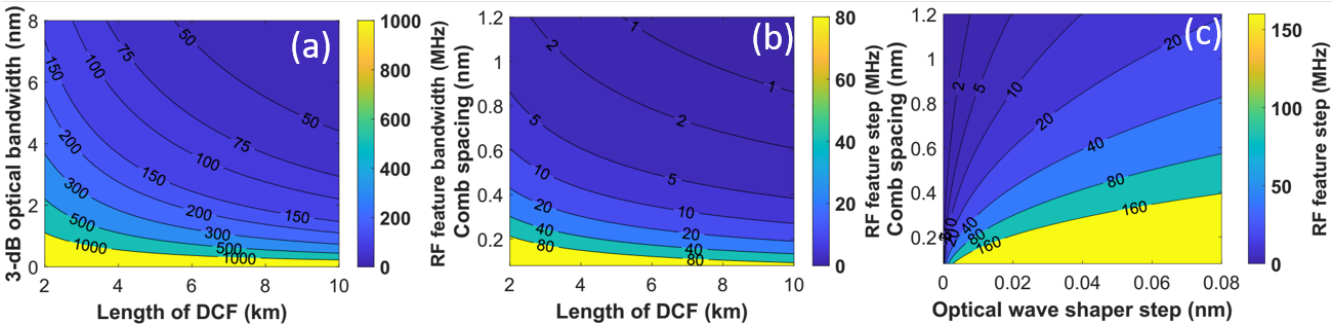

Figure 4.12: Simulation results of (a) Bandwidth of each RF control point (i.e. RF feature) vs 3-dB optical bandwidth and length of DCF, with fixed dispersion constant; (b) Step resolution of each RF control point vs comb spacing and length of DCF, with fixed optical waveshaper step (i.e. addressability); (c) Step resolution of each RF control point vs comb spacing and optical waveshaper step, with fixed dispersion constant.

the resultant bandwidth range of each RF control point can be from several tens of MHz to a few GHz, as depicted in Fig. 4.12 (a).

In addition, the RF step resolution Δf_{step} , i.e. how close two RF control points can be placed, is simulated and is shown in Fig. 4.12(b). It is observed that the larger the optical comb spacing, the finer the RF step resolution would be. The addressability of the optical waveshaper also plays a role in governing the RF step resolution, as shown in Fig. 4.12(c). The optical step resolution in the optical waveshaper governs the precision of the optical comb FSR, which in turn determines the step resolution of the RF response. The mathematical relationship can be expressed as,

$$\Delta f_{step} = \frac{\Delta\omega_{add}}{2\pi\beta_2 L_{DCF}\Delta\omega_{FSR}(\Delta\omega_{FSR} + \Delta\omega_{add})} \tag{4.6}$$

In our experiment, the optical waveshaper used for generating the optical comb carriers has a spectral resolution of 12 GHz, and an addressability of 1 GHz. As illustrated in Fig. 4.13(a), the user can control

the amplitude of each 1-GHz point (red shaded area in the left cycle), while each 1-GHz point has a 12-GHz full bandwidth (purple shaded area). Therefore, to construct a periodic cosine function (red dashed line in Fig. 4.13(a)) using the optical waveshaper, the amplitude at each 1-GHz spacing (alternate red and yellow shaded area) is set to the corresponding value of a sinusoidal function. The resultant optical comb will be of a periodic quasi-sinusoidal function due to the 12-GHz spectral resolution of the optical waveshaper (black solid line in Fig. 4.13(a)). However, the slight difference between periodic desired and quasi-sinusoidal shape will not distort the resultant target RF response because all the essential parameters are still accurately represented in the resultant optical combs.

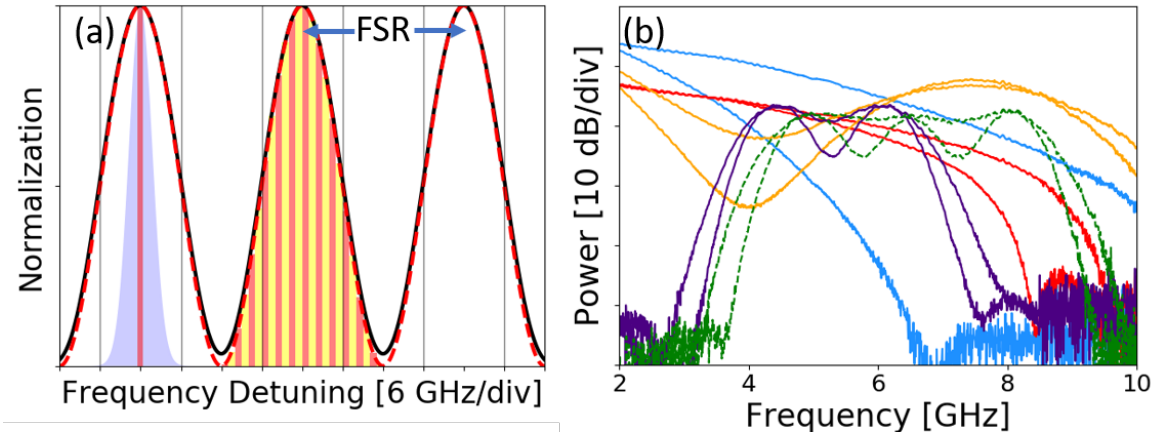

Figure 4.13: (a) Illustration of optical spectral processing for multiple control points at waveshaper; (b) Samples of simple RF responses achieved by the RF spectral shaper that are commonly needed in RF systems.

We did a preliminary experiment to verify the RF spectral shaper's ability to generate different RF spectral shaping/equalization functions across a 10 GHz bandwidth. Showing in Fig. 4.13(b) are examples of several commonly needed RF spectral response in RF systems including negative linear response with variable slopes (red and sky blue), sinusoid (orange), and flat-top/multi-peak bandpass-shaping (green and purple). The generated RF responses show dynamic, precise, and continuous spectral tailoring capability of the proposed RF spectral shaper. It is important to mention that the orthogonal Gaussian basis used in

the proposed algorithm is to provide a general yet dynamic decomposition solution for complex wideband RF response. In our experiment, the narrowest bandwidth obtained by the RF Gaussian function is 180 MHz, while the widest bandwidth is expected to be 55 GHz if the modulator and the photodetector could support.

Next, we demonstrate the feasibility of adaptive spectral control for simultaneous multiband (S, C, and X bands) spectral shaping with non-uniform and fully customizable spectral properties using the proposed two-section algorithm, as shown in Fig. 4.14. First, the target RF response is defined by the user – indicated by the dashed red curve (in linear scale) in Fig. 4.14(a). The target function in log scale is shown by the dashed red curve in Fig. 4.14(b). The function is designed for supporting simultaneous Bluetooth/WiFi transmission (S band) as well as gain equalization at higher frequency range (C+X bands). The proposed algorithm automatically decomposed the target RF response into an optimized number of Gaussian functions (indicated by the five color-shaded areas centered at 2.4 GHz, 3.8 GHz, 5.8 GHz, 7.8 GHz, and 8.5 GHz) for obtaining the desired RF response. Then, the algorithm generates the corresponding optical parameters for the optical comb carriers according to Eq. 4.1 and Eq. 4.2. The parameters are used to control the programmable optical processer, i.e. optical waveshaper, for generating the optical comb carriers needed for the reconstruction of the target RF response. After photodetection, the target RF response is reconstructed as shown by the black curve in Fig. 4.14(a) in linear scale and black curve in Fig. 4.14(b) in log scale. It is observed that the Bluetooth/ WiFi transmission window at 2.4 GHz (region I) has a 40-dB rejection ratio, while gain compensation in Region II and III have 10 dB (purple shaded area) and 6 dB (grey shaded area) dynamic shaping range, respectively. Although there is discrepancy between the target and resultant RF responses, the discrepancy is only less than 1%, which is marked by the green shaded region.

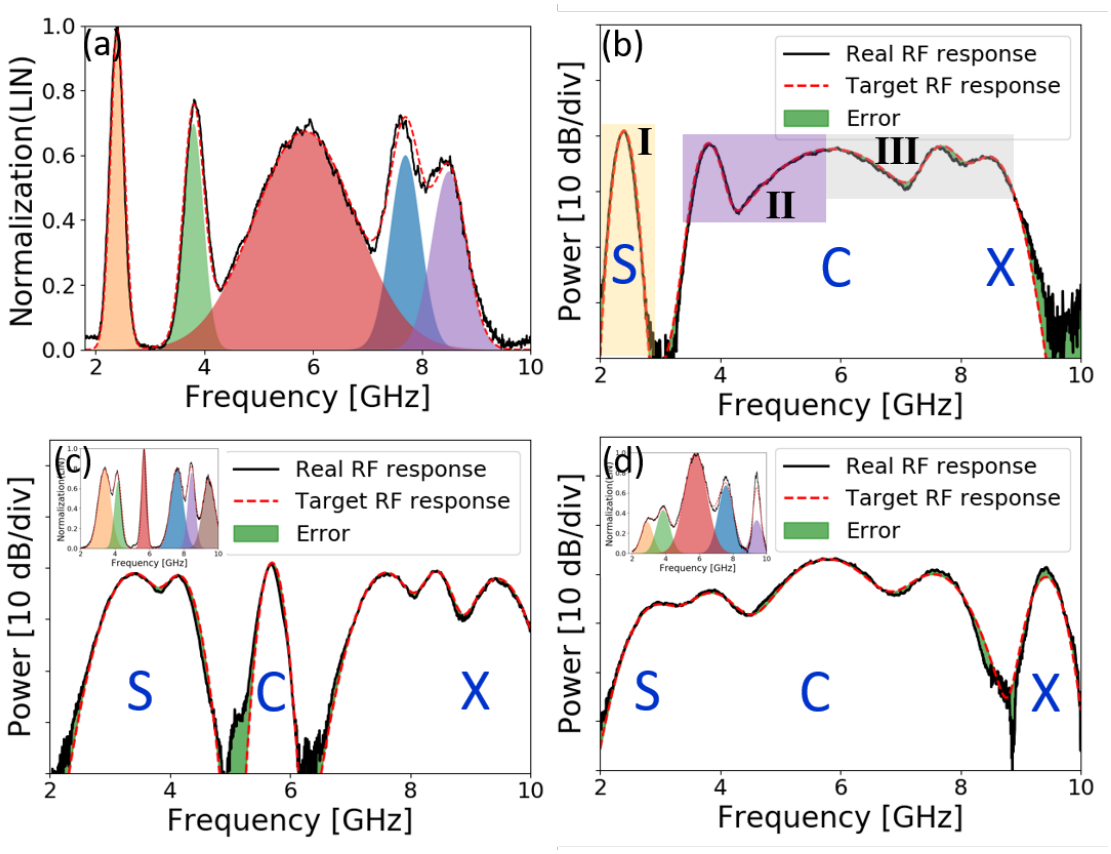

Figure 4.14: Experimental results of wideband adaptive RF spectral shaper with optimized decomposition and reconstruction algorithm. (a) Target RF response (dashed red curve), reconstructed RF response (solid black curve), set of Gaussian functions (shaded); (b) Target RF response for simultaneous Bluetooth/WiFi channel filtering (region I) and spectral compensation (region II and III), mismatch are showed in green shade; (c) S+X band spectral shaping and C band transmission; (d) S+C band spectral shaping and X band transmission.

Furthermore, different target RF response is presented to the RF spectral shaper for verifying its adaptability and reconfigurability. Fig. 4.14(c) has a target RF response that facilitates transmission in C band and dynamic gain compensation in S+X bands, while Fig. 4.14(d) has a target RF response that requires dynamic spectral equalization in S+C bands and signal transmission in X band. The decomposed Gaussian functions are depicted by the color-shaded areas in the linear scale inset. The resultant RF responses generated by the RF spectral shaper are shown by the black solid curve, while the discrepancies are indicated by the green shaded areas in Figure 4.14(c)-(d). The results show that the proposed RF spectral shaper has successfully adapted to changes in the user defined target RF response and generated the corresponding RF response with small discrepancy.

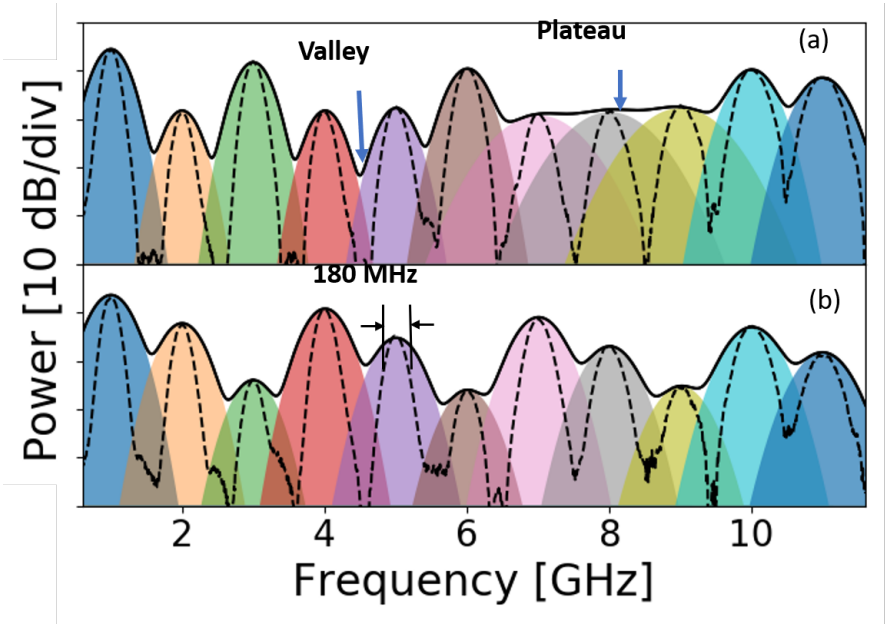

Figure 4.15: (a)-(b) Eleven spectral control points reconstructing a target RF response with peaks, valleys, and plateaus with 180 MHz RF control point bandwidth.

As the number of RF spectral control point increases, some of the optical comb feature could be masked by another comb, resulting in ripples in the resultant RF response. Here, we investigate the maximum number of RF spectral control point (number of Gaussian functions for reconstruction) supported

by the RF spectral shaper without degrading the resultant RF response. First, each Gaussian function are intentionally set to have a narrow 3-dB bandwidth of 180 MHz with shaping slope of 0.03 dB/MHz and are evenly spaced at 1 GHz, as shown by the black dashed lines in Figure 4.15(a)-(b), so that we can clearly observe each of the Gaussian peaks without overlapping. Bandwidth of RF control points are governed by the total dispersion, a 90 MHz bandwidth can be achieved when a 5 km DCF is used. The RF spectral shaper supports 11 spectral control points, and the control points can be placed as close as tens of MHz with uneven spacing if desired, which is governed by the addressability of the optical waveshaper and the dispersion provided. As the bandwidth of the Gaussian functions increases, as shown by the color shaded Gaussian shapes, tails of the Gaussian functions overlap and forms the valleys and plateau of the RF response, as shown by the black solid curves. Figure 4.16(a)-(b) shows the experimental results of the fine tuning of the center position of the RF Gaussian spectral function, which indicates that the 1 GHz addressability in the optical waveshaper results in a step resolution of 7.8 MHz and 18.3 MHz in center frequency at 3 GHz and 6 GHz in both directions, respectively.

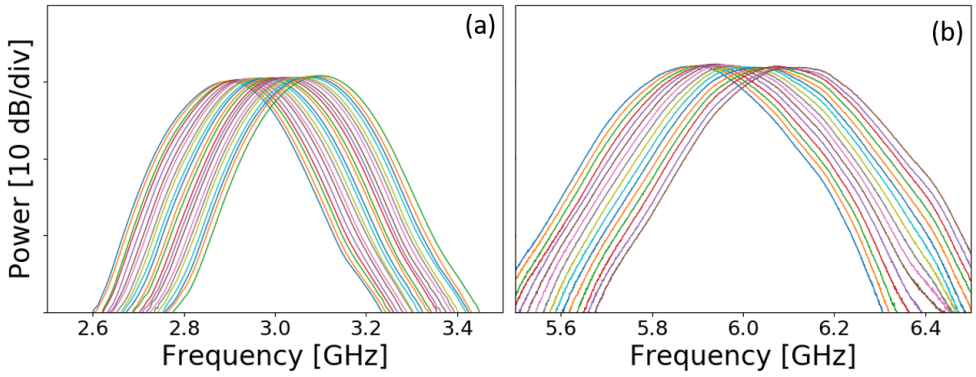

Figure 4.16: (a) Measured 7.8 MHz step resolution when Gaussian RF peak is centered at 3 GHz; (b) Measured 18.3 MHz step resolution when Gaussian RF peak is centered at 6 GHz

4.5 Summary

In summary, we presented a multiband filter design algorithm and experimentally demonstrated a multiband RF filter with fully and individually tuning capability – independent spectral shape reconfiguration for each passband, multiband filters with mixed passband shapes, 278% of bandwidth tuning, and both the amplitude and frequency of each passband can be tuned independently. Specifically, 40 dB of continuous amplitude tuning over 10 GHz of frequency tuning have been achieved. In addition, the group delay slope of each passband can be tuned individually over a range of $\pm$4.5 ns/GHz. The proposed algorithm considers each passband as an individual, such that the corresponding cosine function for the generation of each passband is shaped and weighted precisely and individually before combining them together into the final shaping function.

Based on adaptive decomposition and reconstruction algorithms, a customizable RF spectral shaper with tens of MHz step resolution is also experimentally demonstrated that allows dynamic multi-point control of arbitrary RF spectral function. The proposed spectral shaper is capable of generating arbitrary RF spectral functions for wideband spectral tailoring, multipoint spectral control, and channel equalization. The two-section algorithm overcomes the phase limitation in direct FIR approaches by dynamically decomposes and optimizes the target RF response into a series of Gaussian functions. The algorithm then generates the corresponding parameters for the construction of the optical comb carriers that are used for the reconstruction of the target RF response. It is worth to notice that a flat RF spectral function could be challenging for the current decomposition algorithm to provide high-accuracy decomposition and reconstruction, triangular spectral functions could be added to the decomposition algorithm to tackle the challenge. In the experiment, simultaneous dynamic RF spectral shaping with user-defined shaping

functions in S, C and X bands are successfully achieved. Furthermore, the proposed RF spectral shaper mitigates the optical coarse resolution in most optical to RF spectrum mapping schemes using discrete convolution technique. It is important to note that although coherent FIR approach provides better noise performance than incoherent FIR approach, we believe that the flexibility and shaping capability offered in the proposed incoherent approach still worth the tradeoff. In our previous study[118], the use of incoherent RF filter for spectral shaping results in RF waveforms with acceptable noise performance. The proposed RF spectral shaper is a potential blackbox solution to future software defined radio (SDR) system due to its fully programmable capability and the automatic adaptive RF spectral decomposition and reconstruction processes.

Chapter 5

Bio-Inspired Photonics–Marine Hatchetfish Camouflage Strategies for Dynamic RF Steganography

Camouflage is a strategy that animals utilize for concealment in their habitat, making themselves invisible to their predators and preys. In RF systems, steganography or stealth transmission is the camouflage of information – a technology of hiding and transmitting secret messages in public media. Steganography conceals the secret message in publicly available media such that the eavesdropper or attacker will not be able to tell if there is a secret message to look for. Marine Hatchetfish has two effective camouflage skills to help them hide from their predators – Silvering and Counterillumination. Silvering in Marine Hatchetfish uses its microstructured skin on its sides to achieve destructive interference at colors that could indicate

the presence of the fish, while they also emit light at their bottom part to match its color and intensity to its surrounding, making it invisible from below, refer as counterillumination. In this chapter, we borrow the two underwater camouflage strategies from Marine Hatchetfish, mimic them with photonic phenomena, and apply the camouflage strategies for physical stealth transmission of a 200 MBaud/s 16QAM OFDM secret signal at 5 GHz over a 25-km of optical fiber. The proposed bio-inspired steganography strategies successfully hid the secret signal in plain sight in temporal, RF spectral, and optical spectral domains, by blending in using counterillumination and turning invisible using silvering techniques. The stealth signal can only be retrieved with the precise and correct parameter for constructive interference at the secret signal frequency to unmask the silvering.

5.1 From Marine Hatchetfish to Optical RF Steganography

Camouflage, is a defense and survival strategy that organisms use to disguise their appearance and to blend in with their habitat, such that they can hide from predators and sneak up on prey. For example, stick insect camouflages by having its appearance resemble a tree branch. Artic hare grows grey fur in the summer, but their fur is white in winter to blend in with snow.

In communication systems, camouflage of information is done via steganography or stealth transmission, which is a technology to conceal the presence of secrete message in publicly available media such that the eavesdropper cannot tell if there is a secrete message to look for. Steganography [122] has a long history dated back to the Greeks. The word steganography has two Greek roots, "stegos" means "cover" and "grafia" means "write". Secret message was written on a wooden folding table, and then covered over with wax to make the table appear to be blank. Furthermore, Histiaeus, a ruler in ancient Greece shaved the

head of a messenger and wrote a secret message on it. Once the messenger's hair grew back, the messenger was dispatched with the message. During High Renaissance, Leonardo Da Vinci hid secret messages in his painting including the famous Mona Lisa and the Last Supper.

In modern society, communication networks are an inseparable part of human, that are responsible for supporting applications including telemedicine, online banking, and augmented reality learning. Needless to say, it is essential to protect the massive amount of sensitive and personal information against attackers. Although encryption is usually performed at the media access control (MAC) layer or above, physical layer is one of the most vulnerable places to attack that usually could result in total exposure.

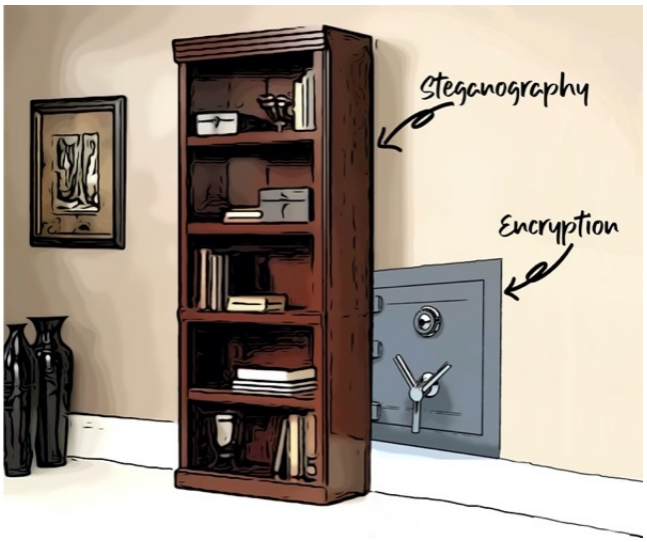

Figure 5.1: Effective cryptography requires both encryption and steganography. It is like storing valuables are in a locked safe (encryption) hidden behind a secret bookcase door (steganography).

Physical encryption techniques have been studied intensively to secure the physical layer [123]–[125], however, physical layer steganography [126] has always been overlooked and its development is still lacking behind. Effective cryptography requires two major components: encryption and steganography. Encryption scrambles the sensitive information so that it is unreadable without the key, while steganography hides the sensitive information within ordinary information so that the attacker will not even know there is a

signal to look for. It is like storing valuables in a locked safe (encryption) hidden behind a secret bookcase door (steganography) – Figure 5.1.

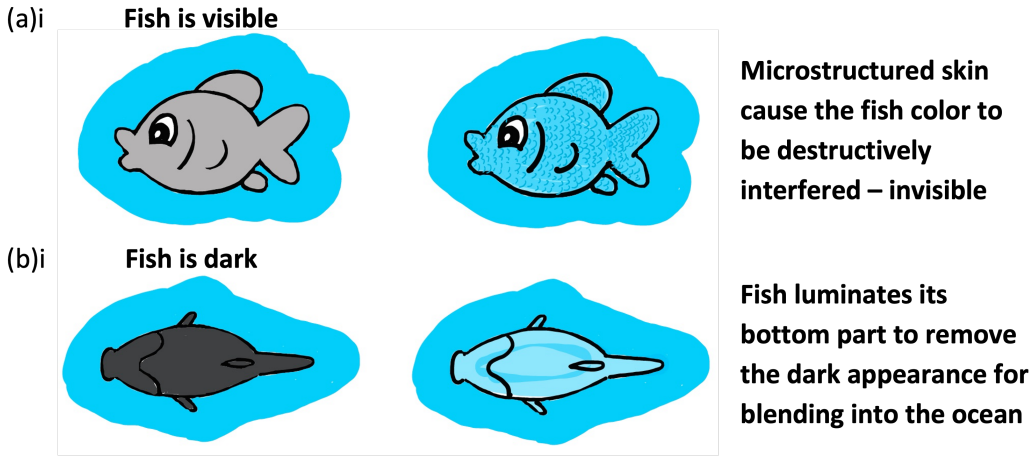

Figure 5.2: Illustration of the two camouflage skills in Marine Hatchetfish. (a) Side view (i) no camouflage - fish is visible (ii) silvering - fish is destructively interfered at colors that could indicate the presence of the fish; (b) Bottom view (i) no camouflage – fish appears darker against the bright water surface when seen from below (ii) counterillumination – fish illuminates itself to the same color and intensity as the background.

Turning to nature for solution, animals conceal their presence in their surroundings via camouflage – an extremely efficient way to ensure their survival. Borrowing camouflage strategies from animals could be an effective solution towards steganography in RF and optical systems. Among different types of camouflage, underwater camouflage is powerful because of the multi-dimensional concealment it can achieve. Underwater camouflage helps sea animals to hide from predators from above the water, being invisible from its side, and removing its dark appearance when seen from below. Marine Hatchetfish [127]–[129] has some of these powerful camouflage skills for survival – silvering and counterillumination, as illustrated in Fig. 5.2. Marine Hatchetfish has microstructured skin on its sides to achieve destructive interference at colors that could indicate the presence of the fish, while constructive interference occurs at colors that is similar to their surroundings, this technique is known as silvering (Fig. 5.2(a)). At the

same time, Marine Hatchetfish also emits light from the bottom part of their body to match its color and intensity to its surrounding to make them invisible from below, referring as counterillumination (Fig. 5.2(b)).

5.2 Existing Optical Steganography Approaches

Information security continue to demanded new strategies to protect sensitive information since most aspects of our society from online social media, mobile computing, security service, health care service, smart city, to online banking are intensively connected and relying on optical and radio frequency (RF) networks [3], [126], [130]. Massive number of sensitive, confidential, and personal information are being transmitted, processed, and stored every second; thus, networks and information have to be protected against malicious attacks to prevent attacker from intercepting or stealing the sensitive information. While encryption is mainly used to protect sensitive information, the presence of the information has not been concealed – meaning that the attacker can still see the presence of the encrypted information and it is just a matter of time for them to decrypt it through approaches like brute force attack. Therefore, effective cryptography requires two major components, encryption and steganography. Encryption scrambles the sensitive information so that it is unreadable without the key, while steganography hides the sensitive information within ordinary information to maintain its secrecy during transmission so that the attacker will not even know there is a signal to look for. Therefore, an effective cryptography scheme could ensure confidentiality, integrity, and authentication of information.

Fiber optics is the backbone of most communication networks that connects cities and nations across oceans and continents, as well as supporting radio-over-fiber transmission of mobile radio frequency signal

(i.e. 5G and WiFi) [1], [2]. Therefore, there is a critical need to physically secure the sensitive information during transmission in the data link using physical cryptography. Physical encryption techniques [131] have been studied intensively and are well developed; however, steganography in the physical layer [11], [132]–[134] have always been overlooked. Physical encryption can be achieved using either optical or electronic approaches. In electronic scheme, chaos mapping can be done by masking [131] or scrambling [135] using digital chaotic signal in passive optical network (PON) at the physical layer. In optical scheme, encryption can be achieved via chaotic lasers [123]–[125] , including nonlinear dynamics for high-quality chaos synchronization [136], semiconductor laser with optical feedback for key space enhancement [137], and double-random phase encoding in the fractional Fourier domain [138]. Electrical RF steganography [139] was proved successfully to hide the digitally modulated communication information via linear chirp radar signals; however, electrical RF steganography systems have a low bandwidth, their electromagnetic wave nature makes them easily suffering from electromagnetic interference and are vulnerable to steganalysis - detecting messages hidden using steganography. On the other hand, optical steganography is mainly done by spreading the stealth signal over an extremely wide optical spectrum (i.e. stealth optical pulse train from mode-locked laser with a wide spectrum [132]), such that the pulse amplitude would be low and can be buried underneath system noise when passing through a dispersive device. To allow the optical carrier to mimic and blend into the system noise, the optical pulse can also be processed to be a noise-like signal at the stealth transmitter using a combination of nonlinear spectral broadening, temporal spreading and power equalizing [140]. To tackle the challenges in conventional optical steganography, direct usage of broadband amplified spontaneous emission (ASE) noise [133] is thus a good candidate such that the stealth signal could be fully buried under the system noise with the same noisy signature. Transmission

of optical stealth signal in optical fiber makes it very challenging for the attacker to pick up any signature of the stealth signal without being detected.

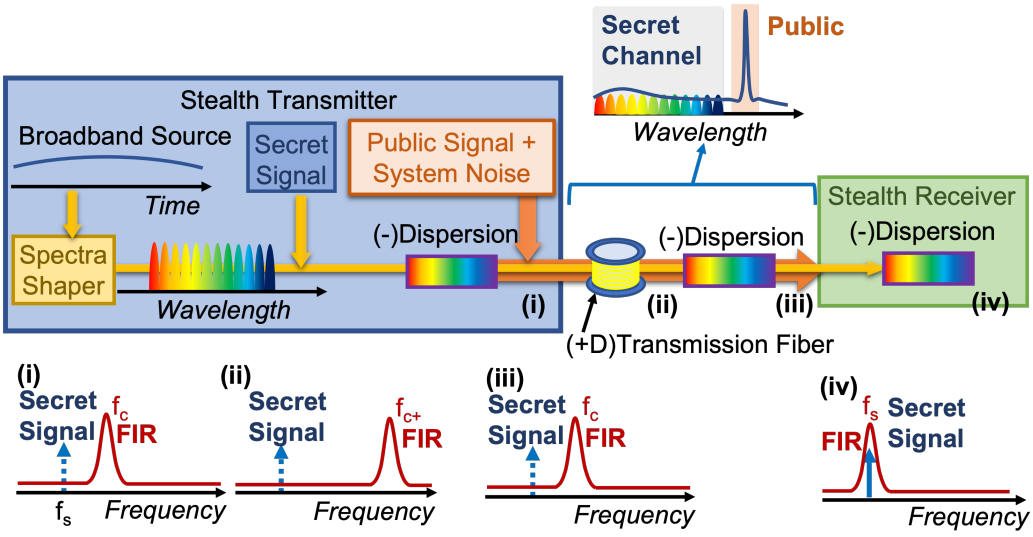

Figure 5.3: Illustration of the proposed bio-inspired optical steganography for RF signal transmission over the fiber. (i) Silvering – photonic RF FIR creates destructive interference condition at the stealth signal frequency (fs); (ii) Transmission in optical fiber will only push the constructive interference condition to a much higher frequency (fc+); (iii) Dispersion compensation fiber at the last section of the transmission will move the constructive interference condition back to fc; (iv) Correct dispersion at the stealth receiver allows constructive interference condition to occur at the stealth signal frequency fs.

In this section, we borrow the two camouflage techniques from Marine Hatchetfish – silvering and counterillumination, mimic the techniques using photonics, and apply them as optical steganography techniques for stealth transmission of OFDM signal in radio-over-fiber networks. The mimicking of silvering – the use of destructive interference at the fish color to make it invisible to predators, is achieved using an optical finite impulse response (FIR) structure such that the stealth signal is destructively interfered to the attacker at any point of the transmission. While the mimicking of counterillumination – the production of light to match their backgrounds in both brightness and color, is achieved using a wide-band low intensity light as the optical carrier to match with the background noise in the system. Unlike most existing optical steganography schemes, the proposed bio-inspired steganography does not just bury

the stealth signal underneath system noise, but it also using destructive interference at the stealth signal frequency to make the stealth signal to be invisible and disappear in the attacker's eyes.

5.3 Bio-inspired Steganography Measure Based on Microwave Photonics

5.3.1 Working principle

[1] Figure 5.3 is the design of the bio-inspired optical steganography scheme. To achieve counterillumination, a broadband ASE source generated from an erbium doped fiber amplifier (EDFA) is used as the optical carrier for the stealth OFDM signal to "illuminate" at the same wavelength and intensity as the background system noise, such that no distinct optical spectral component is observed. The broadband ASE source is spectrally sliced for achieving a desired photonic RF FIR in RF domain [36] when passing through dispersive medium for "silvering", such that destructive interference at the stealth signal frequency (f_s) is resulted in the attacker's view, hiding the signal in both RF spectral domain and temporal domain. The constructively interfered frequency (f_c) will be way above the frequency range of interest – i.e. nothing will be observed since there is no signal transmission at that frequency range. The stealth-modulated broadband optical carrier is combined with the public signal and system noise for transmission, resulting in a complete submerging of the stealth signal underneath the system noise, hiding the stealth signal in the optical spectral domain. The transmission fiber has a positive dispersion sign that will further move the constructively interfered frequency to an even higher frequency (f_{c+}) as the signal propagates – much

[1] **Q. Liu**, M. P. Fok. "Bio-inspired photonics – marine hatchetfish camouflage strategies for RF steganography." Optics Express 29.2 (2021): 2587-2596.

further away from the stealth signal frequency. In most optical network, dispersion compensating fiber with negative dispersion is placed at the last section of the transmission to correct any temporal spreading caused by the transmission fiber. The presence of the dispersion compensating fiber will move the constructive interference frequency back to f_c. The attacker will not be able to observe any trace of the stealth signal in the optical spectrum, RF spectrum, or time domain at any point of the transmission. As a result, there is no reason for the attacker to attack the "empty" channel, successfully achieving steganography. At the intended receiver, a precisely matched dispersion is needed to achieve constructive interference at the stealth signal frequency f_s, revealing the stealth signal. Due to the broadcast characteristic of PON, other public receiver will just treat the secret channel as system noise.

5.3.2 Experimental details

Experimental setup of the proposed bio-inspired optical steganography for OFDM-PON is shown in Fig. 5.4. Optical broadband source from an erbium doped fiber amplifier (EDFA) that covers the wavelength range from 1528 to 1568 nm is shaped to 20 nm wide and sliced by an optical wave shaper (Finisar 1000S). The dual channel 12 Gb/s arbitrary waveform generator (AWG, Keysight 8190A) is used to generate both the stealth signal and the public signal. The stealth RF signal is modulated onto the shaped optical source using a 12 GHz electro-optic intensity modulator (MZM). The stealth signal-modulated optical carrier is then launched to a dispersion compensation fiber (DCF1) to introduce proper time delay between taps for generating the photonic RF FIR. It is important to note that while we are using a 1.5 km DCF1 with dispersion coefficient of -255 ps/nm at the stealth transmitter in the experiment, the dispersion can be chosen to any value as long as the resultant FIR constructive interference condition occurs at a higher frequency than the stealth signal frequency. Meanwhile, the public signal is directly modulated onto a

DFB laser output at 1553.33 nm. In our experiment, amplified spontaneous emission (ASE) noise is added to mimic the wideband system noise that are normally found in long-haul transmission system. The stealth signal, public signal, and system noise are combined and transmitted through a 25-km standard single mode fiber (SMF) followed by a 2.5-km DCF2 for dispersion compensation in a PON. A three-port thin film filter (TFF) with 3-dB bandwidth of 0.3 nm and center wavelength at 1553.33 nm is used to drop the public channel to the public receiver, leaving the hidden stealth signal for the stealth receiver. To observe the stealth signal, precise knowledge of the amount of dispersion is needed for constructive interference condition to occur at the stealth signal frequency, which is only known to the stealth receiver but not the attacker. After passing through DCF3 at the stealth receiver, the stealth signal is converted back to the electrical domain using a photodetector and is captured using a 128 GSa/s real-time sampling oscilloscope (Keysight UXR0334A Infiniium) with 33 GHz bandwidth for offline digital signal processing.

To design the desired photonic RF finite impulse response with center frequency f_{FIR} the corresponding optical comb should have a FSR $\Delta\lambda_{FSR}$ governed by the following equation,

$$\Delta\lambda_{FSR} = \frac{1}{|D(L_{DCF1} + l_{DCF3})|f_{FIR}} \tag{5.1}$$

where D, L_{DCF1}, L_{DCF3} denote dispersion coefficient, the length of the DCF1 and DCF3, respectively. The center frequency (f_{FIR}) will be right at the stealth signal frequency f_s after passing through all the optical fiber (i.e. DCF1, SMF, DCF2, and DCF3). However, the FIR center frequency f_{FIR} will be away from f_s at any point after the transmitter and before the end of DCF3. The large key space provided by the total dispersion make it difficult to discover, search, or retrieve the stealth signal without the precise knowledge of the correct dispersion. Then, the overall shape of the optical comb is designed such that it

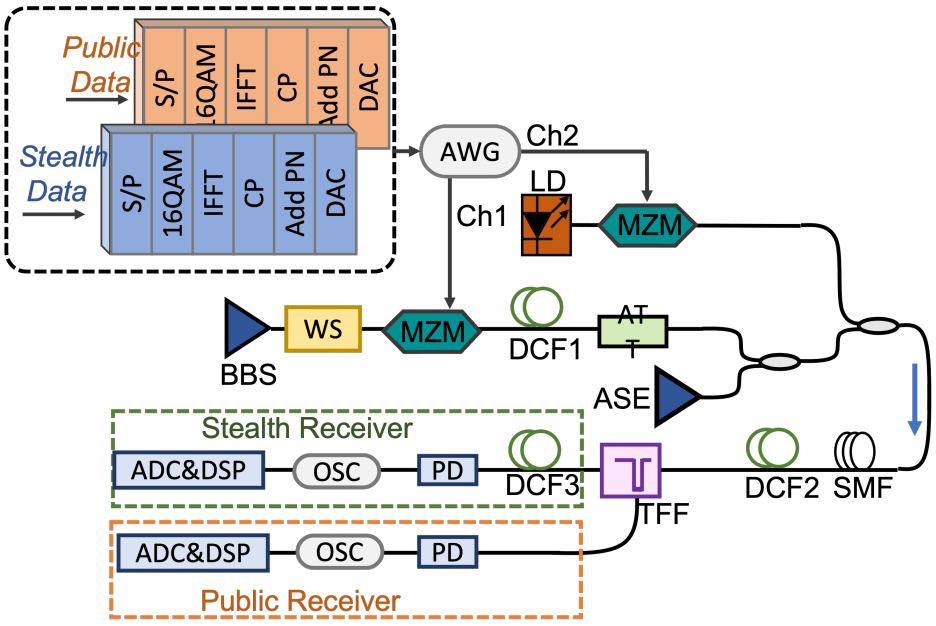

Figure 5.4: Experimental demonstration of the proposed bio-inspired steganography scheme. BBS: broadband optical source; WS: optical wave shaper; MZM: electro-optic intensity modulator; DCF1-3: dispersion compensating fiber; ATT: optical attenuator; AWG: arbitrary waveform generator; ASE: amplified spontaneous emission; DFB: distributed feedback laser diode; SMF: single mode fiber; TFF: thin-film filter; PD: photodetector; OSC: real-time sampling oscilloscope.

is the correct RF filter profile at the stealth receiver for retrieving the stealth signal [64]. Therefore, the needed optical spectral shaping function can be expressed as:

$$T(\lambda) = cos(\frac{\Delta\lambda_{full}}{\Delta\lambda_{FSR}} \cdot \frac{\lambda}{2}) \exp\left(-\frac{\lambda^2}{2\Delta\lambda_{FWHM}^2}\right) \tag{5.2}$$

where $\Delta\lambda_{full}$, $\Delta\lambda_{FWHM}$ are the total shaped optical bandwidth and full width half maximum (FWHM) optical bandwidth, respectively. It is important to mention that the stealth signal will survive any inline optical amplifier that are intended to amplify the public signal. Fig. 5.5 shows experimental studies of the dynamic RF filter design. In most scenarios, the length of the DCF and SMF cannot be changed easily; therefore, we will mainly change the FSR of the optical comb carrier to achieve the desired FIR frequency, as shown in Fig. 5.5(a). The goal is to set the whole constructive interference band to be completely outside of the stealth signal RF spectrum during the whole transmission. In this experiment, the dispersion of the 1.5-km DCF1 and DCF3, 2.5-km DCF2, and 25-km SMF are -255 ps/nm, -425 ps/nm, and +425 ps/nm, respectively. An example of the shaped optical comb carrier is shown in Fig. 5.5(b). Fig. 5.5(c) is measured by a RF network analyzer showing the capability to tune the resultant RF response to different frequency for achieving destructive interference condition at different stealth signal frequency (f_s). The preliminary results prove the feasibility of using the proposed design algorithm for designing RF filters with high flexibility and customizability.

5.3.3 Results and discussion

In this experiment, our goal is to perform stealth transmission of a 200 MBaud/s 16 QAM-OFDM signal at 5 GHz. Optical comb carrier with spacing of 0.317 nm is used such that destructive interference condition

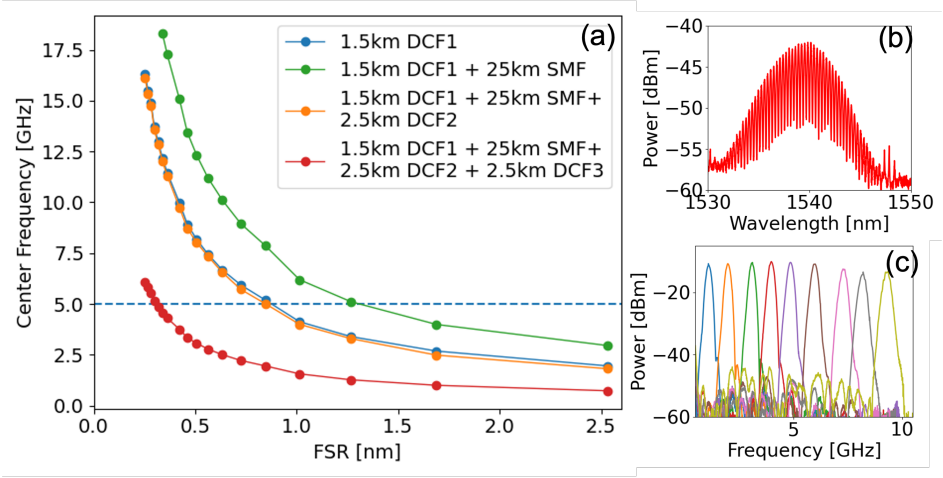

Figure 5.5: (a) Relationship between constructive interference frequency (f_{FIR}) and the designed FSR of the optical comb carrier at different fiber combinations; (b) Measured optical spectrum of the shaped optical comb carrier; (c) Tunable and reconfigurable constructive interference peaks at different frequencies.

is achieved at 5 GHz (stealth signal frequency) but a constructive interference condition at 13.22 GHz (solid red in Fig. 5.6(a)) at the transmitter. Constructive interference condition can only be achieved at 5 GHz (stealth signal frequency) when the accumulated dispersion is -680 ps/nm at the stealth receiver, as shown by the dashed brown line in Fig. 5.6(a). Thus, no stealth signal can be observed at the starting point of the transmission. As the stealth signal propagates in the SMF, the positive dispersion value of SMF will always reduce the total amount of dispersion. Thus, the constructive interference frequency will always be moved further up to a higher frequency f_{c+} (solid orange) while keeping the stealth signal invisible at any point along the SMF. During standard dispersion compensation in a PON or radio over fiber network, the amount of dispersion compensation will move the constructive interference frequency back to a slightly lower frequency f_{c-} (solid green and purple) but will not be enough to move it back all the way to the stealth signal frequency, keeping the stealth signal invisible at any location of the transmission.

The constructive interference condition can only be moved back to the stealth signal frequency if the correct dispersion is used at the stealth receiver (dashed brown curve in Fig. 5.6(a)). The noise floor at the RF spectrum is at -50 dBm and can be improved by 10 dB using balanced detection [141].

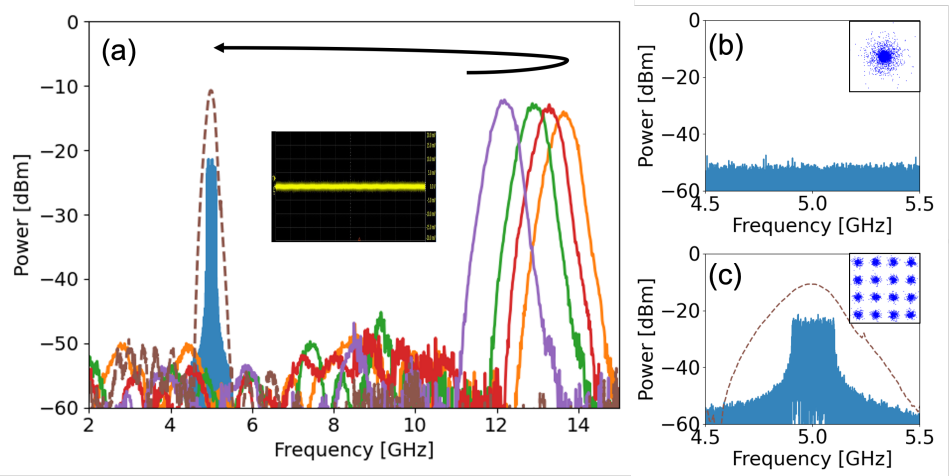

Figure 5.6: Experimental results of the bio-inspired steganography scheme for the concealment of stealth signal. (a) State1(red): constructive interference condition occurs at 13.22 GHz after DCF1, State 2(Orange): positive dispersion of the SMF will move constructive interference condition to higher frequency; State 3(green/purple): DCF 2 is used to compensate the dispersion of SMF in public transmission nodes that moves the constructive interference peak to a slightly lower frequency; State 4(dashed brown): the matched dispersion at stealth receiver will shift the constructive interference condition to the stealth signal frequency at 5 GHz; (b) RF spectrum and constellation diagram measured during transmission without a correct stealth receiver (c) RF spectrum and constellation diagram measured at the stealth receiver with correct dispersion.

When the public signal is removed, we examined the received signal at the stealth receiver without applying a correct dispersion. The stealth signal is not visible in neither time domain nor RF spectral domain, as shown in Fig. 5.6(a) inset and Fig. 5.6(b), respectively. Furthermore, the corresponding constellation diagram as shown by the inset of Fig. 5.6(b) does not show any sign of the stealth signal – a noise like diagram is resulted. Even if the eavesdropper tries to tap into the transmission fiber directly at different locations of the transmission, no trace of the stealth signal can be observed because the 5 GHz stealth frequency is at destructive interference along the whole transmission (as shown by the solid color

curves in Fig. 5.6(a)), just like the silvering camouflage technique that Marine Hatchetfish is using. At the stealth receiver, the stealth signal can be retrieved only if the correct dispersion is used, such that constructive interference condition occurs precisely at 5 GHz, i.e. the stealth signal frequency. Fig. 5.6(c) shows the resultant constructive interference at 5 GHz (brown dashed) with the RF spectrum of the stealth signal shown in blue, and a clear constellation diagram shown in the inset.

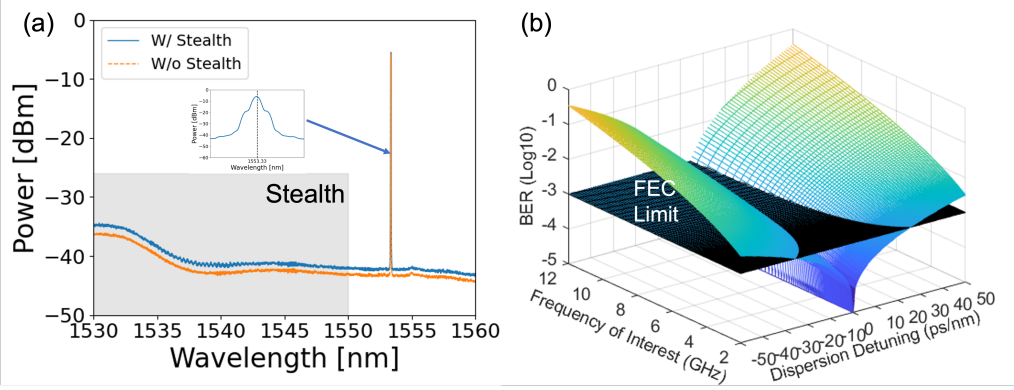

Figure 5.7: (a) Measured optical spectra of the transmission with (blue) and without (orange) the stealth signal. (b) Simulated mesh plot of the BER change with respect to the dispersion mismatch and the stealth signal frequency.

Just like the Marine Hatchetfish where multiple camouflage skills are used to conceal its appearance in different view, the proposed optical steganography scheme also utilize a second stealth technique to conceal its appearance in the optical spectral domain too. Marine Hatchetfish uses counterillumination to illuminate itself to the same color and intensity as the background such that it will not appear dark against the bright water surface when seen from below. Here, the use of incoherent broadband optical comb source acts like the counterillumination in Marine Hatchetfish, such that the stealth signal's appearance is similar to the ASE system noise. The broadband optical comb source has successfully concealed the trace of stealth signal in optical spectral domain under the system noise, as shown in Fig. 5.7(a). In case the eavesdropper attempts to use coherent detection technique to detect the phase of the transmission

that includes both the system noise and the stealth signal, the bandwidth of coherent detection is limited by the photodiode and analog-to-digital conversion capability, which is in the order of 100 GHz [142], corresponding to only 2% of the ASE noise and broadband comb source bandwidth used for the stealth signal, preventing the eavesdropper from digitizing or recording signal that is buried under the noise.

The goal of steganography is to conceal the stealth signal such that the attacker will not know if there is a signal to look for. It is important to know whether it is easy to unintentionally get the dispersion close enough to unconcealed the stealth signal. Therefore, we study the dispersion tolerance of the proposed bio-inspired optical steganography scheme by investigating the relationship between BER, stealth signal frequency, and the dispersion offset, as shown in Fig. 5.7(b). To successfully demodulate a 16QAM-OFDM signal, a forward error correction (FEC) threshold of 1×10-3 is needed, as shown by the dark blue horizontal plane in Fig. 5.7(b). As observed, the dispersion needs to be within ±10 ps/nm dispersion mismatch to retrieval the hidden stealth signal at 5 GHz correctly. Stealth signal with higher center frequency could increase the robustness of stealth transmission due to the tighter requirement of dispersion matching. The broadband characteristic of the optical comb makes the use of tunable dispersive device to monitor the stealth channel impossible. Commercially available dispersion-tunable compensation module usually either has very small bandwidth and dispersion, or has specific channel spacing, i.e. 0.8 nm. It would also be impossible for the eavesdropper to physically switch out wideband fixed dispersive medium to apply brute force attack to guess the dispersion. Furthermore, the estimation of dispersion using coherent detection could easily fail due to the wideband and incoherent nature of the broadband optical carrier that carries the stealth signal [143]. Therefore, the proposed bio-inspired steganography scheme is effective in terms of both prevention of stealth signal detection and inhibiting signal recovery.

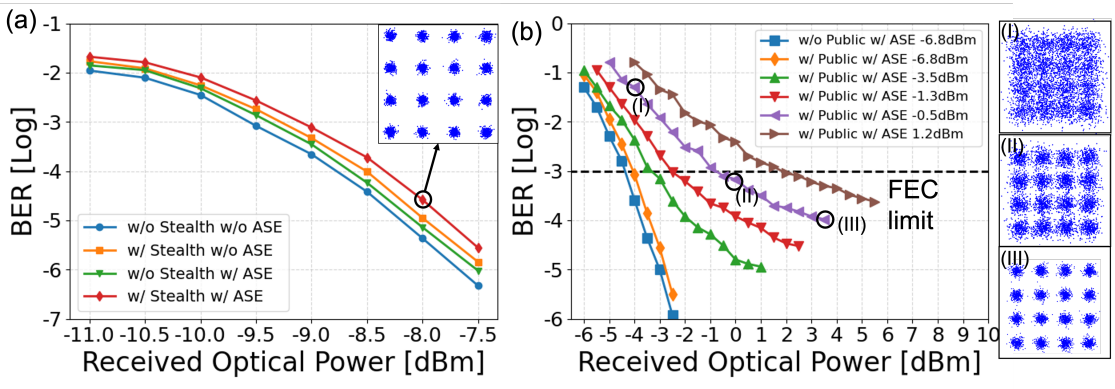

Figure 5.8: (a) BER measurements and constellation diagram of the public channel with and without stealth signal and system noise (ASE); (b) BER measurements and constellation diagrams of the stealth channel signal under different system noise power.

While the concealing of stealth signal is important, the transmission performance of the stealth signal and the public signal are equally important. BER measurements and constellation plots of the public and stealth signals are investigated. Fig. 5.8(a) shows the measured BER of the public channel with and without stealth signal and system noise, which indicates that only 0.2 to 0.4 dB power penalty is resulted when the stealth signal is added. The addition of system noise will add another 0.3 dB of power penalty to the public signal. Fig. 5.8(b) shows the BER measurement of the stealth signal when different amount of system noise is added to the transmission for better concealment. In our experiment, it is observed that a power penalty is increased while still below FEC limit as the system noise is increased. Comparing the orange and blue curves, the presence of public signal has insignificant effect on the stealth signal BER. Constellation diagrams of the stealth signal at various received power are shown in Fig. 5.8(b)(i)-(iii), indicating that the stealth can be retrieval successfully if BER is below the FEC limit.

5.4 Summary

In summary, we presented a bio-inspired optical steganography scheme for enhancing the security of RF signal transmitting in radio-over-fiber and optical networks. Our approach borrows the silvering and counterilluminate camouflage strategies in Marine Hatchetfish, mimic it with photonics, and experimentally apply it in the stealth transmission of 16QAM OFDM signal. Silvering is achieved by the generation of destructive interference condition at the stealth signal frequency for the concealing of signal using photonic RF FIR, while counterilluminate is achieved by using a broadband optical comb source to blend in the wideband system noise. The proposed bio-inspired steganography scheme is an important part in cryptography when using with optical encryption. In our experiment, a 200MBaud/s 16QAM OFDM stealth signal at 5 GHz is successfully concealed in temporal domain, RF spectral domain, and optical spectral domain. Moreover, the proposed stealth transmission design could potentially simplify the remote node function in future 5G network and beyond for secure communication since the reveal of stealth is done physically without the need of high-speed digital signal process.

Chapter 6

Conclusions and Future Work

6.1 Conclusions and Limitations

6.1.1 Conclusions

In this dissertation, various dynamic and adaptive RF systems enabled by photonic technologies are theoretically analyzed and experimentally demonstrated. The essence of the dynamic RF systems can be divided into three parts: dynamic spectral usages, dynamic spectral processing and dynamic security. And the adaptiveness of the developed RF systems is reflected by the high-speed, wideband and reconfigurable hardware and software design, as well as the capability of identifying, switching, controlling and compensating ambient complicated communication environment and signal.

Based on the two themes (i.e. dynamic and adaptive) of this dissertation, we started from the demonstration of instantaneous microwave frequency estimation by PM-Lyot architecture, which can achieve dual-function frequency measurement and Doppler frequency shift. Then, a data-driven method is used

based on complementary optical power measurement.The absolute measurement error is significantly reduced to 50 MHz with a RMSE of only 1.1 MHz. After RF signal identification, real-time RF switching is also achieved, 50 ps signal switching of amplitude, frequency and phase based on polarization-dependent and transmission transparent nonlinear four wave mixing. RF signal switching technique can also be used to generate frequency hopping signal with instantaneous switching speed to improve security and signal fidelity of high capacity RF systems. Later on, we moved on to the wideband and reconfigurable RF response control and management. Independent spectral shape, amplitude, bandwidth, group delay and number of passbands reconfiguration for each passband are successfully achieved. We also proposed a decomposition and reconstruction algorithms, which can adaptively decompose the received RF wideband response into summation of Gaussian basis and reconstruct its complementary spectral response to compensate it in S,C,X bands. That is, point-by-point spectral shaper enabled by photonics is achieved. Furthermore, a dynamic RF over fiber security strategy inspired by Marine Hatchetfish is developed and experimentally demonstrated. Our approach borrows the silvering and counterilluminate camouflage strategies in Marine Hatchetfish, mimic it with photonics, and experimentally apply it in the stealth transmission of 16QAM OFDM signal. Briefly, silvering is achieved by the generation of destructive interference condition at the stealth signal frequency for the concealing of signal using photonic RF FIR, while counterilluminate is achieved by using a broadband optical comb source to blend in the wideband system noise.

6.1.2 Limitations and outlook

This dissertation fulfill the proposed research goal for dynamic and adaptive RF systems enabled by photonic technology. However, there are still several limitations identified during our research:

- Although the proposed instantaneous frequency measurement system can achieve wideband dual-function measurement, only single tone signal can be measured. However, it is highly desired to achieve multi-tone measurement in the future due to the complex unknown RF environment. One possible solution is frequency-to-time mapping.

- In the data-driven frequency estimation project, the interpretability of black-box machine learning still has room for improvement. Although it has successfully overcome the issue resulted from non-linearity during modulation as well as the over-fitting problem for most of post-processing data analysis, it is not clear to most audience that the model selection rule and how to further improve the model.

- We have only demonstrated the real-time switching of amplitude, phase and frequency properties. The high-speed RF switching scheme using the proposed real-time RF switching approach could potentially be translated to multilevel frequency switching, providing a more complex hopping pattern and improve information security during transmission.

- The resolution of the demonstrated RF spectral shaper is strictly limited by the addressibility of the optical wave shaper. Also, there is a trade-off between number of control point and control point resolution due to their optical properties might mask each other once more combs are introduced. Thus, it is potential to use $1 \times N$ paralell shaping with Nx degree of freedom manipulation.

- Currently, the bio-inspired optical steganography scheme is demonstrated single band stealth transmission. The implementation of multi-channel stealth transmission without significant performance degradation is still under development.

6.2 Future Work

Although abundant processing bandwidth, the availability of low-loss optical fiber as a transport medium and the flexibility in tailoring the RF response are obtained by up-converting RF signal to optical frequency in microwave photonic system. The demonstrated approaches are a benchtop configuration consisted of relatively discrete fiber-optic components, which are sensitive to peripheral environment such as temperature changes and vibration. Besides, optical loss in MWP systems is important because an increase in this parameter translates quadratically into RF loss in RF circuits [104], [144]. Consequently, leveraging photonic integration allowed a dramatic reduction in the footprint of MWP systems with fairly high complexity, making them more comparable to RF circuits. Integration brings advantages to functions such as optical modulation, generation, processing and measurement of microwave signals, but also enhances their performance. To minimize and implement the proposed dynamic and adaptive RF systems in practical communication applications (i.e. Internet of Things, 5G.), compact photonic integration is needed. Here, a summary of the most advanced technological tools based on integrated photonics are shown in Table 6.1,

Table 6.1: Investigation of Photonic Integration

YEAR	FUNCTIONALITY	PIC TECHNOLOGY	SIZE	LOSS
2018	**Laser source[145]**	III–V/silicon	0.4 x 2.4 mm^2	NA
2018	**Optical filter [146]**	silicon-on-insulator	0.55 x 2.5 mm^2	5.4 dB
2018	**Optical modulator [147]**	lithium niobate	1.5 x 5 mm^2	0.5 dB
2017	**Optical delay line [148]**	silicon-on-insulator	5.4 x 5.3 mm^2	12.4 dB
2015	**Polarization [149]**	silicon-on-insulator	2.4 x 2.4 um^2	NA
2017	**Circulator [150]**	silicon-on-insulator	3.5 mm	9.2 dB
2015	**Photodetector [151]**	silicon-on-insulator	0.4 x 0.4 mm^2	NA

In the future work, it is promising to explore and integrate the proposed approaches on SOI platform, collaborating with foundry plan (e.g. AIM Photonics, Globalfoundries, etc.).

Appendix A

Publications during Study

[J1] **Q. Liu**, Benjamin Gily, and M. P. Fok. "Adaptive Photonic Microwave Instantaneous Frequency Estimation Using Machine Learning." IEEE Photonics Technology Letters (under revision).

[J2] **Q. Liu**, M. P. Fok. "Bio-inspired photonics – marine hatchetfish camouflage strategies for RF steganography." Optics Express 29.2 (2021): 2587-2596.

[J3] **Q. Liu**, M. P. Fok. "Adaptive photonic RF spectral shaper." Optics Express 28.17 (2020): 24789-24798.

[J4] M. Yang, **Q. Liu**, H. S. Naqawe and M. P. Fok. "Movement Detection in Soft Robotic Gripper Using Sinusoidally Embedded Fiber Optic Sensor." Sensors 20.5 (2020): 1312.

[J5] **Q. Liu**, M. P. Fok. "Real-Time RF Multi-Dimensional Signal Switching Using Polarization-Dependent Optical Mixing ", IEEE Photonics Journal, 12.2 (2020):1-8.

[J6] **Q. Liu**, M. P. Fok. "Ultrafast and Wideband Microwave Photonic Frequency-Hopping Systems: A Review." Applied Sciences, 10.2 (2020): 521.

[J7] **Q. Liu**, J. Ge, M. P. Fok. "Microwave photonic multiband filter with independently tunable passband spectral properties." Optics Letters, 43 (2018): 5685 - 5688.

[C1] **Q. Liu** and M. P. Fok. "Data-Driven Complementary Power Measurement for Microwave Instantaneous Frequency Estimation." IEEE Research and Applications of Photonics in Defense Conference, TuC4.3, 2021.

[C2] **Q. Liu** and M. P. Fok. "Bioinspired Photonics: Camouage Strategies from Marine Hatchet sh for Optcial RF Steganography." IEEE Research and Applications of Photonics in Defense Conference, MD1.4, 2021.

[C3] **Q. Liu** and M. P. Fok. "Adaptive Microwave Photonic Spectral Shaper for RF Response Tailoring." Optical Fiber Communication Conference (OFC), M3H.4, 2020.

[C4] L. Zheng, Z. Liu, Z. Zhang, S. Xiao, **Q. Liu** and M. P. Fok. "Self-adaptive over-the-air RF self-interference cancellation based on signal-of-interest driven regular triangle algorithm." Optical Fiber Communication Conference (OFC), M3H.4, 2020.

[C5] **Q. Liu** and M. P. Fok. "Real-time Temporal Signal Stitching Using Polarization-Dependent Optical Wave Mixing." Frontiers in Optics, FTu5B.4, 2019.

[C6] **Q. Liu** and M. P. Fok. "Dual-function Frequency and Doppler Shift Measurement System Using a Phase Modulator Incorporated Lyot Filter." Optical Fiber Communication Conference (OFC), Th2A. 36, 2019.

[C7] M. P. Fok, J. Ge, and **Q. Liu**. "Dynamic and multiband RF spectral processing." Smart Photonic and Optoelectronic Integrated Circuits XXI. Vol. 10922. International Society for Optics and Photonics, 2019.

[C8] J. Ge, D. Garon, **Q. Liu** and M. P. Fok. "Reconfigurable microwave photonic spectral shaper." Optical Fiber Communication Conference (OFC), W2A. 36, 2019.

[C9] G. V. Pérez, **Q. Liu**, M. P. Fok. "Stretchable Fiber Optic Sensors for Soft Robotics." BMES, P-SAT-458, 2018.

Appendix B

Matlab Code for Programmable Optical Waveshaper

```
function pushbutton1_Callback(hObject, eventdata, handles)
% hObject    handle to pushbutton1 (see GCBO)
% eventdata  reserved - to be defined in a future version of MATLAB
% handles    structure with handles and user data (see GUIDATA)
distance = str2num(get(handles.edit3,'String'));
Ld = distance*1e3;
beta2 = str2num(get(handles.edit4,'String'));
beta2_DCF = beta2*1e-25;%s2/m

RFcenter(1) = str2num(get(handles.edit5,'String'));
RFcenter(2) = str2num(get(handles.edit6,'String'));
RFcenter(3) = str2num(get(handles.edit7,'String'));
RFcenter(4) = str2num(get(handles.edit8,'String'));
RFcenter(5) = str2num(get(handles.edit9,'String'));
RFcenter(6) = str2num(get(handles.edit10,'String'));
RFcenter(7) = str2num(get(handles.edit20,'String'));
RFcenter(8) = str2num(get(handles.edit21,'String'));
RFcenter(9) = str2num(get(handles.edit22,'String'));
RFcenter(10) = str2num(get(handles.edit23,'String'));
RFcenter(11) = str2num(get(handles.edit24,'String'));
RFcenter(12) = str2num(get(handles.edit25,'String'));
```

```
RFcenter(13) = str2num(get(handles.edit26,'String'));
RFcenter(14) = str2num(get(handles.edit27,'String'));
RFcenter(15) = str2num(get(handles.edit28,'String'));
RFcenter(16) = str2num(get(handles.edit29,'String'));

N = str2num(get(handles.edit49,'String'));
for i = 1:N
    RFcenter(i) = RFcenter(i)*1e9;
end

FSR = zeros(1,N);
for i = 1:N
    FSR(i) = ...
        roundn((1/RFcenter(i))/(beta2_DCF*Ld*2*pi)*0.08/10e9,-3);%in nm
end
set(handles.uitable1,'Data',FSR');

A = zeros(1,16);
A(1) = str2num(get(handles.edit32,'String'));
A(2) = str2num(get(handles.edit33,'String'));
A(3) = str2num(get(handles.edit34,'String'));
A(4) = str2num(get(handles.edit35,'String'));
A(5) = str2num(get(handles.edit36,'String'));
A(6) = str2num(get(handles.edit37,'String'));
A(7) = str2num(get(handles.edit38,'String'));
A(8) = str2num(get(handles.edit39,'String'));
A(9) = str2num(get(handles.edit40,'String'));
A(10) = str2num(get(handles.edit41,'String'));
A(11) = str2num(get(handles.edit42,'String'));
A(12) = str2num(get(handles.edit43,'String'));
A(13) = str2num(get(handles.edit44,'String'));
A(14) = str2num(get(handles.edit45,'String'));
A(15) = str2num(get(handles.edit46,'String'));
A(16) = str2num(get(handles.edit47,'String'));

wv_matrix = zeros(5026,4);
wv_matrix(:,1) = 191.25:0.001:196.275;  %THz
wv_matrix(:,2) = 50;                    %dB
wv_matrix(:,3) = 0;                     %phase rad
wv_matrix(:,4) = 1;

c = 2.99792458e5;
f_range = wv_matrix(:,1);
wl_range = c./f_range; %convert to wavelength
```

```
65
66  start_wl =  str2num(get(handles.edit1,'String'));
67  f_h = c/start_wl;
68  end_f = roundn(f_h,-3);
69
70  end_wl = str2num(get(handles.edit2,'String'));
71  f_l = c/end_wl;
72  start_f = roundn(f_l,-3);
73
74  bandwidth = end_wl - start_wl; %in nm
75  f_start_point = find(abs(wv_matrix(:,1)-start_f)<1e-13);
76  f_end_point = find(abs(wv_matrix(:,1)-end_f)<1e-13);
77  central_f = roundn((start_f+end_f)/2,-3);
78  central_point = find(abs(wv_matrix(:,1)-central_f)<1e-13);
79  central_wl = wl_range(central_point);
80
81  % normalize the frequency range
82  f = f_range - central_f;
83
84  f_range_0 = f_range(f_start_point:f_end_point);
85  f_range_mean = mean(f_range_0);
86  f_range_2 = f_range_0 - f_range_mean;
87  m = max(f_range_2);
88  f_range_2 = f_range_2./m;
89  f0 = f_range_2;
90
91  B = zeros(1,N);
92  for i = 1:N
93      B(i) = ceil(bandwidth/FSR(i)/2);
94  end
95
96  % plot(handles.axes1,f0,10*log10(subwav));
97
98  for i = 1:N
99      chirpp(:,i) = cos(2*pi*B(i)*f0);
100     chirppp(:,i) = mapminmax(chirpp(:,i)', 0, 1)';
101 end
102
103 H_FWHM(1) = str2num(get(handles.edit50,'String'));% 0.21 normal
104 H_FWHM(2) = str2num(get(handles.edit53,'String'));% 0.21 normal
105 H_FWHM(3) = str2num(get(handles.edit54,'String'));% 0.21 normal
106 H_FWHM(4) = str2num(get(handles.edit55,'String'));% 0.21 normal
107 H_FWHM(5) = str2num(get(handles.edit56,'String'));% 0.21 normal
108 H_FWHM(6) = str2num(get(handles.edit57,'String'));% 0.21 normal
```

```
109
110 sign(1) = str2num(get(handles.edit58,'String'));% 0.21 normal
111 sign(2) = str2num(get(handles.edit59,'String'));% 0.21 normal
112 sign(3) = str2num(get(handles.edit60,'String'));% 0.21 normal
113 sign(4) = str2num(get(handles.edit61,'String'));% 0.21 normal
114 sign(5) = str2num(get(handles.edit62,'String'));% 0.21 normal
115
116 for i = 1:N
117     H_shaper(:,i) = exp(-f_range_2.^2/(2*(H_FWHM(i).^2)));
118 end
119 %%tri to test combination of gaussian and tri
120 k = 1.95;% 1 normal
121 H_shaper_tri = sinc(f_range_2*k*pi).^2;
122 log_htri = log(H_shaper_tri);
123
124 normal_shaper = zeros(5026,1);
125 for i = 1:N
126     if sign(i) == 1
127         normal_shaper(f_start_point:f_end_point) = ...
               normal_shaper(f_start_point:f_end_point) + A(i) * ...
               chirppp(:,i).*H_shaper(:,i);
128     elseif sign(i) == 0
129         normal_shaper(f_start_point:f_end_point) = ...
               normal_shaper(f_start_point:f_end_point) + A(i) * ...
               chirppp(:,i).*H_shaper_tri;
130     end
131 end
132 plot(handles.axes1,log_htri);
133
134 figure(1)
135 plot(log_htri);
136
137
138 normal_shaper = mapminmax(normal_shaper', 0, 1)';
139 log_shaper = 10*log10(normal_shaper);
140
141 plot(handles.axes2,wl_range,normal_shaper);
142 plot(handles.axes3,wl_range,log_shaper);
143
144 maxloss = 50; %Set the minimal loss value
145 wv_matrix(f_start_point:f_end_point,2) = - ...
      log_shaper(f_start_point:f_end_point);
146 for i = 1:5026
147     if wv_matrix(i,2) ≥ maxloss
```

```
148             wv_matrix(i,2) = maxloss;
149         end
150     end
151     plot(handles.axes4,wl_range,wv_matrix(:,2))
152
153     name2 = get(handles.edit48,'String');
154     % h = length(name2);
155     % set(handles.edit48,'string',h);
156     name3 = name2(1);
157     for i = 2:length(name2)
158         name3 = strcat(name3,name2(i));
159     end
160     filen=strcat(name3,'.wsp');
161     fid = fopen(filen,'wt');
162     for i = 1:5026
163       fprintf(fid,'%.3f\t',wv_matrix(i,1));
164       fprintf(fid,'%.3f\t',wv_matrix(i,2));
165       fprintf(fid,'%.2f\t',wv_matrix(i,3));
166       fprintf(fid,'%d\n',wv_matrix(i,4));
167     end
168     fclose(fid);
```

Bibliography

[1] R. Waterhouse and D. Novack, "Realizing 5g: Microwave photonics for 5g mobile wireless systems," *IEEE Microwave Magazine*, vol. 16, no. 8, pp. 84–92, 2015.

[2] G.-K. Chang and C. Liu, "1–100ghz microwave photonics link technologies for next-generation wifi and 5g wireless communications," in *2013 IEEE International Topical Meeting on Microwave Photonics (MWP)*, IEEE, 2013, pp. 5–8.

[3] N. Ghazisaidi, M. Maier, and C. M. Assi, "Fiber-wireless (fiwi) access networks: A survey," *IEEE Communications Magazine*, vol. 47, no. 2, pp. 160–167, 2009.

[4] C. Liu, J. Wang, L. Cheng, M. Zhu, and G.-K. Chang, "Key microwave-photonics technologies for next-generation cloud-based radio access networks," *Journal of Lightwave technology*, vol. 32, no. 20, pp. 3452–3460, 2014.

[5] X. Zou, B. Lu, W. Pan, L. Yan, A. Stöhr, and J. Yao, "Photonics for microwave measurements," *Laser & Photonics Reviews*, vol. 10, no. 5, pp. 711–734, 2016.

[6] P. Bacon, D. Fischer, and R. Lourens, "Overview of rf switch technology and applications.," *Microwave Journal*, vol. 57, no. 7, 2014.

[7] Q. Zhao and B. M. Sadler, "A survey of dynamic spectrum access," *IEEE signal processing magazine*, vol. 24, no. 3, pp. 79–89, 2007.

[8] M. Barnoski, *Fundamentals of optical fiber communications*. Elsevier, 2012.

[9] K. Xu, R. Wang, Y. Dai, F. Yin, J. Li, Y. Ji, and J. Lin, "Microwave photonics: Radio-over-fiber links, systems, and applications," *Photonics Research*, vol. 2, no. 4, B54–B63, 2014.

[10] B. Wu, B. J. Shastri, and P. R. Prucnal, "Secure communication in fiber-optic networks," in *Emerging trends in ICT security*, Elsevier, 2014, pp. 173–183.

[11] M. P. Fok, Z. Wang, Y. Deng, and P. R. Prucnal, "Optical layer security in fiber-optic networks," *IEEE Transactions on Information Forensics and Security*, vol. 6, no. 3, pp. 725–736, 2011.

[12] M. Li and N. Zhu, "Recent advances in microwave photonics," *Frontiers of Optoelectronics*, vol. 9, no. 2, pp. 160–185, 2016.

[13] R. A. Minasian, "Ultra-wideband and adaptive photonic signal processing of microwave signals," *IEEE Journal of Quantum Electronics*, vol. 52, no. 1, pp. 1–13, 2015.

[14] J. Capmany, G. Li, C. Lim, and J. Yao, "Microwave photonics: Current challenges towards widespread application," *Optics express*, vol. 21, no. 19, pp. 22 862–22 867, 2013.

[15] H. Zimmermann, "Osi reference model-the iso model of architecture for open systems interconnection," *IEEE Transactions on communications*, vol. 28, no. 4, pp. 425–432, 1980.

[16] J. Yao, "Microwave photonics," *Journal of lightwave technology*, vol. 27, no. 3, pp. 314–335, 2009.

[17] J. Capmany and D. Novak, "Microwave photonics combines two worlds," *Nature photonics*, vol. 1, no. 6, p. 319, 2007.

[18] T. Berceli and P. R. Herczfeld, "Microwave photonics—a historical perspective," *IEEE transactions on microwave theory and techniques*, vol. 58, no. 11, pp. 2992–3000, 2010.

[19] T. Saramaeki, S. Mitra, and J. Kaiser, "Finite impulse response filter design," *Handbook for digital signal processing*, vol. 4, pp. 155–277, 1993.

[20] J. Capmany, J. Mora, I. Gasulla, J. Sancho, J. Lloret, and S. Sales, "Microwave photonic signal processing," *Journal of Lightwave Technology*, vol. 31, no. 4, pp. 571–586, 2012.

[21] T. A. Nguyen, E. H. Chan, and R. A. Minasian, "Instantaneous high-resolution multiple-frequency measurement system based on frequency-to-time mapping technique," *Optics letters*, vol. 39, no. 8, pp. 2419–2422, 2014.

[22] X. Zou, S. Pan, and J. Yao, "Instantaneous microwave frequency measurement with improved measurement range and resolution based on simultaneous phase modulation and intensity modulation," *Journal of lightwave technology*, vol. 27, no. 23, pp. 5314–5320, 2009.

[23] J. Niu, S. Fu, K. Xu, J. Zhou, S. Aditya, J. Wu, P. P. Shum, and J. Lin, "Instantaneous microwave frequency measurement based on amplified fiber-optic recirculating delay loop and broadband incoherent light source," *Journal of lightwave technology*, vol. 29, no. 1, pp. 78–84, 2011.

[24] F. Xin, J. Yan, and Q. Liu, "Microwave frequency measurement based on optical phase modulation and stimulated brillouin scattering," *Electronics Letters*, vol. 53, no. 14, pp. 937–939, 2017.

[25] M. P. Fok, "Compact and low-latency instantaneous frequency measurement using 38 cm bismuth-oxide fiber and fiber bragg gratings," *Applied optics*, vol. 52, no. 23, pp. 5659–5662, 2013.

[26] X. Zou, W. Li, B. Lu, W. Pan, L. Yan, and L. Shao, "Photonic approach to wide-frequency-range high-resolution microwave/millimeter-wave doppler frequency shift estimation," *IEEE Transactions on Microwave Theory and Techniques*, vol. 63, no. 4, pp. 1421–1430, 2015.

[27] W. Chen, A. Wen, X. Li, Y. Gao, Y. Wang, S. Xiang, H. He, and H. Zheng, "Wideband doppler frequency shift measurement and direction discrimination based on a dpmzm," *IEEE Photonics Journal*, vol. 9, no. 2, pp. 1–8, 2017.

[28] M. Fok, K. Lee, and C. Shu, "Waveband-switchable soa ring laser constructed with a phase modulator loop mirror filter," *IEEE photonics technology letters*, vol. 17, no. 7, pp. 1393–1395, 2005.

[29] J. Ge and M. P. Fok, "Ultra high-speed radio frequency switch based on photonics," *Scientific reports*, vol. 5, no. 1, pp. 1–7, 2015.

[30] P. Ghelfi, F. Scotti, D. Onori, and A. Bogoni, "Photonics for ultrawideband rf spectral analysis in electronic warfare applications," *IEEE Journal of Selected Topics in Quantum Electronics*, vol. 25, no. 4, pp. 1–9, 2019.

[31] J. Niu, S. Fu, K. Xu, J. Zhou, S. Aditya, J. Wu, P. P. Shum, and J. Lin, "Instantaneous microwave frequency measurement based on amplified fiber-optic recirculating delay loop and broadband incoherent light source," *Journal of lightwave technology*, vol. 29, no. 1, pp. 78–84, 2010.

[32] F. N. Khan, Q. Fan, C. Lu, and A. P. T. Lau, "An optical communication's perspective on machine learning and its applications," *Journal of Lightwave Technology*, vol. 37, no. 2, pp. 493–516, 2019.

[33] X. Zou, S. Xu, S. Li, J. Chen, and W. Zou, "Optimization of the brillouin instantaneous frequency measurement using convolutional neural networks," *Optics letters*, vol. 44, no. 23, pp. 5723–5726, 2019.

[34] A. Yariv and P. Yeh, *Photonics: optical electronics in modern communications*. Oxford University Press, 2007.

[35] Q. Liu and M. P. Fok, "Dual-function frequency and doppler shift measurement system using a phase modulator incorporated lyot filter," in *2019 Optical Fiber Communications Conference and Exhibition (OFC)*, IEEE, 2019, pp. 1–3.

[36] ——, "Adaptive photonic rf spectral shaper," *Optics Express*, vol. 28, no. 17, pp. 24 789–24 798, 2020.

[37] M. Skolnik, *Radar Handbook, Third Edition*. McGraw-Hill Education, 2008, ISBN: 9780071485470. [Online]. Available: https://books.google.com/books?id=QzPHwAEACAAJ.

[38] R. A. Poisel, *Introduction to communication electronic warfare systems*. Artech House, Inc., 2008.

[39] M. K. Simon, J. K. Omura, R. A. Scholtz, and B. K. Levitt, *Spread spectrum communications handbook*. Citeseer, 1994, vol. 2.

[40] W. Hu, D. Willkomm, M. Abusubaih, J. Gross, G. Vlantis, M. Gerla, and A. Wolisz, "Dynamic frequency hopping communities for efficient ieee 802.22 operation," *IEEE Communications Magazine*, vol. 45, no. 5, pp. 80–87, 2007.

[41] G. K. Gopalakrishnan, W. K. Burns, and C. H. Bulmer, "Microwave-optical mixing in linbo/sub 3/ modulators," *IEEE Transactions on Microwave Theory and Techniques*, vol. 41, no. 12, pp. 2383–2391, Dec. 1993. DOI: 10.1109/22.260732.

[42] Y. Gao, A. Wen, H. Zhang, S. Xiang, H. Zhang, L. Zhao, and L. Shang, "An efficient photonic mixer with frequency doubling based on a dual-parallel mzm," *Optics Communications*, vol. 321, pp. 11–15, 2014.

[43] G. M. Rebeiz, *RF MEMS: theory, design, and technology*. John Wiley & Sons, 2004.

[44] P. Hindle, "The state of rf/microwave switches," *Microwave Journal*, vol. 53, no. 11, pp. 20–36, 2010.

[45] B. R. Mahafza, *Introduction to radar analysis*. CRC press, 2017.

[46] I. Aykin, M. Krunz, and Y. Xiao, "Adaptive frequency-hopping schemes for cr-based multi-link satellite networks," *International Journal of Satellite Communications and Networking*, vol. 36, no. 4, pp. 315–331, 2018.

[47] N. J. Muller, *Bluetooth demystified*. McGraw-Hill Professional, 2000.

[48] D. A. Fritz, D. W. Moy, and R. A. Nichols, "Modeling and simulation of advanced ehf efficiency enhancements," in *MILCOM 1999. IEEE Military Communications. Conference Proceedings (Cat. No. 99CH36341)*, IEEE, vol. 1, 1999, pp. 354–358.

[49] J. Montgomery, D. Runyon, and J. Fuller, "Large multibeam lens antennas for ehf satcom," in *MILCOM 88, 21st Century Military Communications-What's Possible?'. Conference record. Military Communications Conference*, IEEE, 1988, pp. 369–373.

[50] Q. Liu, J. Yan, and F. Xin, "Microwave waveform generation with reconfigurable envelope and high fidelity based on spectrum compensated frequency-to-time mapping," *Optical Fiber Technology*, vol. 36, pp. 291–296, 2017.

[51] S. Pan and Y. Zhang, "Tunable and wideband microwave photonic phase shifter based on a single-sideband polarization modulator and a polarizer," *Optics Letters*, vol. 37, no. 21, pp. 4483–4485, 2012.

[52] M. Fok, K. Lee, and C. Shu, "4/spl times/2.5 ghz repetitive photonic sampler for high-speed analog-to-digital signal conversion," *IEEE Photonics Technology Letters*, vol. 16, no. 3, pp. 876–878, 2004.

[53] F. Su, G. Wu, and J. Chen, "Photonic analog-to-digital conversion with equivalent analog pre-filtering by shaping sampling pulses," *Optics letters*, vol. 41, no. 12, pp. 2779–2782, 2016.

[54] Q. Liu and M. P. Fok, "Real-time temporal signal stitching using polarization-dependent optical wave mixing," in *Frontiers in Optics*, Optical Society of America, 2019, FTu5B–4.

[55] H. Jiang, L. Yan, W. Pan, B. Luo, and X. Zou, "Ultra-high speed rf filtering switch based on stimulated brillouin scattering," *Optics Letters*, vol. 43, no. 2, pp. 279–282, 2018.

[56] H. Jiang, L. Yan, Y. Pan, W. Pan, B. Luo, X. Zou, and B. Eggleton, "Microwave photonic comb filter with ultra-fast tunability," *Optics Letters*, vol. 40, no. 21, pp. 4895–4898, 2015.

[57] J. Ge and M. P. Fok, "Optically controlled fast reconfigurable microwave photonic dual-band filter based on nonlinear polarization rotation," *IEEE Transactions on Microwave Theory and Techniques*, vol. 65, no. 1, pp. 253–259, 2016.

[58] Y. Chen, "High-speed and wideband frequency-hopping microwave signal generation via switching the bias point of an optical modulator," *IEEE Photonics Journal*, vol. 10, no. 1, pp. 1–7, 2018.

[59] P. Zhou, F. Zhang, X. Ye, Q. Guo, and S. Pan, "Flexible frequency-hopping microwave generation by dynamic control of optically injected semiconductor laser," *IEEE Photonics Journal*, vol. 8, no. 6, pp. 1–9, 2016.

[60] V. Supradeepa, C. M. Long, R. Wu, F. Ferdous, E. Hamidi, D. E. Leaird, and A. M. Weiner, "Comb-based radio-frequency photonic filters: Routes to nanosecond tuning speed and extremely high stopband attenuation," *ArXiv: 1105.0722*, 2011.

[61] W. Li, W. Zhang, and J. Yao, "Frequency-hopping microwave waveform generation based on a frequency-tunable optoelectronic oscillator," in *Optical Fiber Communication Conference*, Optical Society of America, 2014, W1J–2.

[62] F. Zhou, X. Wang, S. Yan, X. Hu, Y. Zhang, H. Qiu, X. Xiao, J. Dong, and X. Zhang, "Frequency-hopping microwave generation with a large time-bandwidth product," *IEEE Photonics Journal*, vol. 10, no. 3, pp. 1–9, 2018.

[63] N. Shi, X. Zhu, S. Sun, W. Li, N. Zhu, and M. Li, "Fast-switching microwave photonic filter using an integrated spectrum shaper," *IEEE Photonics Technology Letters*, vol. 31, no. 3, pp. 269–272, 2019.

[64] Q. Liu, J. Ge, and M. P. Fok, "Microwave photonic multiband filter with independently tunable passband spectral properties," *Optics Letters*, vol. 43, no. 22, pp. 5685–5688, 2018.

[65] E. H. Chan and R. A. Minasian, "High conversion efficiency microwave photonic mixer based on stimulated brillouin scattering carrier suppression technique," *Optics Letters*, vol. 38, no. 24, pp. 5292–5295, 2013.

[66] J. Zheng, J. Wang, J. Yu, M. Zhu, Z. Dong, X. Wang, T. Su, J. Liu, N. Zhu, and G.-K. Chang, "Photonic microwave-signal-mixing technique using phase-coherent orthogonal optical carriers for radio-over-fiber application," *Optics Letters*, vol. 39, no. 18, pp. 5263–5266, 2014.

[67] Q. Zhou and M. P. Fok, "Microwave photonic mixer based on polarization rotation and polarization-dependent modulation," *IEEE Photonics Technology Letters*, vol. 27, no. 23, pp. 2453–2456, 2015.

[68] B. Wu, M. Wang, Y. Tang, J. Sun, and S. Jian, "Photonic microwave signal mixing using sagnac-loop-based modulator and polarization-dependent modulation," *IEEE Photonics Journal*, vol. 8, no. 4, pp. 1–8, 2016.

[69] M. P. Fok and P. R. Prucnal, "Polarization effect on opticalxorperformance based on four-wave mixing," *IEEE Photonics Technology Letters*, vol. 22, no. 15, pp. 1096–1098, 2010.

[70] H. Hu, R. M. Jopson, A. H. Gnauck, S. Randel, and S. Chandrasekhar, "Fiber nonlinearity mitigation of wdm-pdm qpsk/16-qam signals using fiber-optic parametric amplifiers based multiple optical phase conjugations," *Optics express*, vol. 25, no. 3, pp. 1618–1628, 2017.

[71] B. Lomsadze and S. T. Cundiff, "Frequency comb-based four-wave-mixing spectroscopy," *Optics letters*, vol. 42, no. 12, pp. 2346–2349, 2017.

[72] M. P. Fok and C. Shu, "Multipump four-wave mixing in a photonic crystal fiber for 6x10 gb/s wavelength multicasting of dpsk signals," *IEEE Photonics Technology Letters*, vol. 19, no. 15, pp. 1166–1168, 2007.

[73] T. Nagatsuma, S. Horiguchi, Y. Minamikata, Y. Yoshimizu, S. Hisatake, S. Kuwano, N. Yoshimoto, J. Terada, and H. Takahashi, "Terahertz wireless communications based on photonics technologies," *Optics Express*, vol. 21, no. 20, pp. 23 736–23 747, 2013.

[74] E. Compain and B. Drevillon, "High-frequency modulation of the four states of polarization of light with a single phase modulator," *Review of scientific instruments*, vol. 69, no. 4, pp. 1574–1580, 1998.

[75] R. A. Minasian, "Photonic signal processing of microwave signals," *IEEE Transactions on Microwave Theory and Techniques*, vol. 54, no. 2, pp. 832–846, 2006.

[76] G. Hueber and R. B. Staszewski, *Multi-mode/Multi-band RF transceivers for wireless communications: Advanced techniques, Architectures, and Trends*. John Wiley & Sons, 2011.

[77] M. D. Cavalier and D. Shea, "Antenna system for multi-band satellite communications," in *MILCOM 97 MILCOM 97 Proceedings*, IEEE, vol. 1, 1997, pp. 276–280.

[78] S.-C. Lin, "Microstrip dual/quad-band filters with coupled lines and quasi-lumped impedance inverters based on parallel-path transmission," *IEEE Transactions on Microwave Theory and Techniques*, vol. 59, no. 8, pp. 1937–1946, 2011.

[79] Y.-C. Lin, T.-S. Horng, and H.-H. Huang, "Synthesizing a multiband ltcc bandpass filter with specified transmission-and reflection-zero frequencies," *IEEE Transactions on Microwave Theory and Techniques*, vol. 62, no. 12, pp. 3351–3361, 2014.

[80] A. C. Guyette, "Intrinsically switched varactor-tuned filters and filter banks," *IEEE Transactions on Microwave Theory and Techniques*, vol. 60, no. 4, pp. 1044–1056, 2012.

[81] R. Gomez-Garcia and A. C. Guyette, "Reconfigurable multi-band microwave filters," *IEEE Transactions on Microwave Theory and Techniques*, vol. 63, no. 4, pp. 1294–1307, 2015.

[82] K.-W. Hsu, J.-H. Lin, and W.-H. Tu, "Compact sext-band bandpass filter with sharp rejection response," *IEEE Microwave and Wireless Components Letters*, vol. 24, no. 9, pp. 593–595, 2014.

[83] G. M. Rebeiz, K. Entesari, I. C. Reines, S.-J. Park, M. A. El-Tanani, A. Grichener, and A. R. Brown, "Tuning in to rf mems," *IEEE microwave magazine*, vol. 10, no. 6, pp. 55–72, 2009.

[84] J. Ge and M. P. Fok, "Passband switchable microwave photonic multiband filter," *Scientific reports*, vol. 5, no. 1, pp. 1–8, 2015.

[85] J. Mora, L. R. Chen, and J. Capmany, "Single-bandpass microwave photonic filter with tuning and reconfiguration capabilities," *Journal of lightwave technology*, vol. 26, no. 15, pp. 2663–2670, 2008.

[86] L. Huang, D. Chen, F. Zhang, P. Xiang, T. Zhang, P. Wang, L. Lu, T. Pu, and X. Chen, "Microwave photonic filter with multiple independently tunable passbands based on a broadband optical source," *Optics express*, vol. 23, no. 20, pp. 25 539–25 552, 2015.

[87] Y. Jiang, P. P. Shum, P. Zu, J. Zhou, G. Bai, J. Xu, Z. Zhou, H. Li, and S. Wang, "A selectable multiband bandpass microwave photonic filter," *IEEE Photonics Journal*, vol. 5, no. 3, pp. 5 500 509–5 500 509, 2013.

[88] H. Chen, Z. Xu, H. Fu, S. Zhang, C. Wu, H. Wu, H. Xu, and Z. Cai, "Switchable and tunable microwave frequency multiplication based on a dual-passband microwave photonic filter," *Optics express*, vol. 23, no. 8, pp. 9835–9843, 2015.

[89] J. Yao, "Photonics to the rescue: A fresh look at microwave photonic filters," *IEEE Microwave Magazine*, vol. 16, no. 8, pp. 46–60, 2015.

[90] A. Byrnes, R. Pant, E. Li, D.-Y. Choi, C. G. Poulton, S. Fan, S. Madden, B. Luther-Davies, and B. J. Eggleton, "Photonic chip based tunable and reconfigurable narrowband microwave photonic filter using stimulated brillouin scattering," *Optics express*, vol. 20, no. 17, pp. 18 836–18 845, 2012.

[91] D. Marpaung, B. Morrison, M. Pagani, R. Pant, D.-Y. Choi, B. Luther-Davies, S. J. Madden, and B. J. Eggleton, "Low-power, chip-based stimulated brillouin scattering microwave photonic filter with ultrahigh selectivity," *Optica*, vol. 2, no. 2, pp. 76–83, 2015.

[92] V. Supradeepa, C. M. Long, R. Wu, F. Ferdous, E. Hamidi, D. E. Leaird, and A. M. Weiner, "Comb-based radiofrequency photonic filters with rapid tunability and high selectivity," *Nature Photonics*, vol. 6, no. 3, pp. 186–194, 2012.

[93] J. Mora, B. Ortega, A. Deez, J. L. Cruz, M. V. Andres, J. Capmany, and D. Pastor, "Photonic microwave tunable single-bandpass filter based on a mach-zehnder interferometer," *Journal of lightwave technology*, vol. 24, no. 7, p. 2500, 2006.

[94] H.-J. Kim, D. E. Leaird, and A. M. Weiner, "Rapidly tunable dual-comb rf photonic filter for ultrabroadband rf spread spectrum applications," *IEEE Transactions on Microwave Theory and Techniques*, vol. 64, no. 10, pp. 3351–3362, 2016.

[95] A. Choudhary, I. Aryanfar, S. Shahnia, B. Morrison, K. Vu, S. Madden, B. Luther-Davies, D. Marpaung, and B. J. Eggleton, "Tailoring of the brillouin gain for on-chip widely tunable and reconfigurable broadband microwave photonic filters," *Optics letters*, vol. 41, no. 3, pp. 436–439, 2016.

[96] L. Gao, J. Zhang, X. Chen, and J. Yao, "Microwave photonic filter with two independently tunable passbands using a phase modulator and an equivalent phase-shifted fiber bragg grating," *IEEE Transactions on Microwave Theory and Techniques*, vol. 62, no. 2, pp. 380–387, 2014.

[97] M. P. Fok and J. Ge, "Tunable multiband microwave photonic filters," in *Photonics*, Multidisciplinary Digital Publishing Institute, vol. 4, 2017, p. 45.

[98] E. Hamidi, D. E. Leaird, and A. M. Weiner, "Tunable programmable microwave photonic filters based on an optical frequency comb," *IEEE Transactions on Microwave Theory and Techniques*, vol. 58, no. 11, pp. 3269–3278, 2010.

[99] X. Zhu, F. Chen, H. Peng, and Z. Chen, "Novel programmable microwave photonic filter with arbitrary filtering shape and linear phase," *Optics express*, vol. 25, no. 8, pp. 9232–9243, 2017.

[100] A. WaveShaper Series, *Family of programmable optical processors*, 2019.

[101] C. Pulikkaseril, L. A. Stewart, M. A. Roelens, G. W. Baxter, S. Poole, and S. Frisken, "Spectral modeling of channel band shapes in wavelength selective switches," *Optics express*, vol. 19, no. 9, pp. 8458–8470, 2011.

[102] M. P. Fok, C. Shu, and W.-W. Tang, "A cascadable approach to produce widely selectable spectral spacing in birefringent comb filters," *IEEE photonics technology letters*, vol. 18, no. 18, pp. 1937–1939, 2006.

[103] A. J. Metcalf, H.-J. Kim, D. E. Leaird, J. A. Jaramillo-Villegas, K. A. McKinzie, V. Lal, A. Hosseini, G. E. Hoefler, F. Kish, and A. M. Weiner, "Integrated line-by-line optical pulse shaper for high-fidelity and rapidly reconfigurable rf-filtering," *Optics express*, vol. 24, no. 21, pp. 23 925–23 940, 2016.

[104] D. Marpaung, C. Roeloffzen, R. Heideman, A. Leinse, S. Sales, and J. Capmany, "Integrated microwave photonics," *Laser & Photonics Reviews*, vol. 7, no. 4, pp. 506–538, 2013.

[105] H. Bogucka, P. Kryszkiewicz, and A. Kliks, "Dynamic spectrum aggregation for future 5g communications," *IEEE Communications Magazine*, vol. 53, no. 5, pp. 35–43, 2015.

[106] M. Amjad, M. H. Rehmani, and S. Mao, "Wireless multimedia cognitive radio networks: A comprehensive survey," *IEEE Communications Surveys & Tutorials*, vol. 20, no. 2, pp. 1056–1103, 2018.

[107] E. Chai, K. G. Shin, J. Lee, S.-J. Lee, and R. H. Etkin, "Fast spectrum shaping for next-generation wireless networks," *IEEE Transactions on Mobile Computing*, vol. 13, no. 1, pp. 20–34, 2013.

[108] R. Pepper, "Cisco visual networking index (vni) global mobile data traffic forecast update," Cisco, Tech. Rep., Feb. 2013. Accessed: Jul. 10, 2019.[Online]. Available …, Tech. Rep., 2013.

[109] D. Swanson and G. Macchiarella, "Microwave filter design by synthesis and optimization," *IEEE Microwave Magazine*, vol. 8, no. 2, pp. 55–69, 2007.

[110] L. Han, "A reconfigurable microwave equalizer with different maximum attenuations based on rf mems switches," *IEEE Sensors Journal*, vol. 16, no. 1, pp. 17–18, 2015.

[111] C.-S. Bres, S. Zlatanovic, A. O. Wiberg, J. R. Adleman, C. K. Huynh, E. Jacobs, J. M. Kvavle, and S. Radic, "Parametric photonic channelized rf receiver," *IEEE Photonics technology letters*, vol. 23, no. 6, pp. 344–346, 2011.

[112] X. Zou, W. Li, W. Pan, L. Yan, and J. Yao, "Photonic-assisted microwave channelizer with improved channel characteristics based on spectrum-controlled stimulated brillouin scattering," *IEEE transactions on microwave theory and techniques*, vol. 61, no. 9, pp. 3470–3478, 2013.

[113] G. Gao and L. Lei, "Photonics-based broadband rf spectrum measurement with sliced coherent detection and spectrum stitching technique," *IEEE Photonics Journal*, vol. 9, no. 5, pp. 1–11, 2017.

[114] L. Li, X. Yi, T. X. Huang, and R. Minasian, "High-resolution single bandpass microwave photonic filter with shape-invariant tunability," *IEEE Photonics Technology Letters*, vol. 26, no. 1, pp. 82–85, 2013.

[115] H. S. Wen, M. Li, W. Li, and N. H. Zhu, "Ultrahigh-q and tunable single-passband microwave photonic filter based on stimulated brillouin scattering and a fiber ring resonator," *Optics letters*, vol. 43, no. 19, pp. 4659–4662, 2018.

[116] Y. Liu, D. Marpaung, A. Choudhary, and B. J. Eggleton, "Lossless and high-resolution rf photonic notch filter," *Optics letters*, vol. 41, no. 22, pp. 5306–5309, 2016.

[117] J. Ge and M. P. Fok, "Reconfigurable rf multiband filter with widely tunable passbands based on cascaded optical interferometric filters," *Journal of Lightwave Technology*, vol. 36, no. 14, pp. 2933–2940, 2018.

[118] J. Ge, D. A. Garon, and M. P. Fok, "Photonic implementation of a highly reconfigurable wideband rf spectral shaper," *Optics Communications*, vol. 445, pp. 111–118, 2019.

[119] X. Xu, M. Tan, J. Wu, T. G. Nguyen, S. T. Chu, B. E. Little, R. Morandotti, A. Mitchell, and D. J. Moss, "High performance rf filters via bandwidth scaling with kerr micro-combs," *APL Photonics*, vol. 4, no. 2, p. 026 102, 2019.

[120] R. K. Beatson, W. Light, and S. Billings, "Fast solution of the radial basis function interpolation equations: Domain decomposition methods," *SIAM Journal on Scientific Computing*, vol. 22, no. 5, pp. 1717–1740, 2001.

[121] B. Fornberg, E. Larsson, and N. Flyer, "Stable computations with gaussian radial basis functions," *SIAM Journal on Scientific Computing*, vol. 33, no. 2, pp. 869–892, 2011.

[122] G. Borse, V. Anand, and K. Patel, "Steganography: Exploring an ancient art of hiding information from past to the future," *International Journal of Engineering and Innovative Technology (IJEIT)*, vol. 3, pp. 192–94, 2013.

[123] A. Argyris, D. Syvridis, L. Larger, V. Annovazzi-Lodi, P. Colet, I. Fischer, J. Garcia-Ojalvo, C. R. Mirasso, L. Pesquera, and K. A. Shore, "Chaos-based communications at high bit rates using commercial fibre-optic links," *Nature*, vol. 438, no. 7066, pp. 343–346, 2005.

[124] A. Uchida, *Optical communication with chaotic lasers: applications of nonlinear dynamics and synchronization*. John Wiley & Sons, 2012.

[125] G. D. Vanwiggeren and R. Roy, "Communication with chaotic lasers," *Science*, vol. 279, no. 5354, pp. 1198–1200, 1998.

[126] N. Skorin-Kapov, M. Furdek, S. Zsigmond, and L. Wosinska, "Physical-layer security in evolving optical networks," *IEEE Communications Magazine*, vol. 54, no. 8, pp. 110–117, 2016.

[127] E. I. Rosenthal, A. L. Holt, and A. M. Sweeney, "Three-dimensional midwater camouflage from a novel two-component photonic structure in hatchetfish skin," *Journal of The Royal Society Interface*, vol. 14, no. 130, p. 20 161 034, 2017.

[128] M. F. Land, "The physics and biology of animal reflectors," *Progress in biophysics and molecular biology*, vol. 24, pp. 75–106, 1972.

[129] E. J. Denton, "Review lecture: On the organization of reflecting surfaces in some marine animals," *Philosophical Transactions of the Royal Society of London. B, Biological Sciences*, vol. 258, no. 824, pp. 285–313, 1970.

[130] B. Wu and Y. Ergaibi, "Optical stealth communication for smart sensor networks," in *2017 IEEE Sensors Applications Symposium (SAS)*, IEEE, 2017, pp. 1–5.

[131] B. Liu, L. Zhang, X. Xin, and J. Yu, "Constellation-masked secure communication technique for ofdm-pon," *Optics Express*, vol. 20, no. 22, pp. 25 161–25 168, 2012.

[132] Z. Wang and P. R. Prucnal, "Optical steganography over a public dpsk channel with asynchronous detection," *IEEE Photonics Technology Letters*, vol. 23, no. 1, pp. 48–50, 2010.

[133] B. Wu, Z. Wang, Y. Tian, M. P. Fok, B. J. Shastri, D. R. Kanoff, and P. R. Prucnal, "Optical steganography based on amplified spontaneous emission noise," *Optics express*, vol. 21, no. 2, pp. 2065–2071, 2013.

[134] J. Lubacz, W. Mazurczyk, and K. Szczypiorski, "Principles and overview of network steganography," *IEEE Communications Magazine*, vol. 52, no. 5, pp. 225–229, 2014.

[135] L. Deng, M. Cheng, X. Wang, H. Li, M. Tang, S. Fu, P. Shum, and D. Liu, "Secure ofdm-pon system based on chaos and fractional fourier transform techniques," *Journal of Lightwave Technology*, vol. 32, no. 15, pp. 2629–2635, 2014.

[136] N. Li, H. Susanto, B. Cemlyn, I. Henning, and M. Adams, "Secure communication systems based on chaos in optically pumped spin-vcsels," *Optics letters*, vol. 42, no. 17, pp. 3494–3497, 2017.

[137] D. Wang, L. Wang, Y. Guo, Y. Wang, and A. Wang, "Key space enhancement of optical chaos secure communication: Chirped fbg feedback semiconductor laser," *Optics express*, vol. 27, no. 3, pp. 3065–3073, 2019.

[138] G. Unnikrishnan, J. Joseph, and K. Singh, "Optical encryption by double-random phase encoding in the fractional fourier domain," *Optics letters*, vol. 25, no. 12, pp. 887–889, 2000.

[139] Z. Zhang, M. J. Nowak, M. Wicks, and Z. Wu, "Bio-inspired rf steganography via linear chirp radar signals," *IEEE Communications Magazine*, vol. 54, no. 6, pp. 82–86, 2016.

[140] H. Zhu, R. Wang, T. Pu, T. Fang, P. Xiang, J. Zheng, Y. Tang, and D. Chen, "Experimental demonstration of optical stealth transmission over wavelength-division multiplexing network," *Applied optics*, vol. 55, no. 23, pp. 6394–6398, 2016.

[141] X. Xue, X. Zheng, H. Zhang, and B. Zhou, "Spectrum-sliced microwave photonic filter with an improved dynamic range based on a linbo3 phase modulator and balanced detection," *IEEE Photonics Technology Letters*, vol. 24, no. 9, pp. 775–777, 2012.

[142] P. Bower and I. Dedic, "High speed converters and dsp for 100g and beyond," *Optical Fiber Technology*, vol. 17, no. 5, pp. 464–471, 2011.

[143] C. Huang, P. Y. Ma, B. J. Shastri, P. Mittal, and P. R. Prucnal, "Robustness of optical steganographic communication under coherent detection attack," *IEEE Photonics Technology Letters*, vol. 31, no. 4, pp. 327–330, 2019.

[144] D. Marpaung, J. Yao, and J. Capmany, "Integrated microwave photonics," *Nature photonics*, vol. 13, no. 2, pp. 80–90, 2019.

[145] D. T. Spencer, T. Drake, T. C. Briles, J. Stone, L. C. Sinclair, C. Fredrick, Q. Li, D. Westly, B. R. Ilic, A. Bluestone, *et al.*, "An optical-frequency synthesizer using integrated photonics," *Nature*, vol. 557, no. 7703, pp. 81–85, 2018.

[146] H. Wang, J. Dai, H. Jia, S. Shao, X. Fu, L. Zhang, and L. Yang, "Polarization-independent tunable optical filter with variable bandwidth based on silicon-on-insulator waveguides," *Nanophotonics*, vol. 7, no. 8, pp. 1469–1477, 2018.

[147] C. Wang, M. Zhang, X. Chen, M. Bertrand, A. Shams-Ansari, S. Chandrasekhar, P. Winzer, and M. Lončar, "Integrated lithium niobate electro-optic modulators operating at cmos-compatible voltages," *Nature*, vol. 562, no. 7725, pp. 101–104, 2018.

[148] X. Wang, L. Zhou, R. Li, J. Xie, L. Lu, K. Wu, and J. Chen, "Continuously tunable ultra-thin silicon waveguide optical delay line," *Optica*, vol. 4, no. 5, pp. 507–515, 2017.

[149] B. Shen, P. Wang, R. Polson, and R. Menon, "An integrated-nanophotonics polarization beamsplitter with 2.4 x 2.4 um2 footprint," *Nature Photonics*, vol. 9, no. 6, pp. 378–382, 2015.

[150] D. Huang, P. Pintus, C. Zhang, P. Morton, Y. Shoji, T. Mizumoto, and J. E. Bowers, "Dynamically reconfigurable integrated optical circulators," *Optica*, vol. 4, no. 1, pp. 23–30, 2017.

[151] N. Youngblood, C. Chen, S. J. Koester, and M. Li, "Waveguide-integrated black phosphorus photodetector with high responsivity and low dark current," *Nature Photonics*, vol. 9, no. 4, pp. 247–252, 2015.